

The Effects of Neutral Gas Pressure
and Electron Temperature on the
Dynamics of the Electron Diffusion
Gauge Experiment Electron Plasma

Kyle Adam Morrison

A DISSERTATION

PRESENTED TO THE FACULTY

OF PRINCETON UNIVERSITY

IN CANDIDACY FOR THE DEGREE

OF DOCTOR OF PHILOSOPHY

RECOMMENDED FOR ACCEPTANCE

BY THE DEPARTMENT OF

ASTROPHYSICAL SCIENCES

JUNE, 2004

© Copyright 2004 by Kyle Adam Morrison.

All rights reserved.

Abstract

The dynamics of pure, electron plasmas confined in cylindrically symmetric, Malmberg-Penning traps are strongly affected by imperfections in the trap fields and collisions with background gas molecules present in the vacuum. These imperfections in the trap torque the azimuthally rotating plasma, causing it to expand radially.

The Electron Diffusion Gauge (EDG) device is used to determine whether the effects of background gas on an electron plasma can be quantitatively predicted and used to calibrate ionization gauges, the standard equipment for measuring gas pressure in the ultra-high-vacuum (UHV) regime. Earlier studies of EDG plasmas in this regime suggested that the plasma expansion is primarily due to field imperfections rather than interaction with the background gas (primarily helium), and that an observed damping of the $m = 1$ diocotron mode is more sensitive to the gas pressure. Recent measurements indicate that $m = 1$ diocotron mode growth observed at high electron-source heating voltages can be much more sensitive to other components of the background gas than the mode damping is to helium. It appears likely that ions unintentionally produced in the electron source are traversing the plasma and causing the destabilization, and that quantitative prediction of this effect will be difficult.

At higher (HV) background gas pressures, the plasma expansion rate has been observed to agree with the theoretical expansion rate predicted with a fluid description of the plasma that includes elastic collisions with background gas molecules. This agreement is impressive because the model describes uniform-temperature plasmas, and the plasmas in EDG do not necessarily have uniform temperatures at HV pressures. Greatly improved measurements of the plasmas' radial density profiles and new measurements of the on-axis plasma temperature indicate that the majority of these plasmas do not have thermal, quasi-equilibrium density profiles initially. Measurements later in the UHV-pressure evolution of thermal quasi-equilibrium plasmas reveal that expansion due to field imperfections is a factor of four lower than that estimated previously. Non-increasing temperatures measured during this later part of the evolution further suggest that the plasma is indeed losing the electrostatic potential energy liberated by the expansion, presumably through inelastic collisions with impurities in the background gas.

This thesis work is dedicated to the Lord,
God of Abraham, Isaac, and Jacob,
for His glory.

Acknowledgments

This thesis research was made possible by my research advisors, Dr. Ronald C. Davidson and Dr. Stephen F. Paul, who provided the the opportunity to work on such a unique experiment, a continual supply of practical advice, and physics insights into the plasma behavior we were observing. I am fortunate to have had the benefit of their company. This thesis work was meticulously reviewed by Dr. Ronald C. Davidson, Dr. Robert Kaita, and Dr. Cynthia Phillips, who suggested many valuable improvements for which I am quite grateful.

Dr. Samuel Cohen, my academic advisor, has contributed greatly to my perspective of physics research (and, therefore, this thesis) in the course of many enjoyable and informative discussions about physics, the universe, and everything.

I am also very grateful to my former research advisors, Dr. Richard Majeski, Dr. Robert Kaita, Dr. Masaaki Yamada, and Dr. Hantao Ji, for their instruction when I worked on CDX-U and MRX. It is doubtful that this research on EDG would have been as successful without the experience I obtained when working on those experimental devices. Dr. Tobin Munsat, Dr. Troy Carter, and Dr. Scott Hsu are also greatly responsible for helping to train and assist me on those projects. I owe what formal knowledge of plasma physics I have to the faculty in the Program in Plasma Physics.

This research builds upon the results of the previous thesis students that worked on EDG, namely, Dr. David Moore, who constructed the machine requisition by requisition, and Dr. Edward Chao, who greatly improved EDG and characterized its performance. In addition, Emily Belli and Tom Jenkins have contributed to the research on EDG, and this thesis research has also been influenced by their efforts.

No thesis is complete without an expression of thanks to Barbara Sarfaty, the Graduate Program Administrator for the Program in Plasma Physics, who kindly shepherds all students through this valley in the shadow of bureaucracy (despite their blissful ignorance of such).

Every experimental physicist and graduate student at the lab is indebted to the excellent technical staff that hold the institutional memory of the Princeton Plasma Physics Laboratory and frequently put it, expertly, to our questionable uses. The projects I have worked on have benefited incalculably from the assistance of the engineering staff, especially Jim Taylor, Dave Cylinder, Jim Gorman, Greg Lemunyan, Bob Cutler, Larry Guttadora, Tom Provost, Tom Czeizinger, John Vaccaro, Kenny Andreas, Jim Kukon, and Dick Zimmer. VAX and CAMAC communication for EDG data acquisition was graciously supported by Phyllis Roney, Tom Gibney, and John Wertenbaker. A great deal of assistance with EDG and MRX electronics (and particularly the design and testing of the EDG temperature diagnostic amplifier) was provided by Robert Marsala and Hans Schneider. Resources as valuable as these make one wonder how people doing experimental research outside of a national lab accomplish anything.

Also affecting my research through numerous conversations are the many friends I've met at Princeton, including Dr. Robin Knight, Dr. Gianmarco Felice, Dr. Steven J. Miller, Dr. Eduardo Dueñez, Seunghyeon Son, Eric Adelizzi, Dr. James

Vere, Dr. Troy Carter, Dr. Brent Jones, Dr. Daniel S. Clark, Ronald Stowell, Jef Spaleta, Alexandra Landsman, and many other great people I'm neglecting to mention for the sakes of forestry stocks and my downpayment. Truly, Princeton is a great place to work primarily because of its great people.

The greatest asset I take with me from Princeton is my wife, Julia, who has also had quite an impact on this research. I have had the luxury of spending far more of my time thinking about my research than keeping my medical coverage, thanks to her industriousness.

This research was financially supported primarily by the Office of Naval Research under contracts # N0001400F0029 and # N0001403IP20060, and in part by the Department of Energy under contract # DE-AC02-76-CHO3073.

Contents

Abstract	iii
Acknowledgments	vi
1 Introduction	1
1.1 Non-Neutral Plasmas	2
1.2 The Electron Diffusion Gauge Experiment	4
1.3 Motivation	5
1.4 Thesis Overview	7
2 Experimental Apparatus	11
2.1 The Electron Diffusion Gauge device	11
2.1.1 Filament-Matching Criterion	13
2.2 Electron Density Measurement	20
2.2.1 Radially Scanning Faraday-Cup Density Diagnostic	21
2.2.2 Phosphor-Screen Density Diagnostic	26
2.3 Temperature Diagnostics	40
2.3.1 T_{\parallel} Measurement	41
2.3.2 Inferred T_{\perp} from Measured Density Profiles	49

2.4	Diocotron Mode Diagnostic	52
2.5	Basic Equipment	57
3	The Dynamics of Long, Warm Plasmas in Malmberg-Penning Traps	61
3.1	Particle Dynamics and Transport	62
3.1.1	Global Confinement	62
3.1.2	Evolution Towards Thermal Equilibrium	64
3.2	Thermal Equilibrium and Thermal Quasi-Equilibrium Plasmas	72
3.3	Non-Ideal Plasma Expansion	77
3.3.1	Asymmetry-Induced Plasma Expansion	77
3.3.2	Plasma Evolution at Higher Pressures	80
3.4	$m = 1$ Diocotron Mode Evolution	82
3.4.1	$m = 1$ Diocotron Mode Frequency	83
3.4.2	$m = 1$ Diocotron Mode Growth Rate	85
3.5	Summary of Theoretical Predictions	91
4	Measurements of Plasma Expansion and Temperature Evolution	93
4.1	Expansion Rate Determination	94
4.2	Expansion Rate Scaling with Pressure	102
4.2.1	Review of the Previous Data	102
4.2.2	Large-Filament Data	105
4.2.3	Small-Filament Data	112
4.2.4	Phosphor-Screen Data	117
4.3	Temperature Evolution	122
4.3.1	Review of the Inferred Temperature Data	122

4.3.2	Comparison of Inferred and Measured Temperature Evolutions	125
4.4	Summary of Plasma Expansion Studies	132
5	Measurements of $m = 1$ Diocotron Mode Evolution	135
5.1	Review of Basic Comparisons with Theory	136
5.1.1	Agreement with Predicted Finite-Length Frequency	136
5.1.2	Resistive-Wall Mode Growth	138
5.1.3	“Anomalous” Mode Damping	142
5.2	Mode Sensitivity to Filament Conditions	144
5.2.1	Influence of Filament Heating Voltage	144
5.2.2	Influence of Filament Bias Voltage	148
5.3	Mode Sensitivity to Pressure	151
5.3.1	Previous Measurements of the Mode Evolution Pressure Dependence	152
5.3.2	Measurements of the Mode Growth Rate Dependence on Pressure	152
5.4	Transiting Ion Measurements	159
5.5	Summary of $m = 1$ Diocotron Mode Measurements	166
6	Conclusions	169
6.1	Dependence of the Plasma Expansion Rate on Background Gas Pressure	169
6.2	Dependence of the $m=1$ Diocotron Mode Growth Rate on Background Gas Pressure	172

A	Electron-neutral collision and ionization cross-sections	175
A.1	Helium	177
A.2	Molecular Hydrogen	178
A.3	Molecular Nitrogen	179
	Bibliography	180

List of Figures

2.1	Malmberg-Penning trap geometry	13
2.2	Cut-away schematic of the EDG device	14
2.3	Photograph of assembled trap electrodes	15
2.4	Photograph of the EDG device	15
2.5	Photograph of a small filament	17
2.6	Photograph of a small filament mounted in the filament assembly . .	17
2.7	Plot of the filament-matching criterion	19
2.8	Photograph of the front of the Faraday-cup density diagnostic	21
2.9	Photograph of the rear of the Faraday-cup density diagnostic	22
2.10	Photographs of the Faraday-cup density diagnostic electrodes.	23
2.11	Sample profiles from the two density diagnostics	24
2.12	Photograph of the plasma-facing side of the phosphor screen	27
2.13	Photograph of the CCD-camera-facing side of the phosphor screen .	28
2.14	Photograph of the light baffle for the phosphor-screen diagnostic . .	28
2.15	Photograph of the CCD camera assembly	29
2.16	Photograph of the phosphor screen's acceleration grid	30
2.17	Sample FFT-filtered images	31
2.18	Uniformity of the phosphor screen, displaced plasma test	34

2.19	Phosphor screen response vs. incident electron energy	35
2.20	Phosphor screen response vs. incident electron flux	36
2.21	Uniformity of the phosphor screen, plasma expansion test	37
2.22	Temperature measurement diagram	42
2.23	Temperature data analysis illustration	43
2.24	On-axis Temperature Diagnostic Amplifier circuit diagram	45
2.25	Photograph of the On-axis Temperature Diagnostic Amplifier	46
2.26	Example quasi-equilibrium profiles	50
2.27	$\lambda_D^2/R_{\text{cold}}^2$ vs. the equilibrium parameter ϵ for plasmas in quasi- equilibrium	51
2.28	Diocotron mode measurement diagram	53
2.29	Plasma displacement measured with the phosphor screen.	55
2.30	Predicted axial magnetic field profile	59
4.1	Density profile evolution	95
4.2	Plasma edge radius illustration	98
4.3	Plasma mean-square radius calculation integrand	99
4.4	Comparison of R_{edge} computations.	100
4.5	Previous plasma expansion rate vs. pressure measurement	104
4.6	Plasma expansion rate vs. pressure for a large filament and $B = 610$ G	106
4.7	Mean-square radius vs. time for $t < 2$ seconds.	108
4.8	Median total charge vs. time for $t < 2$ seconds.	109
4.9	Plasma expansion rate vs. pressure for a large filament and $B = 300$ G	111
4.10	Plasma expansion rate vs. pressure for a small filament and $B = 600$ G	113
4.11	Plasma expansion rate vs. pressure for a small filament and $B = 300$ G	115
4.12	Phosphor-screen images of expanding plasmas	118

4.13	Plasma expansion after $t = 3$ seconds	119
4.14	Late-time expansion rates compared to data in Fig. 4.10	121
4.15	Previous energy evolution results	123
4.16	Temperature evolution at $P \approx 6 \times 10^{-9}$ Torr	126
4.17	Estimated electrostatic potential energy evolution	128
4.18	Temperature evolution at $P \approx 2 \times 10^{-6}$ Torr	130
5.1	Comparison of measured and predicted $m = 1$ mode frequencies . . .	137
5.2	Diocotron mode growth rate vs. electrode resistance to ground	139
5.3	Displacement evolution determined from images	140
5.4	Resistively driven plasma root-mean-square radius evolution	141
5.5	Diocotron mode growth rate vs. mode frequency	143
5.6	Diocotron mode growth rate vs. heating voltage at $V_b = -16.7$ V . . .	145
5.7	Diocotron mode growth rate vs. heating voltage for multiple bias voltages	146
5.8	Parallel temperature vs. filament heating voltage	147
5.9	Diocotron mode growth rate vs. bias voltage	149
5.10	Previous amplitude evolution of the $m = 1$ diocotron mode	153
5.11	Diocotron mode growth rate vs. pressure at $V_b = -16.7$ V	155
5.12	Diocotron mode growth rate vs. pressure at $V_b = -4.7$ V	157
5.13	Diocotron mode growth rate vs. bias voltage at several pressures . . .	158
5.14	Ion current vs. background gas pressure	160
5.15	Ion current vs. confining voltage	162
5.16	Ion current dependence on filament voltages	164

A.1	Electron - He momentum transfer collision and ionization (a) cross-sections and (b) volumetric rates	177
A.2	Electron - H ₂ momentum transfer collision and ionization (a) cross-sections and (b) volumetric rates	178
A.3	Electron - N ₂ momentum transfer collision and ionization (a) cross-sections and (b) volumetric rates	179

List of Tables

2.1	Characteristic EDG plasma parameters	16
3.1	Comparison of Debye-length-interaction transport coefficients	67
A.1	Volumetric collision and ionization rates for electrons impacting helium (He)	177
A.2	Volumetric collision and ionization rates for electrons impacting molecular hydrogen (H ₂)	178
A.3	Volumetric collision and ionization rates for electrons impacting molecular nitrogen (N ₂)	179

Chapter 1

Introduction

Pure, electron plasmas are trapped in the Electron Diffusion Gauge (EDG) device [CHAO *et al.*, 2000, 1999b; MORRISON *et al.*, 2002; PAUL *et al.*, 2002; MORRISON *et al.*, 2001] in order to study the effects that background gases have on the electron plasma dynamics. The EDG device is a cylindrically symmetric, Malmberg-Penning trap (see section 2.1 and Fig. 2.1) [DEGRASSIE and MALMBERG, 1977; O'NEIL, 1995; GOULD, 1995; DRISCOLL *et al.*, 2002; ANDEREGG *et al.*, 2003; BOLLINGER *et al.*, 2003; GREAVES and SURKO, 2002; FAJANS *et al.*, 2000] with inner radius $R_w = 2.54$ cm. Malmberg-Penning traps have a uniform magnetic field parallel to the common axis of multiple, cylindrical electrodes, and particles with the same sign of charge can be confined between two nonadjacent electrodes that are charged to a sufficiently high voltage.

1.1 Non-Neutral Plasmas

Non-neutral plasmas in Malmberg-Penning traps such as EDG have been intensely studied for decades [DEGRASSIE and MALMBERG, 1977; ROBERSON and DRISCOLL, 1988; FAJANS and DUBIN, 1995; BOLLINGER *et al.*, 1999; ANDEREGG *et al.*, 2002b; SCHAUER *et al.*, 2003], and similar traps have been used to make atomic clocks [BOLLINGER *et al.*, 1985, 1994; TAN *et al.*, 1995; FISK, 1997], antihydrogen-forming apparatuses [AMORETTI *et al.*, 2002, 2003a; FUJIWARA *et al.*, 2001; GABRIELSE *et al.*, 2002], and cold-positron-beam sources [GREAVES *et al.*, 2002; GREAVES and SURKO, 2002; KURZ *et al.*, 1998; SURKO *et al.*, 2000]. Non-neutral plasmas are plasmas where there are appreciably more particles with one sign of charge than with the other (e.g., many more electrons than hydrogen ions), though most of the non-neutral plasmas studied have only one charged species (electrons, in EDG). These plasmas are similar to neutral plasmas in that they can exclude externally produced electric fields from their interior and support waves that are analogous to neutral-plasma waves where positive ion motion is not important. In fact, the dielectric function for magnetized, non-neutral plasmas is remarkably similar to that for magnetized, neutral plasmas, and many neutral-plasma waves and instabilities can be identified directly for non-neutral, electron plasmas in Malmberg-Penning traps by applying the mapping [DAVIDSON and KRALL, 1969, 1970]

$$m_p \rightarrow \infty \quad (1.1)$$

$$\omega \rightarrow \omega - l\omega_r \quad (1.2)$$

$$\Omega_c \rightarrow \Omega_c \left(1 - \frac{2\omega_p^2}{\Omega_c^2}\right)^{1/2} \quad (1.3)$$

to the neutral-plasma dispersion relation, where m_p is the mass of any positive ion in the plasma, ω is the frequency of the wave, l is the azimuthal mode number, ω_r is the plasma's equilibrium azimuthal rotation frequency, Ω_c is the electron cyclotron frequency, and ω_p is the electron plasma frequency.

There are important differences between non-neutral plasmas and neutral plasmas, however. Non-neutral plasmas have large, self-generated, equilibrium electric fields since they have a net charge, and accordingly rotate in the particles' $\mathbf{E} \times \mathbf{B}$ drift direction (at the rotation frequency ω_r) when confined by a magnetic field. Non-neutral plasmas made of particle species with the same charge sign (all positive ions or all negative ions) do not experience ambipolar diffusion, and can reach a thermal, quasi-equilibrium state (section 3.2) if they are not in contact with the trap electrodes and various sources of plasma instability are suppressed. Accordingly, non-neutral plasmas are extremely well confined, persisting in traps for tens of seconds without significant charge loss (using static trap fields) and for weeks with the addition of a small, oscillating electric field perturbation to the trap [HUANG *et al.*, 1997]. A substantial amount of effort has been made to understand the transport processes in non-neutral plasmas (see section 3.1.2) so they can be compared to the transport in neutral plasmas. Most notably, long-range "collisions" have been identified (between particles more than two particle gyroradii apart but less than a Debye length apart) that enhance the energy transport in these plasmas above the classically predicted amount.

1.2 The Electron Diffusion Gauge Experiment

The Electron Diffusion Gauge (EDG) is an experimental facility for exploring the possibility of using the dynamics of non-neutral plasmas in Malmberg-Penning traps as a pressure standard for ultra-high vacuum systems. Elastic collisions between plasma electrons and background gas molecules are both predicted [DAVIDSON and MOORE, 1996; DOUGLAS and O'NEIL, 1978] and measured [CHAO *et al.*, 2000; MALMBERG and DRISCOLL, 1980; DEGRASSIE and MALMBERG, 1980] to cause the plasma to expand radially in the trap, so measurements of the amount of plasma expansion might allow absolute determinations of the gas pressure in the UHV regime. The EDG device was built [MOORE, 1995] with a density diagnostic for measuring the axially integrated, radial density profile of the plasma and a leak valve to add helium gas into the trap for pressure control. Data from that original, Faraday-cup density diagnostic in EDG was used [CHAO, 1999] to carefully characterize the plasma formation, numerically reconstruct the electron density distribution in the trap, follow the evolutions of the plasma temperature inferred from the shape of the density profile and the estimated electrostatic potential energy, and to determine the expansion rate of the plasma. The plasma expansion rate as a function of pressure was also measured previously (Fig. 4.5) [CHAO *et al.*, 2000], and seen to be insensitive to the background gas pressure below a pressure of $P \sim 1 \times 10^{-8}$ Torr. This finding agreed with earlier particle transport measurements where imperfections in the trap fields produced a minimum level of transport at the lowest gas pressures [MALMBERG and DRISCOLL, 1980].

Theoretical results additionally suggested that estimates of the electron-neutral collision frequency (and therefore the background gas pressure) could be obtained

non-destructively from measurements of the $m = 1$ diocotron mode's growth [DAVIDSON and CHAO, 1996b]. For the previous thesis research on EDG [CHAO, 1999], a diagnostic was built to measure the mode evolution. The mode frequency, the frequency shifts for large-amplitude modes, and the instability produced by resistive trap electrodes, which were predicted and verified in other experiments, were all reproduced in EDG (section 5.1) [CHAO *et al.*, 2000, 1999c]. An additional, unexplained "anomalous" damping of the $m = 1$ mode that is stronger with increased electron density and decreased magnetic field was also characterized (Fig. 5.5) [CHAO *et al.*, 1999c], and the trap parameters were chosen in such a way to minimize it. The evolution of the $m = 1$ mode as a function of pressure was then observed [CHAO *et al.*, 2000] to damp more strongly with increased background gas pressure (Fig. 5.10). This damping was sensitive to pressure changes as small as $\Delta P \approx 5 \times 10^{-10}$ Torr, making the use of this phenomenon to sense changes in the background gas pressure a promising approach.

1.3 Motivation

Several interesting gaps in the understanding of EDG plasma dynamics were revealed by the previous measurements (section 1.2). Firstly, the plasma expansion rates measured as a function of pressure seemed to indicate that the expansion caused by electron-neutral collisions was a factor of two to four times faster than that predicted theoretically for plasmas in thermal quasi-equilibrium [DAVIDSON and MOORE, 1996]. Secondly, the temperatures inferred by fitting the measured density profiles with predicted, thermal quasi-equilibrium density profiles did not increase as the plasma expanded and electrostatic potential energy was liberated.

Thirdly, while the existence of a minimum level of expansion at the lowest gas pressures is consistent with other experiments, the causes of the minimum expansion at the lowest gas pressures in EDG were largely unknown. More detailed density and temperature measurements are necessary to explain these effects and to provide confidence in the previously reported expansion rates and $m = 1$ diocotron mode measurements. A knowledge of the background gas composition is also necessary to confirm that impurities in the background gas mixture are responsible for the energy loss from the plasma.

The previously measured dependence of the $m = 1$ diocotron mode damping on background gas pressure [CHAO *et al.*, 2000] was encouraging for the development of a pressure standard, and an investigation into its cause is necessary to produce a useful, theoretical description. The most obvious course of action is to install a smaller electron source, which provides insight into whether the mode damping is effected by plasma interaction with the trap electrodes. If it is, the trap electrode interaction might also explain the “anomalous” damping mentioned in section 1.2, as the plasma should expand more quickly for the conditions favoring the mode damping and make contact with the trap electrodes sooner. It is not immediately clear that interaction with the electrodes is the mechanism responsible, however, because the mode frequencies were quite constant during the pressure-dependent mode damping, [CHAO *et al.*, 2000] indicating that very few electrons were being lost to the trap electrodes.

The disagreement of the $m = 1$ diocotron mode resistive-electrode growth rate measurements with the theoretical prediction at high resistance (see Fig. 5.2) [CHAO *et al.*, 2000] could also be investigated to see whether the effect is due to some imperfections in the electronics systems or a true plasma effect, such as the

distortion of the plasma by an effectively charged trap electrode segment. The dependence of the diocotron mode frequency on the plasma radius and temperature has also not been characterized, and could be important since the plasma can expand a substantial amount during the long diocotron mode evolutions (see chapter 4).

1.4 Thesis Overview

In this thesis research, further detailed measurements have been performed to increase our understanding of the effects that the background gas has on the plasma dynamics. New density and temperature diagnostics were constructed and installed to improve measurement of the plasma expansion and the $m = 1$ diocotron mode evolution to further this effort. The principal results of this work are the following: 1. the expansion of EDG plasmas due to the influence of background gas molecules at HV pressures is shown to agree with the predictions from a fluid description of the plasma designed for UHV pressures, 2. the measured plasma temperature is shown to not increase after an initial relaxation of the plasma, suggesting that impurities in the background gas are draining energy from the plasmas, and 3. ions unintentionally produced by the electron source appear to be the cause of pressure- and filament-voltage-dependent $m = 1$ diocotron mode growth.

Chapter 2 describes the Electron Diffusion Gauge device used to trap the plasmas and the diagnostic equipment used to make the measurements. The way that the plasmas are trapped is described, followed by a review of the simple potential-matching rules that give an estimate for the initial plasma radius from the electron source voltages. Next, the original, Faraday-cup density diagnostic and the new,

phosphor-screen density diagnostic used to make radial density profile measurements are described. The bulk of the expansion rate measurements were made with the Faraday-cup density diagnostic, which requires the trapping of many plasmas with excellent shot-to-shot reproducibility to produce a single, axially integrated, radial electron density profile. This diagnostic was recently replaced with the more sophisticated phosphor-screen density diagnostic, which can measure an entire, 2-D, axially integrated density profile for a single plasma. This diagnostic allows reliable measurement of density profiles for plasmas that have been held in the trap for much longer than one second, as well as for plasmas that have sizeable azimuthal perturbations or are offset from the trap axis, and has thus allowed a much better understanding of the EDG plasma. Plasma temperature diagnostics important for determining the energy evolution in the plasma are described next. The temperature is diagnosed both by direct measurements of the parallel temperature at $r = 0$ and by inferring an effective perpendicular temperature by fitting a theoretical, thermal quasi-equilibrium density profile to the measured density profiles. The measurement of the $m = 1$ diocotron mode (as well as any odd-numbered, azimuthal surface wave in the plasma) with an azimuthally discontinuous electrode segment is explained next, followed by an overview of the remaining device systems (such as the solenoid used to create the magnetic field and the vacuum pumping system).

Chapter 3 of this thesis contains a review of the current theoretical and experimental understanding of electron plasmas similar to those in EDG. First, the traditional explanation for the exceptionally good confinement in non-neutral plasmas is presented, which invokes conservation of total canonical angular momentum.

The various particle and energy transport processes that allow non-neutral plasmas to reach thermal equilibrium are explained next, including the prior finding that energy can be exchanged over longer distances in these low-density plasmas than in typical laboratory plasmas because the Debye length is greater than the characteristic particle gyroradius ($\lambda_D > r_L$). Several quantities calculated for thermal equilibrium plasmas and the way that these quantities are modified by the presence of background gas molecules are then described; if the plasma expansion due to the background gas molecules is slow enough, the plasma can remain thermalized and slowly expand while maintaining a thermal quasi-equilibrium. The effects that imperfections in the trap fields and high background gas pressures have on the plasma dynamics is also discussed. Lastly, the observed and predicted dynamics of the $m = 1$ diocotron mode, a common, electrostatic, surface wave in Malmberg-Penning trap plasmas, are outlined.

Chapter 4 describes the plasma expansion and temperature evolution measurements for EDG plasmas. After an explanation of the mean-square radius and expansion rate calculation algorithms, measurements of the expansion rate dependence on pressure that show agreement with the predicted rate for uniform-temperature plasmas are presented. Further expansion rate measurements for initially smaller plasmas are also presented that confirm the observed agreement. More recent measurements using the phosphor screen density diagnostic suggest that all of these measurements were performed on plasmas that were not in a thermal quasi-equilibrium state. Specifically, the plasma expansion after an initial relaxation (apparently to thermal quasi-equilibrium) indicates that the minimum level of plasma expansion due to trap field asymmetries is at least four times less

than was previously thought. Measurements with the $r = 0$ temperature diagnostic are presented which support the hypothesis that the plasma takes at least one second to reach thermal quasi-equilibrium, but also indicate that the plasma temperature is not increasing once the plasma has attained a quasi-equilibrium state, even though the plasma continues to expand. This result is thought to indicate that the plasma is indeed losing energy continuously, presumably through inelastic collisions with impurities in the background gas.

Chapter 5 addresses the dynamics of the $m = 1$ diocotron mode in the EDG device. First, the previous verification that the mode frequency and instability due to resistive trap electrodes in EDG agree with prior experiments is reviewed, and the previous measurements of an additional, “anomalous” damping that is dependent on the plasma line density and magnetic field are described. Next, new measurements of the mode’s sensitivity to the heating voltage and bias voltage on the electron source’s filament are presented. The plasma is seen to grow as strongly at higher filament heating voltages as it does in the presence of resistive trap electrodes, and this mode growth is shown to be sensitive to the background gas pressure below $P \approx 1 \times 10^{-9}$ Torr. Measurements of ions inadvertently produced by the electron source are then presented which exhibit notable similarity to the mode growth rate dependences on source-filament voltages and pressure, suggesting that the new mode growth is due to the interaction between the plasma and these ions as they travel through the trap axially.

Finally, **Chapter 6** summarizes the conclusions drawn from the new measurements and the previous understanding of EDG plasma dynamics. Specific opportunities to enhance this understanding with further measurements and diagnostic improvements are included.

Chapter 2

Experimental Apparatus

In this chapter, the Electron Diffusion Gauge experimental apparatus is described. Section 2.1 gives a general overview of the device's operation, section 2.2 describes the original and new diagnostics for measuring the radial electron density profile, section 2.3 describes the techniques for inferring the perpendicular electron temperature from the measured density profiles and measuring the parallel temperature at $r = 0$, section 2.4 describes the measurement of electrostatic surface waves in the plasma, and section 2.5 includes additional details about the device that are not directly diagnostic-relevant.

2.1 The Electron Diffusion Gauge device

The Electron Diffusion Gauge (EDG) device is a Malmberg-Penning trap [DEGRASSIE and MALMBERG, 1977; O'NEIL, 1995; GOULD, 1995; DRISCOLL *et al.*, 2002; ANDEREGG *et al.*, 2003; BOLLINGER *et al.*, 2003; GREAVES and SURKO, 2002; FAJANS

et al., 2000; DAVIDSON, 1990]. Malmberg-Penning traps (see Fig. 2.1) are cylindrically symmetric, use a uniform, axial magnetic field to confine particles radially, and use charged, cylindrical electrodes to confine particles axially. Naturally, they are designed to confine only particles with the same sign of charge as the voltage on the confining electrodes. To trap an electron plasma, the charged electrode near the electron source (electrode 1) is temporarily set to zero Volts, allowing electrons to flow into the trap along the magnetic field. Once the trap is sufficiently full, that electrode is charged again to trap the electrons (inside grounded electrodes 2–5), where they quickly form a non-neutral plasma. To release the plasma (for diagnostic purposes), the far electrode (electrode 6) is set to zero Volts, and the electrons flow out of the trap towards the detectors.

The EDG device [CHAO *et al.*, 2000; MORRISON *et al.*, 2001] has diagnostics that can destructively measure the total number of electrons in the plasma, destructively measure the axially integrated number of electrons at a particular radial and azimuthal location, non-destructively measure the amplitude and frequency of the $m = 1$ diocotron mode as a function of time, and destructively measure the on-axis electron temperature for plasmas with a negligible diocotron mode amplitude. Because most of the diagnostics require the destruction of the plasma, it is important that these plasmas are highly reproducible. Typical EDG plasma parameters are listed in Table 2.1.

The EDG device (Figures 2.2–2.4) was constructed by Dr. David Moore [MOORE, 1995] and extensively modified by Dr. Edward Chao [CHAO, 1999] and Dr. Stephen Paul. A detailed description of the device’s hardware and the original diagnostic

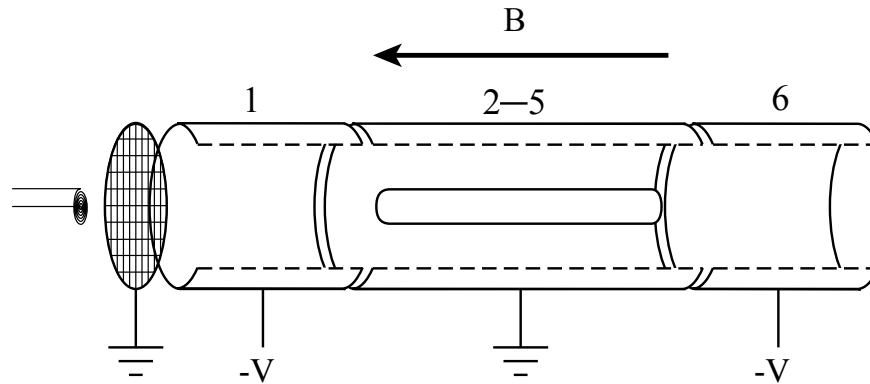


Figure 2.1: Malmberg-Penning trap geometry.

set is presented in Dr. Chao's thesis [CHAO, 1999], and a brief description of the device and the details of the new density and temperature diagnostics are presented in this chapter.

2.1.1 Filament-Matching Criterion

The electron source in EDG is a spiral, 2% thoriated tungsten filament (Fig. 2.5) that is resistively heated across its leads and biased at its center to induce emission of electrons [MALMBERG and DEGRASSIE, 1975]. The electric field between the biased filament and a parallel, grounded, stainless steel wire grid just 1.0 cm closer to the trap electrodes (Fig. 2.6) causes many thermionically emitted electrons to enter the trap. For sufficiently high filament temperatures, the flow of electrons into the trap at a given filament bias voltage behaves as though it were space-charge-limited and is less sensitive to changes in the temperature-dependent emission at the filament's surface. The filament may also be heat-treated to migrate thorium (Th) atoms to its surface for better emission by first applying a high current [LANGMUIR, 1923; JONES and LANGMUIR, 1927] to break apart the thoria (ThO_2)

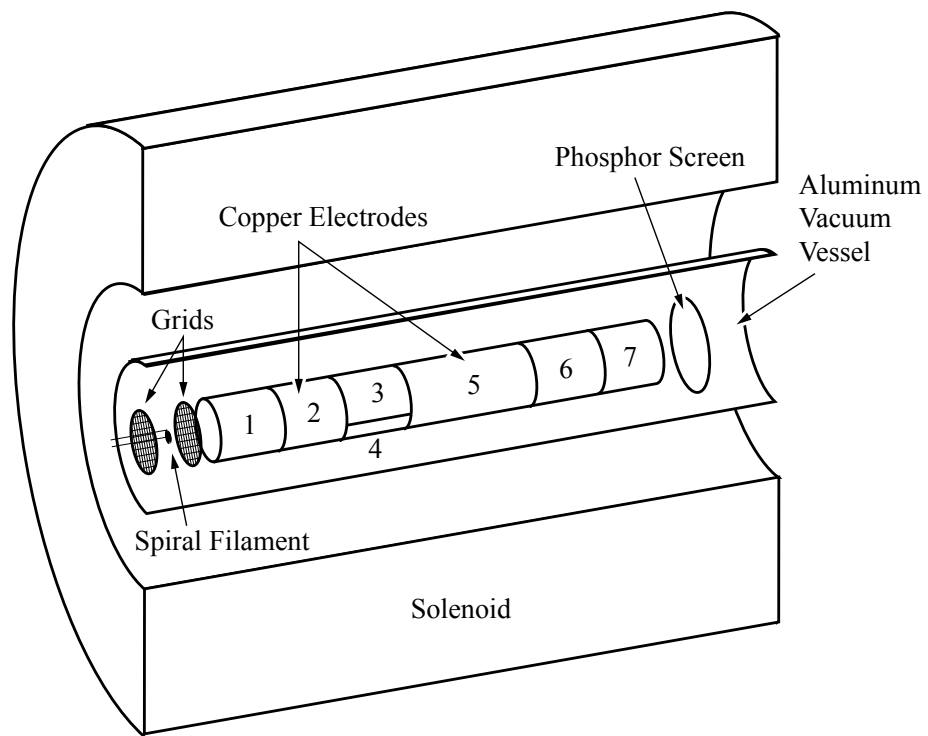


Figure 2.2: Cut-away schematic of the EDG device.



Figure 2.3: Trap electrodes and filament assembly.

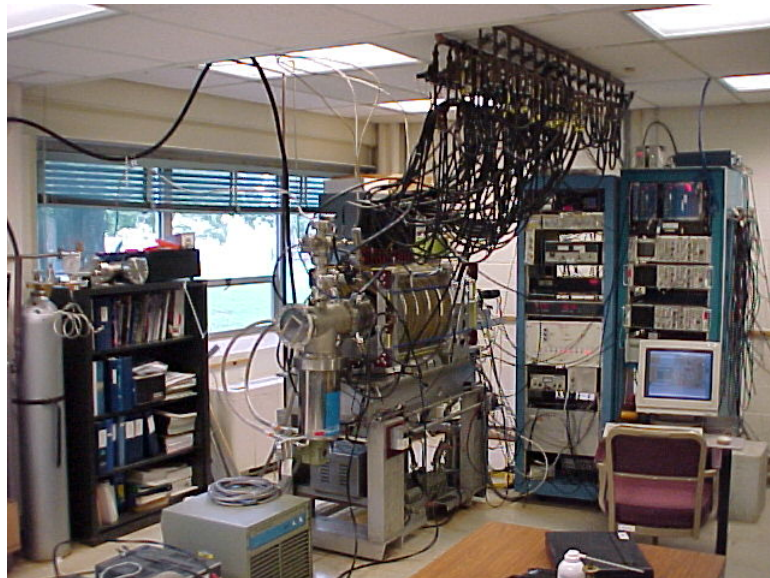


Figure 2.4: Side view of the EDG device.

Quantity	Symbol	Characteristic value
Background gas pressure	P	$1 \times 10^{-10} - 1 \times 10^{-5}$ Torr
Electron temperature	T	1 eV
Magnetic field imposed	B	600 G
Total number of electrons	N	5×10^8 electrons
Plasma length	L_p	15 cm
Plasma radius	$R_p(t = 0)$	0.87 cm (sm. fil.) and 1.27 cm (large fil.)
Density on-axis	$n(r = 0)$	$1.15 \times 10^7 / \text{cm}^3$
Plasma line density	N_L	3.3×10^7 electrons/cm
Electron thermal velocity	v_T	4.2×10^7 cm/s
Plasma frequency	$\omega_p/2\pi$	30 MHz
Cyclotron frequency	$\omega_c/2\pi$	1.7 GHz
Plasma rotation frequency	$\omega_r/2\pi$	290 kHz
Axial bounce frequency	$\omega_b/2\pi$	1.4 MHz
$m = 1$ Diocotron mode frequency	$\omega_D/2\pi$	40 kHz
Electron-electron collision frequency	ν_{ee}	200 Hz
Electron-neutral collision frequency	ν_{en}	$0.15 - 1.5 \times 10^4$ Hz
Electron gyroradius	r_L	0.04 mm
Debye length	λ_D	0.21 cm
Confining voltage	$\phi_{\text{confining}}(r = 0)$	-129 V
Plasma potential on-axis	$\phi_{\text{plasma}}(r = 0)$	-15 V

Table 2.1: Characteristic EDG plasma parameters. The plasma line density N_L is the number of electrons per unit axial distance.

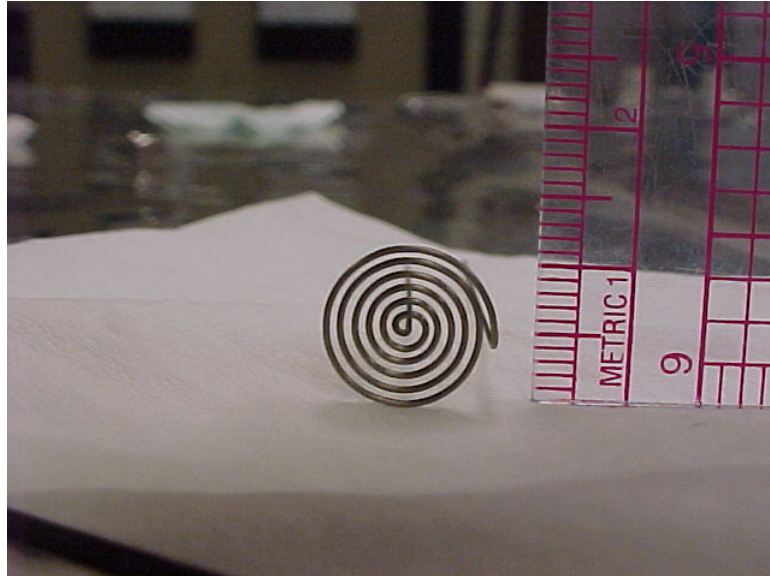


Figure 2.5: One of the small filaments used in EDG.

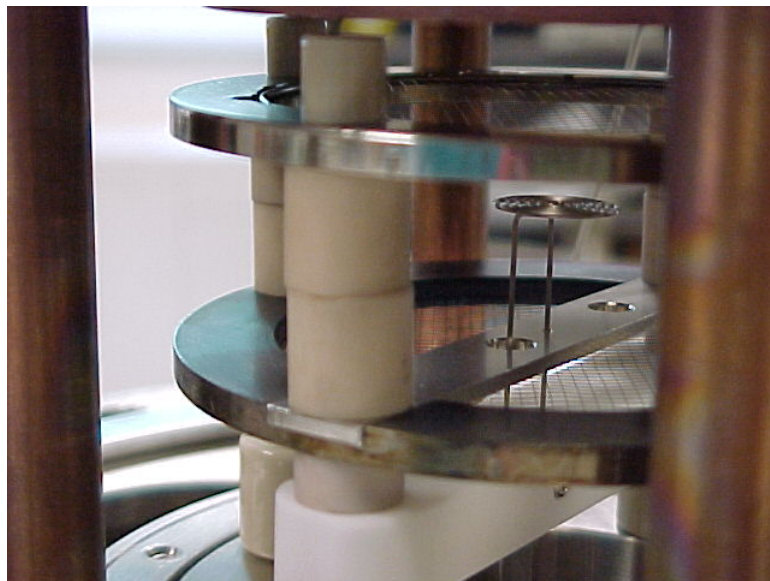


Figure 2.6: View of a small filament mounted in EDG. The front end of the trap is barely visible at the top of the image, the grid above the filament is set to zero volts to encourage electron emission, and the grid below is electrically connected to the center of the filament, which is biased to the filament bias voltage V_b .

molecules (21A for ~ 30 seconds for a 0.02-inch-diameter tungsten wire) and secondly applying a lower current to migrate the thorium atoms through the metal (12A for ~ 20 minutes). Recently, however, this has not reliably produced larger, more consistent emission than has simply heat-treating at the lower current (possibly due to aging of the filaments). Once the trap is filled, the confining electrode on the filament side of the trap (the “entrance” electrode, electrode 1) is negatively charged and no additional electrons flow into the trap.

When the emission from the filament appears space-charge-limited, the resulting plasma radius for a constant density plasma may be estimated [MALMBERG and DEGRASSIE, 1975] by equating the radial potential variation on the filament and the radial potential variation in the plasma. This “filament-matching criterion” results in the equation

$$\frac{V_b}{V_h} = \frac{R_p^2}{R_f^2} \left(-2 \ln \left(\frac{R_p^2}{R_f^2} \right) + 2 \ln \left(\frac{R_w^2}{R_f^2} \right) + 1 \right), \text{ or} \quad (2.1)$$

$$Y = X^2 (-2 \ln X + 2 \ln A + 1), \quad (2.2)$$

where V_b is the voltage applied to the center of the filament for biasing, V_h is the voltage applied across the filament for heating, R_p is the predicted uniform-density-plasma radius, R_f is the filament’s outer radius, R_w is the inner radius of the trap electrodes, $Y = V_b/V_h$, $X = R_p/R_f$, and $A = R_w/R_f$. This equation can be used to estimate the initial plasma radius for a given set of filament voltages, and predicts the plasma’s axial line density to be

$$2\pi \int_0^{R_w} r dr n(r, z) \equiv N_L = X^2 (N_L)_{\max}, \quad (2.3)$$

where

$$(N_L)_{\max} = V_h/e \quad (2.4)$$

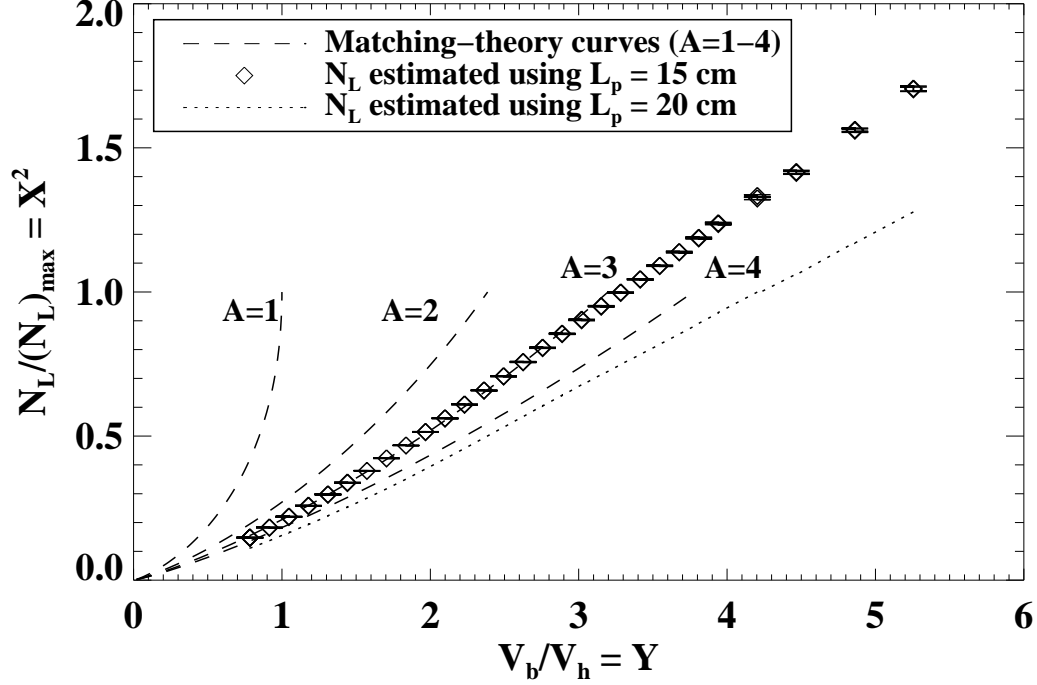


Figure 2.7: Plot of line density $N_L \approx N/L_p$ versus the ratio V_b/V_h for a $R_f = 0.635$ cm filament. The line density is estimated by dividing the measured total plasma charge N by the typical plasma length L_p found in an equilibrium code (which is mentioned in section 4.1). The data appear consistent with the filament-matching condition in Eq. (2.1) for the parameter $A = R_w/R_f = 3$ instead of the predicted $A = 4$. A similar enhancement was seen for large-filament plasmas ($A = 1.75$ instead of $A = 2$) [CHAO, 1999], and the higher line density was thought to be caused by axial compression of the trapped electron cloud as the voltage on electrode 1 is lowered (to “close” the trap).

and e is the charge of an electron. The total number of electrons in the plasma measured as a function of V_b/V_h is compared with this estimate in Fig. 2.7 for a filament with $R_f = 0.635$ cm (1/4 inch). When the ratio V_b/V_h increases past the point where $N_L / (N_L)_{\max} = 1$, the simple filament-matching criteria is no longer valid, and the plasma radius is approximated as the filament radius ($R_p = R_f$) for further calculations. A more sophisticated, 1-D model of the initial plasma density

distribution which extends to this regime, incorporates the electron temperature, and allows the description of non-uniform electron emission over the filament surface was developed by Kriesel and Driscoll [KRIESEL and DRISCOLL, 1998]. This model was not applied to EDG plasmas because of difficulties in measuring the temperature and the electron emission.

Two different sizes of filaments were used for this research: $R_f = 1.27$ cm (large) and $R_f = 0.635$ cm (small).

2.2 Electron Density Measurement

Since EDG pure-electron plasmas have a relatively low density ($n \sim 1 \times 10^7 / \text{cm}^3$) in comparison with typical laboratory plasmas, conventional Langmuir probes can't be used to measure the plasma density or temperature. The electron density and temperature are instead measured by releasing the entire plasma from the trap into detectors located just outside the trap axially. The evolution of the plasma for a given set of conditions is then inferred by comparing measurements of similar plasmas that were confined in the trap for different amounts of time. The standard deviation of the total plasma charge measured under identical conditions is usually less than 0.2%, indicating that the plasmas are highly reproducible.

Two different diagnostics were used for measuring the radial electron density profile in this research: the radially scanning Faraday-cup density diagnostic for the earlier data, and the phosphor-screen density diagnostic for the most recent data.

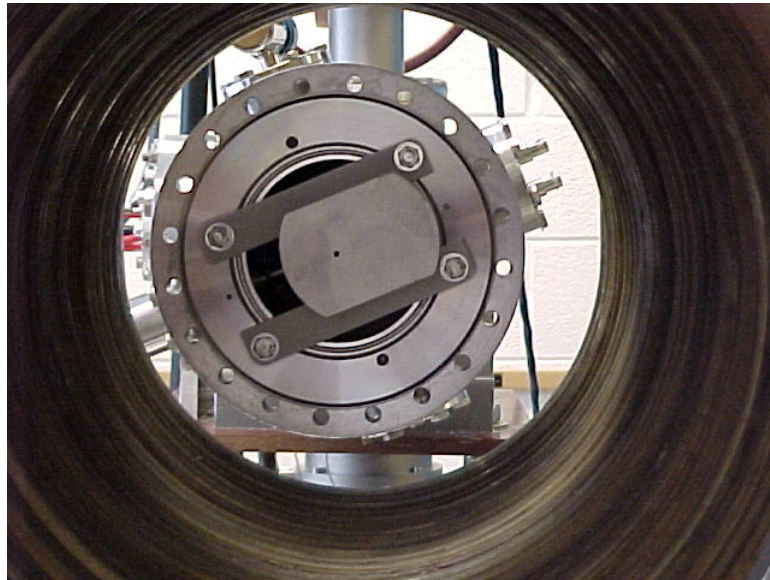


Figure 2.8: Trap-side view of the Faraday-cup density diagnostic collimating plate.

2.2.1 Radially Scanning Faraday-Cup Density Diagnostic

The radially scanning, Faraday-cup density diagnostic (Figures 2.8–2.9) was previously used to obtain radial density profiles in the EDG device [CHAO, 1999] by methodically measuring the number of electrons in the trap near particular radial and azimuthal locations; a density profile could be accumulated by trapping several plasmas at the same trap conditions and making measurements at different radii. After a plasma was released, it would first encounter a collimating plate with a small hole [Figures 2.10(a), 2.8] that selected the axial column of electrons to measure. Next, most of the electrons that passed through the hole would pass through an identical hole in a separate plate [Fig. 2.10(b)] behind the collimating plate. Finally, the electrons that passed through both plates would alight upon an additional measurement electrode behind them [Fig. 2.10(c)].

Approximate, axially integrated density profiles were constructed by moving the collector assembly radially between measurements to observe the number of

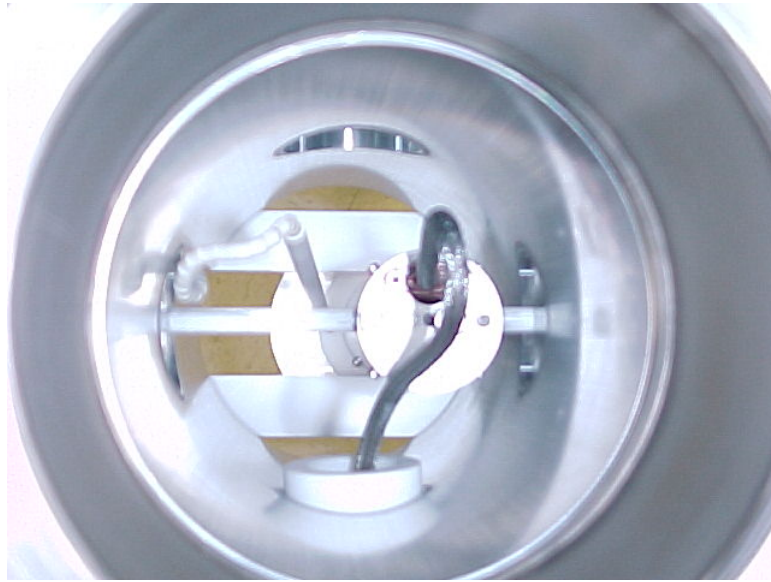
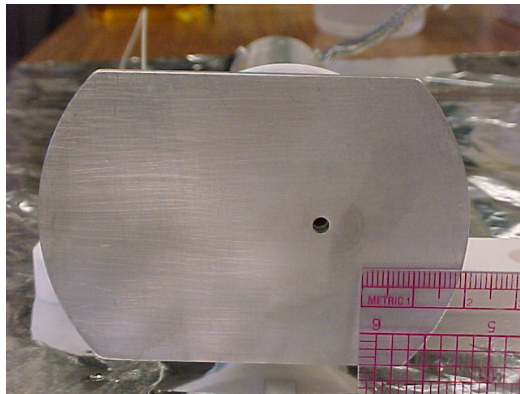


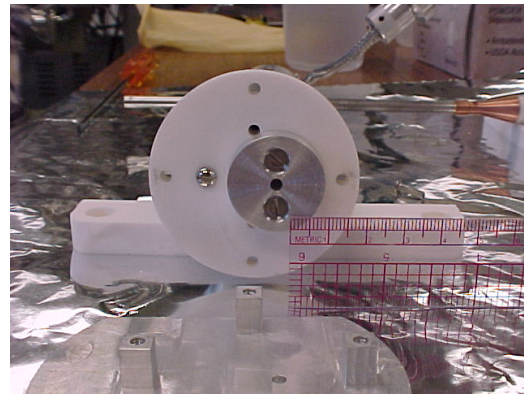
Figure 2.9: Rear view of the Faraday-cup density diagnostic.

electrons at different radii. This process could be performed at different times in the plasma evolution (“hold times”) to measure the change in the density profile. Profiles obtained with this diagnostic are presented in Figures 2.11(b) and 2.11(c), along with an illustrative profile obtained with the phosphor-screen density diagnostic in Fig. 2.11(a).

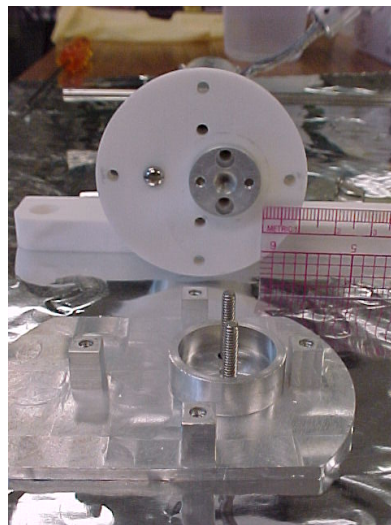
The total number of electrons (“total charge”) in any given plasma was determined by summing the amounts of charge collected by the collimating plate and the second measurement electrode. The signal from the collimating plate (the “total collector”) was calibrated by setting all cylindrical trap electrodes to zero Volts and measuring the the changing voltage on the plate as electrons from the filament flowed directly onto it. The detector capacitance was then determined to be $C = I_{tc}/(dV_{tc}/dt)$, where I_{tc} is the current reaching the plate and V_{tc} is the voltage on the plate. The signals from the measurement electrode (the “local collector”, in



(a) Total Collector.

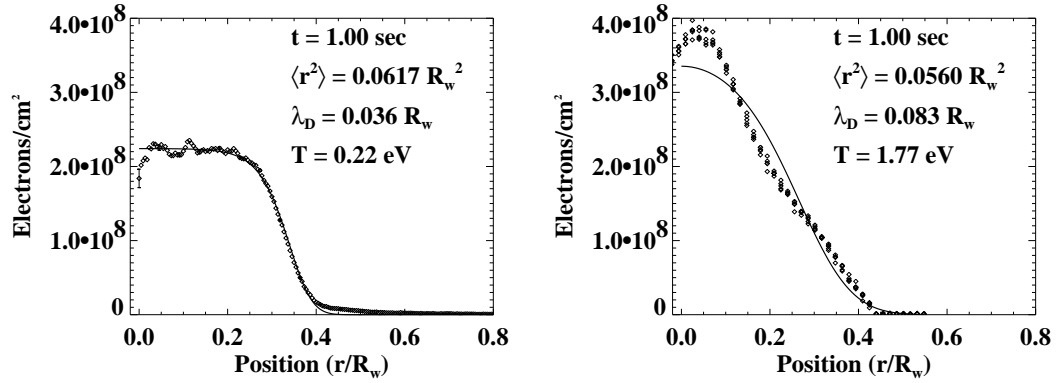


(b) Capacitive shield.



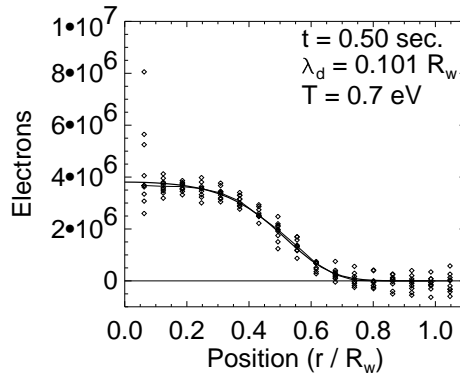
(c) Local Collector.

Figure 2.10: Faraday-cup density diagnostic electrodes.



(a) Image-derived profile.

(b) Faraday-cup-derived profile (small filament).



(c) Faraday-cup-derived profile (large filament).

Figure 2.11: Figure 2.11(a) shows an illustrative image-derived density profile overlaid with a thermal quasi-equilibrium profile, obtained using the CCD camera and a small tungsten filament. Figure 2.11(b) shows an example of data obtained with the Faraday-cup density diagnostic, also for a small filament. Figure 2.11(c) is an example of the profiles obtained using the Faraday-cup diagnostic to observe a plasma formed with a large filament. The small features in the density data in Fig. 2.11(a) for $r < 0.2R_w$ vary for different images (e.g., see Fig. 4.1), and are thought to be simply due to noise in the images. The off-axis peak in the density profile in Fig. 2.11(b) is thought to be due to uncorrectable misalignment of the diagnostic with the trap.

Fig. 2.10(c)) were calibrated by correlating them with the signals from the collimating plate at several radii; electrons that do not hit the total collector or the second plate behind it should hit the local collector, and the correlation can be seen by moving the collector assembly radially across the plasma cross section. The second plate (the “capacitive shield”) was included to reduce the capacitive coupling between the collimating plate and the measurement electrode. For this calibration, we did not account for any electrons intercepted by the capacitive shield.

Even after this careful calibration of the local collector, the integral of the axially integrated density profile generally does not agree with the calculated total charge. This has been attributed [CHAO, 1999] in part to changes in the effective collimating hole radius due to finite electron gyroradii; roughly, the electrons within a gyroradius of the hole’s edge could be collected by the total collector or the capacitive shield instead of the local collector. Misalignment of the magnetic field with the trap, misalignment of the local collector with the trap axis, and potentially unequal radial steps taken by the local collector due to imperfections in the linear motion feedthrough could also contribute to the discrepancy. This disagreement is circumvented for analysis purposes by normalizing the measured axially integrated density profile so its integral agrees with the total charge measured.

The collimating plate was biased to +15 V and the local collector electrode was biased to +23 V to ensure that all the incident electrons would be collected. This is especially important because they are both made of aluminum, which tends to reflect a fair fraction of low energy, incident electrons. The power supplies that biased the measurement electrodes were disconnected during the density measurements to reduce noise, but the capacitive shield was connected to 0. V (grounded)

continuously. The collimating hole is 0.159 cm in diameter, which, in fact, is a sizeable fraction of the plasma cross section for small-filament plasmas. The plasma was trapped between electrodes 1 and 6 (see Fig. 2.2) to reduce the capacitive coupling between the collimating plate and the confining electrode. At least five measurements were made at each radial position to reduce the effects of noise on the resulting density profile.

2.2.2 Phosphor-Screen Density Diagnostic

The phosphor-screen density diagnostic records an entire axially integrated, 2-D density profile for a single plasma. It allows reliable measurement of density profiles for plasmas with large-amplitude diocotron modes and plasmas that have been held in the trap much longer than 1 second. It was designed, assembled, and tested primarily by Dr. Stephen Paul, based upon information about similar diagnostics already in operation [GILSON, 2001; PEURRUNG and FAJANS, 1993; HUANG *et al.*, 1995; FINE *et al.*, 1995].

Phosphor-Screen Density Diagnostic Description

To make a density measurement, the plasma is released from the trap and accelerated into a 10 μm -thick P-43 phosphor coating on a glass screen (Figures 2.12 and 2.13). The phosphor scintillates where it is struck by electrons, and the glowing image of the axially integrated plasma is captured by a CCD camera. The digital image is saved, and an axially integrated radial density profile is determined by averaging the plasma image azimuthally around its centroid.

The light emitted by the phosphor passes through the glass screen, a glass vacuum window, an interference filter tuned near to the peak emission wavelength of

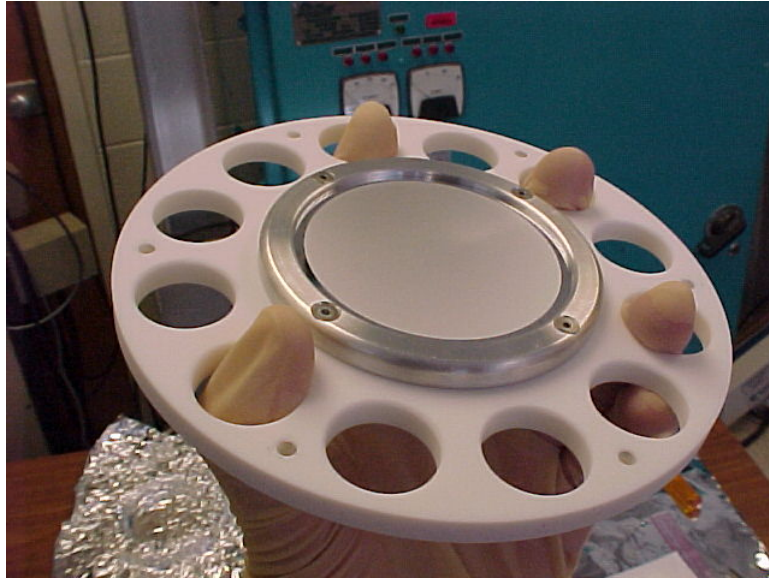


Figure 2.12: The phosphor screen in its machinable-ceramic mount. This side faces the plasma.

the P-43 phosphor (545 nm), an $f=1.5$ camera lens, and a separate image intensifier on its way to the CCD camera (Fig. 2.15). Another ~ 50 nm-thick aluminum coating covering the phosphor reflects nearly all of the light emitted from the filament and serves as an electrode for accelerating the electrons. Additional light baffles (Fig. 2.14) behind the screen reduce the amount of reflected filament light illuminating the back of the screen or entering the camera directly.

The aluminum coating is biased to $V_s = 3\text{--}5$ kV to give the electrons sufficient energy to penetrate the aluminum and excite the phosphor underneath (Fig. 2.13). A grounded, 95% transparent, electroformed copper grid is affixed to the end of the trap to produce a more uniform accelerating electric field (Fig. 2.16). Putting this grid in the path of the escaping plasma has the detrimental effects of focusing (or defocusing) some of the plasma electrons into (or away from) a grid pattern on the screen and absorbing some of the plasma electrons before they reach the



Figure 2.13: The back side of the phosphor screen that the CCD camera sees. This picture was taken before the light baffle in Fig. 2.14 was installed.



Figure 2.14: This light baffle was mounted roughly 1 inch behind the phosphor screen to block stray filament light. The inside faces of the grooves in its surface are perpendicular to its base to reduce the light reflected inwards towards the back of the phosphor screen. The offset hole in the baffle ensures a safe distance between the grounded baffle and the bias wire to the 3–5 kV phosphor screen, seen in Fig. 2.13.

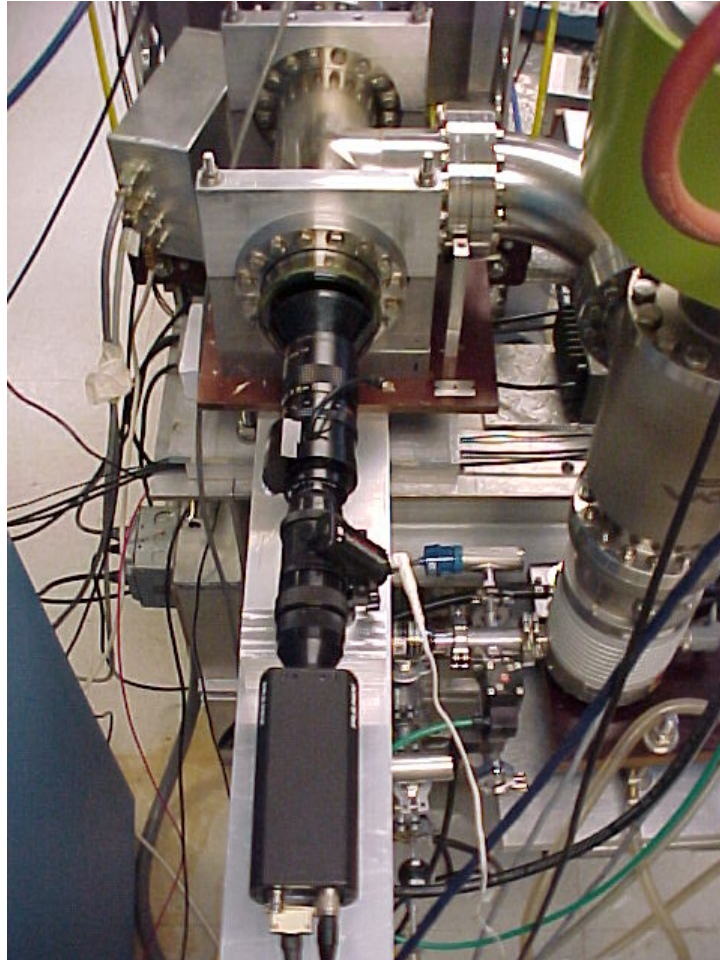


Figure 2.15: The black CCD camera assembly is supported by a tripod mount underneath so the camera can be rotated or pitched to better view the screen. The camera is the black box at the bottom with white writing on the sides, the white power cord on the right is plugged into the image intensifier, the camera lens is in the segment with a knurled grip (just past the segment with a protrusion to the left), and the interference filter is cemented near the base of the flared segment at the far end of the assembly (next to the vacuum window). The phosphor screen itself is just inside the near end of the solenoid coils at the top of the photograph.

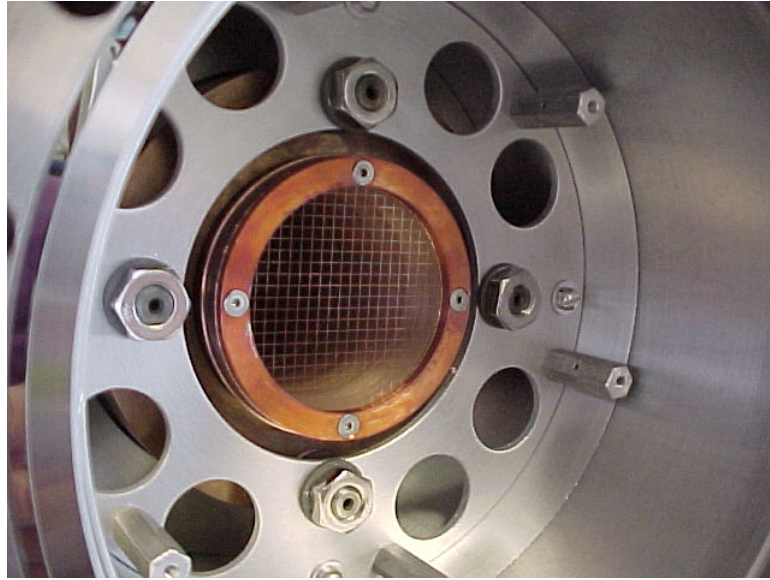


Figure 2.16: View of the phosphor-screen acceleration grid, which is mounted on the last trap electrode.

screen. Whether the electrons are focused, defocused, or indeterminately focused by the grid is dependent on the magnitude of the magnetic field, and the electrons appear alternately focused and defocused as the field is increased. The focused-electron patterns seen for typical EDG operating conditions are readily eliminated by masking out the peaks corresponding to the grid wire spacing in the Fourier transform of the image. The results of this FFT-masking procedure are illustrated in Fig. 2.17.

The radial image profile $c(r)$ is then calculated as medians $c(r_n)$ of the image values between the distances $r_n = n \delta r$ and $r_{n+1} = (n + 1) \delta r$ from the image centroid for all $r \leq R_w$, where δr is the distance on the screen that corresponds to the width of one camera pixel, r is measured from the centroid of the plasma image, and n is a non-negative integer. The uncertainty $\sigma_c(r_n)$ of the value $c(r_n)$ is estimated as the standard deviation of the mean of the image values used to

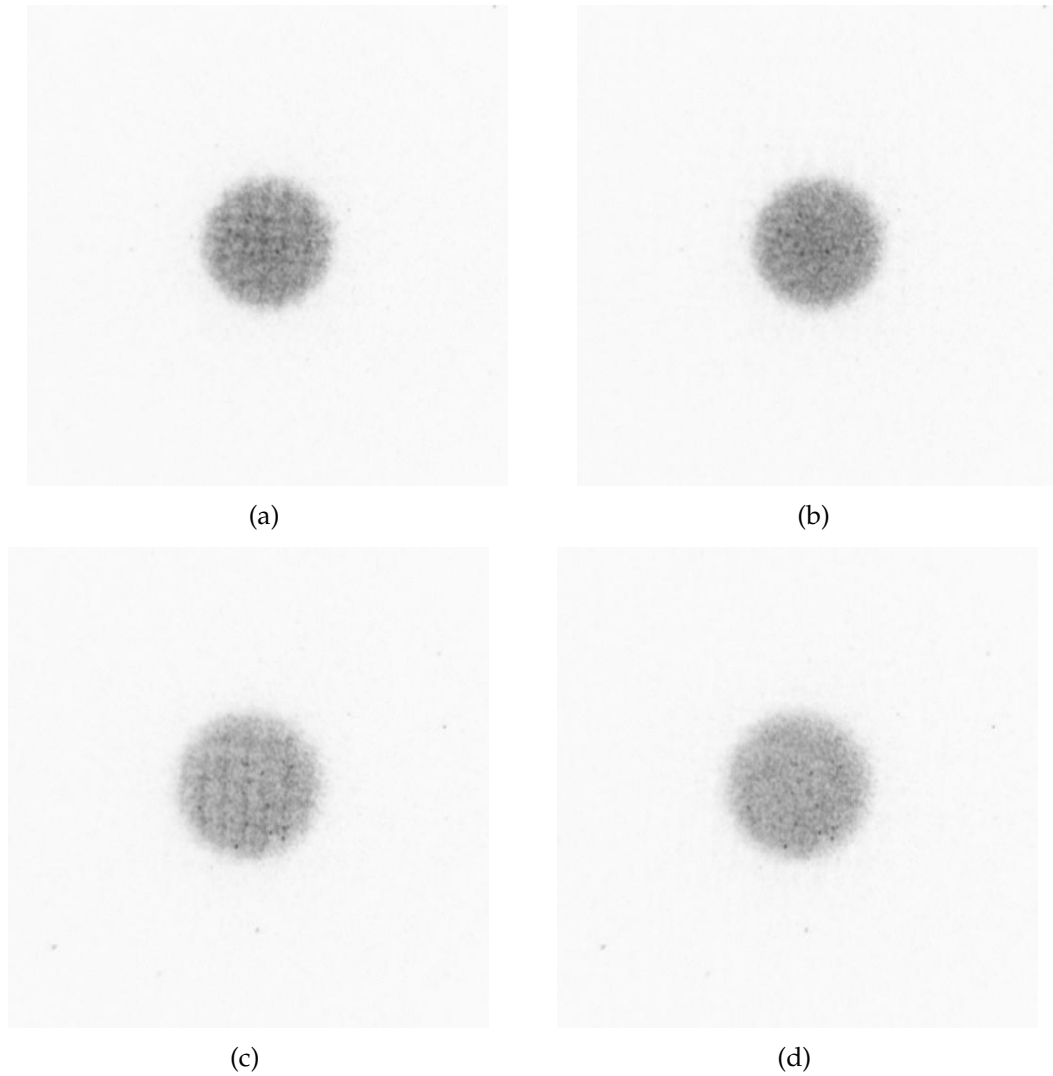


Figure 2.17: Raw and FFT-masked plasma images. The images on the right are the FFT-masked versions of the images on the left. Image 2.17(b) has the density profile shown in Fig. 4.1(a), and image 2.17(d) has the density profile shown in Fig. 4.1(b) and Fig. 2.11(a).

compute $c(r_n)$. The noise level of the CCD camera is estimated as the median of the image values at points outside the trap radius (specifically, in the range $r = 2.6\text{--}2.8$ cm), and is subtracted from the entire image before the profile is determined.

The axially integrated, radial density profile is obtained by multiplying the radial image profile by the ratio of the total number of electrons collected by the screen (the “total charge”) to the numerical integral of the unnormalized radial image profile $2\pi \int r dr c(r)$. An example of the resulting density profile is presented in Fig. 2.11.a . This normalization is performed for each individual image taken, both because the dependence of the image’s total counts on the screen bias voltage V_s had not been characterized and the noise level of the CCD camera is a function of the imperfectly controlled room temperature.

Phosphor-Screen Response Characteristics

There are several details of the phosphor screen response that must be characterized in order to know how the relative intensity of different pixels in the image corresponds to differences in electron density. To use a spatially independent, linear relationship between the light intensity and the number of incident electrons (as implied in the foregoing description of the profile determination), one must check that the amount of light emitted by the screen at any given location is a strong, linear function of the number of incident electrons, only a weak function of the incident electrons’ energy, and not a function of the position on the screen (the phosphor should respond the same to a given electron input at all locations). It is fairly difficult to measure these three responses separately in our trap, so a few different tests were performed that give an indication of the phosphor screen’s response. These qualities could be tested outside of the EDG device (but still in

a vacuum) by scanning an electron beam with a variable particle energy across the surface of the screen or by illuminating the screen with X-rays from an X-ray source, but neither of these somewhat involved methods were used to diagnose the EDG phosphor screen because of time and funding constraints.

An indication of the the uniform response of the screen at all locations may be made by displacing the plasma from the trap axis a variable amount so it will strike a different part of the screen when it is released. This is accomplished by exciting an $m = 1$ diocotron mode using resistors (see sections 3.4.2 and 5.1.2), but a similar result may be obtained by tilting the magnetic field relative to the trap electrodes. In Fig. 2.18, the normalized number of image counts per electron is plotted as a function of the plasma displacement. The number of image counts per electron is estimated to be the ratio of the image's total counts to the measured total number of electrons, and is arbitrarily normalized for clarity. Though there is a fair amount of scatter in the data, there doesn't appear to be any clear dependence of the number of image counts per electron on the distance from the trap axis. If there is no dependence, it either means that the screen's responses to the incident electron flux and the incident electron energy are the same at all the locations sampled by the plasmas in Fig. 2.18, or that any changes in these properties across the screen are offsetting.

If the screen's responses to the incident electron flux and the incident electron energy are independent at all locations on the screen and the screen's response to incident electron energy is indeed uniform, the screen's response to incident electron energy can be determined by varying the bias voltage on the phosphor screen and measuring identically formed plasmas. In Fig. 2.19, the estimated number of image counts per electron is plotted as a function of the phosphor screen voltage

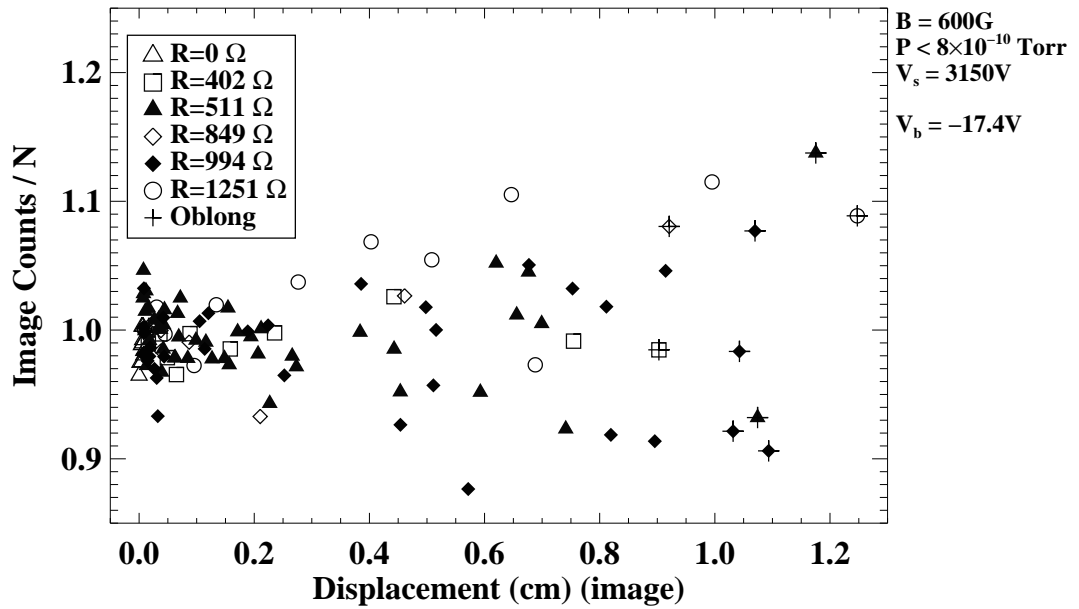


Figure 2.18: Normalized image counts per electron vs. plasma displacement. The plasmas are displaced from the trap axis by as much as 1.25 cm, and the number of image counts per electron changes by less than $\sim 15\%$. The data denoted by open symbols is calculated from the same data set used to produce Fig. 5.2. The points marked as “oblong” are from plasmas that are close enough to the trap electrodes to be visibly distorted azimuthally and may have some interaction with the electrodes. The normalization for the number of image counts per electron is arbitrary, and the true values are approximately 0.008 times those shown. For this data, $B = 600 \text{ G}$, $V_s = 3150 \text{ V}$, and $V_b = -17.4 \text{ V}$. The data denoted with open symbols was taken with $V_h = 4.1 \text{ V}$, and the data denoted with solid symbols was taken with $V_h = 4.8 \text{ V}$.

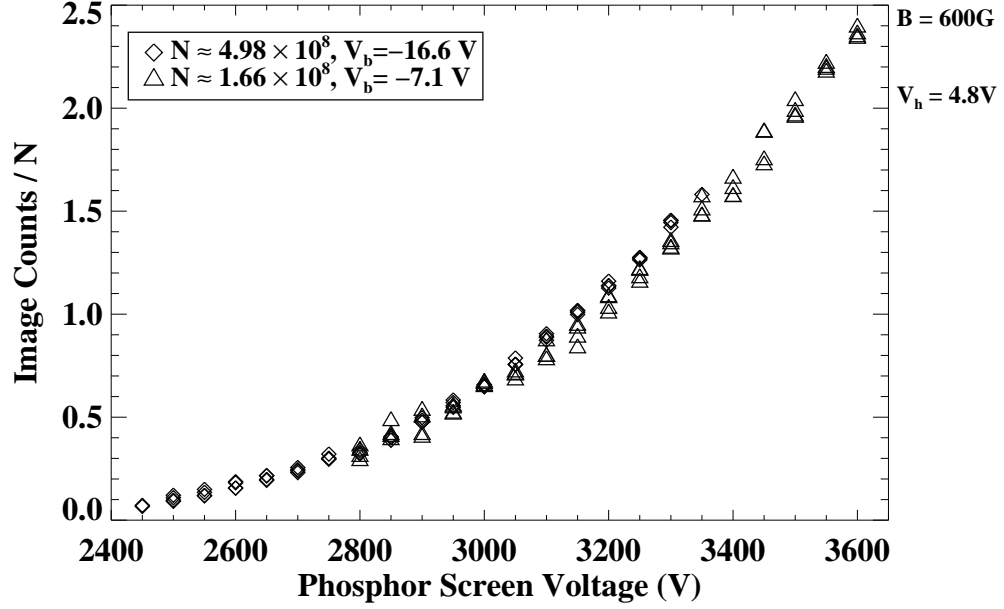


Figure 2.19: Normalized image counts per electron vs. phosphor screen voltage, measured for plasmas with zero displacement from the trap axis ($D = 0$). The normalization factor is the same as for Fig. 2.18.

V_s . While the number of image counts per electron is clearly dependent on the phosphor screen voltage, it is only weakly dependent. For example, the number of image counts per electron roughly doubles from $V_s = 3200$ to $V_s = 3500$, so a difference in electrostatic potential energy of $\Delta\phi_p \approx 15$ V between the center and the edge of the plasma only effects a $\sim 0.5\%$ difference in the amount of light emitted per electron. This test inherently averages over the approximate incident electron energy range $V_s - T \lesssim E \lesssim V_s + \phi_p(r = 0) + T$, since many of the electrons at $r = 0$ will be imparted the equilibrium plasma potential $\phi_p(r = 0)$, half of the particles will be initially moving towards the screen with the additional, average thermal energy T , and half will be initially moving away from the screen. The agreement between the data for plasmas with $N \approx 4.98 \times 10^8$ electrons and $N \approx 1.66 \times 10^8$

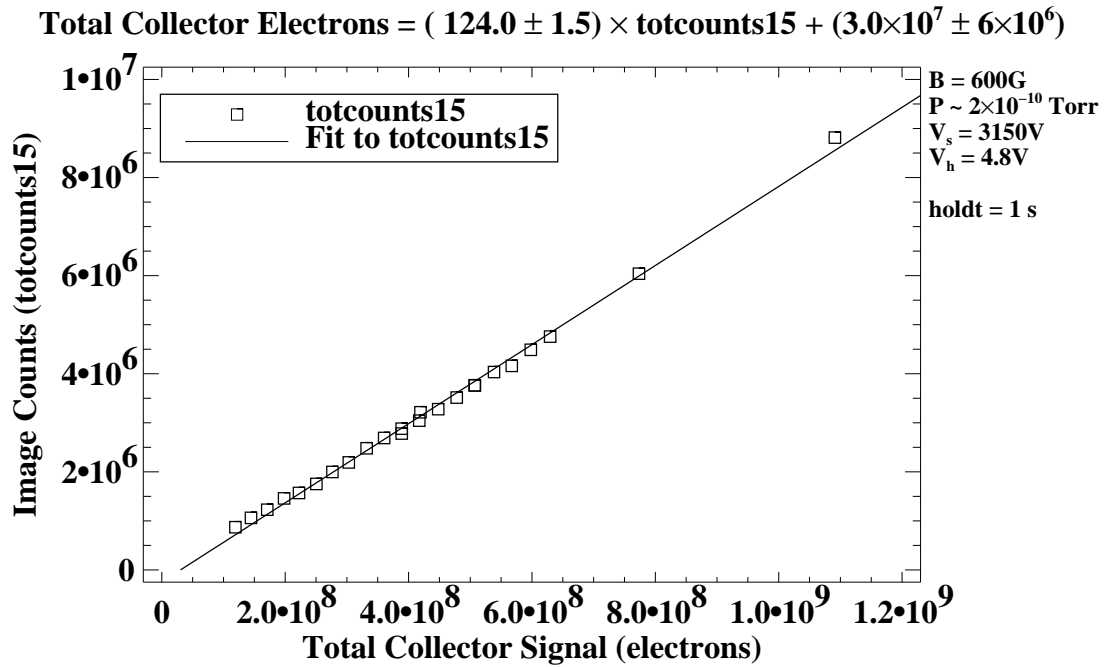


Figure 2.20: Image total counts vs. the measured number of electrons incident on the screen.

electrons further suggests that the number of image counts per electron is not a function of the incident electron flux.

If the screen is known to respond uniformly at all locations and have a weak dependence on the incident electron energy, the screen's response to the incident electron flux can be tested by varying the filament bias voltage V_b . At higher bias voltage V_b , the plasmas have a larger number of plasma electrons and therefore a higher plasma potential at $r = 0$. Figure 2.20 shows that the image total counts is proportional to the total charge collected by the screen when changing V_b . Increasing V_b also increases the initial mean-square radius of the trapped plasmas, causing them to sample more of the screen area. In Figure 2.20, the constant

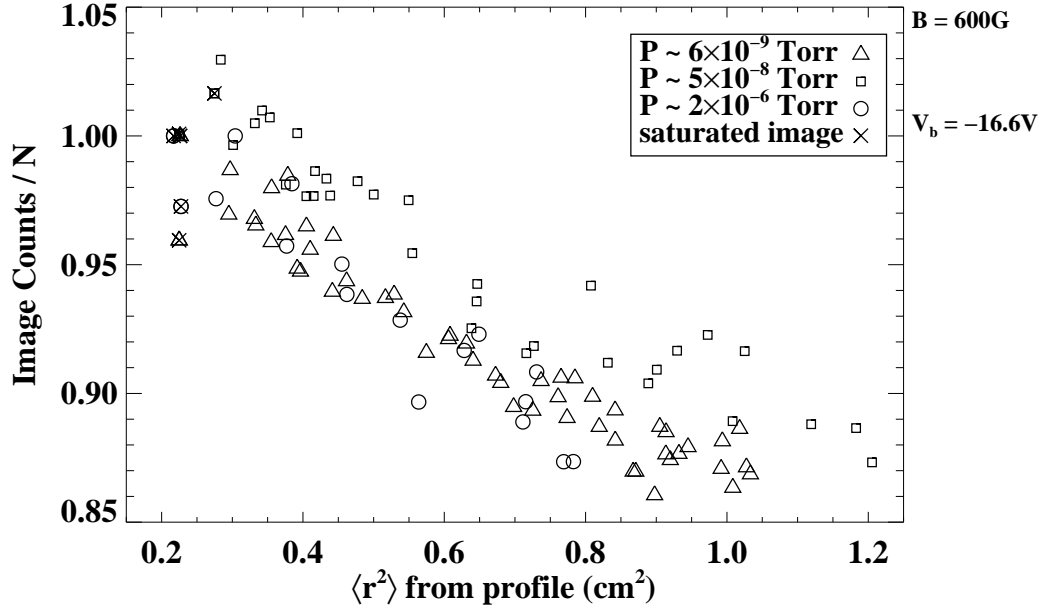


Figure 2.21: Image counts per electron for expanding plasmas. The plasmas expand with very little loss of charge, but the number of image counts per electron decreases by $\sim 15\%$. This is thought to be due to the noise level of the diagnostic. This data is calculated from the same data sets used to produce the late-time expansion rate points in Fig. 4.14.

of proportionality is 124.0 ± 1.5 electrons/(image count), and the offset is an indication of the minimum electron density that can be distinguished from the image noise at this screen bias voltage V_s .

Another way to test the uniformity of the screen is to measure plasmas that are expanding but not losing any charge. Figure 2.21 shows that the number of image counts per electron actually decreases as the plasma expands under the influence of background gas, but this decrease in image counts is not inconsistent with the uniform screen response suggested by Fig. 2.18 because of the noise level of the CCD camera. For example, approximating the axially integrated density profile as

$$c(r) = \frac{A}{\pi \langle r^2 \rangle} \exp \left[-\frac{r^2}{\langle r^2 \rangle} \right], \quad (2.5)$$

where A is a constant, and assigning the image total counts to be the number of counts above a noise level c_{noise} produces a similar 15% drop for the change in $\langle r^2 \rangle$ from $0.25 \text{ cm}^2 \rightarrow 1.0 \text{ cm}^2$ for a noise level of only $c_{\text{noise}} \approx 0.017 \times A$, which is not an unreasonable value. Essentially, as the plasma expands, more of the light emitted by the electrons is below the noise level of the CCD camera because the electrons are spread out radially, and the amount of measurable light decreases for the same number of electrons. This effect should also be present to a small degree in the test of screen uniformity using displaced plasmas in Fig. 2.18, since the plasmas continue to expand while the diocotron mode is growing. In that plot, the plasma is displaced from the trap axis more quickly at higher values of resistance R , and not at all for $R = 0$. The $R = 0$ data shows that plasma expansion accounts for a drop in the number of counts per electron of at most 5% over the course of the measurements. All of the plasmas represented in Fig. 2.18 were trapped for less than one second, and the $\lesssim 5\%$ drop in the number of counts per electron for the $R = 0$ data agrees with the drop for the subset of plasmas represented in Fig. 2.21 that were also trapped less than one second.

It is important to note that the test results displayed in Figures 2.18 – 2.21 do not unequivocally prove that the EDG phosphor screen has a uniform response across its face, a constant response with incident electron flux, and a weak response with incident electron energy. It is conceivable that complicated dependences in these three qualities could conspire to produce these same desirable characteristics, but it appears unlikely that this is the case.

Phosphor-Screen Density Diagnostic Details

The amplifier used to measure the number of plasma electrons collected by the screen (the same one used for the total collector) is coupled to the phosphor screen using five 4.7 nF, high-voltage ceramic capacitors in parallel (the amplifier has a 3.2 nF input capacitance). A 220 M Ω TigerTail resistor in series with the high-voltage power supply keeps the power supply from interfering on the measurement timescale. This RC circuit coupling the total collector amplifier to the phosphor screen is also used in the parallel temperature measurements.

The electronics controlling the voltage on trap electrode 6 were improved so the plasma could be released in approximately 0.65 μ s instead of 4.4 μ s. This improvement was necessary so the plasma would escape the trap in a much shorter time than it takes for the diocotron mode to send it through one azimuthal rotation, thereby avoiding discernible azimuthal smearing of the image. This was accomplished by replacing the Apex Microtechnologies PA05 amplifier that provided the voltage on the confining electrode 6 with a faster PA85 amplifier.

The interference filter in front of the camera has a central wavelength of 540 nm \pm 2 nm and a full width at half maximum of 30 nm \pm 6 nm, and was produced by Barr Associates. The 10-bit PULNiX TM-1010 CCD camera has 1024 \times 1024 pixels, and an individual pixel corresponds to a width of $1.150 \times 10^{-2} \pm 4 \times 10^{-5}$ cm at the phosphor screen ($R_w \approx 220.9$ pixels). The camera's electronic shutter is set to be open for 1/250 seconds to fully integrate the light from the phosphor. The phosphor coating has a characteristic fluorescence time of ~ 2 ms, is made with 1 μ m-size grains, and was assembled by Proxitronic. The generation III (GaAs) image intensifier is model number NE6010 from ITT Industries, has a resolution of 64 lp/mm, and amplifies the incident light by a factor of $\sim 3 \times 10^4$ fL/fc.

2.3 Temperature Diagnostics

Several methods have been developed for measuring plasma temperatures in Malmberg-Penning trap plasmas. Some methods give an average temperature for the entire plasma (non-destructively), while others give temperatures with varying degrees of spatial resolution (usually requiring destruction of the plasma). Plasma-averaged temperature diagnostics include: exciting plasma-frequency waves and measuring their dispersion relationship [MALMBERG and DEGRASSIE, 1975], measuring the power spectrum of temperature-dependent Trivelpiece-Gould modes [ANDEREGG *et al.*, 2003] (either naturally occurring or excited), and measuring the power transmitted through a spheroidal plasma near the $m = 1$ and $m = 2$ diocotron mode frequencies [AMORETTI *et al.*, 2003b]. Spatially resolved temperature diagnostics include the following: using an additional electromagnet to discriminate between the electrons' perpendicular energies in a collimated subset of the plasma (a 'magnetic beach' analyzer) [HYATT *et al.*, 1987; DEGRASSIE and MALMBERG, 1980; HYATT, 1988]; slowly releasing the plasma from the trap and measuring the escaped charge on-axis as a function of time [EGGLESTON *et al.*, 1992; BECK *et al.*, 1996], which gives the parallel temperature at $r = 0$ for a single plasma; and methodically changing the exit electrode potential to several voltages near the plasma potential (instead of to zero Volts) when releasing the plasma and using measurements of the number of electrons that escape as a function of the radius and the final confining voltage [EGGLESTON *et al.*, 1992] to determine the radial parallel temperature profile.

For the work presented in this thesis, parallel plasma temperatures at $r = 0$ are measured by slowly letting the plasma leak out of the trap. Perpendicular plasma

temperatures are inferred by fitting a thermal quasi-equilibrium radial density profile to the measured density profiles.

2.3.1 T_{\parallel} Measurement

On-axis, parallel temperature measurements are performed in a manner described by Eggleston [EGGLESTON *et al.*, 1992]. The voltage on confining electrode 6 (the “exit” electrode) is slowly increased, and both the number of electrons escaping the trap and the exit electrode voltage are recorded as functions of time (see Fig. 2.22). The exit electrode voltage is increased slowly enough to energy-analyze the plasma electrons, allowing the highest energy electrons to escape the trap first and the slower electrons to escape discernibly later. The measurements are fit using the approximate relationship

$$\frac{d \ln(Q_{\text{esc}})}{d(e\phi_c)} = \frac{-1.05}{T_{\parallel}}, \quad (2.6)$$

where Q_{esc} is the total amount of charge that has escaped, e is the charge of an electron, ϕ_c is the confining voltage at the trap axis, and T_{\parallel} is the parallel temperature in eV. A plot of $\ln(Q_{\text{esc}})$ versus ϕ_c for an EDG plasma is displayed in Fig. 2.23.

To measure the parallel temperature in this manner, the only additional equipment necessary for a basic Malmberg-Penning trap is a relatively fast, charge-sensitive amplifier, a circuit to slow the release of the plasma, and waveform digitizers to record the output signals. The amplifier circuit used to measure Q_{esc} for EDG was designed by Robert Marsala (PPPL) and debugged by Mr. Marsala and Hans Schneider (PPPL), and is shown in Figures 2.24–2.25. The amplifier is capacitively coupled to the biased phosphor screen using the same coupling circuit used

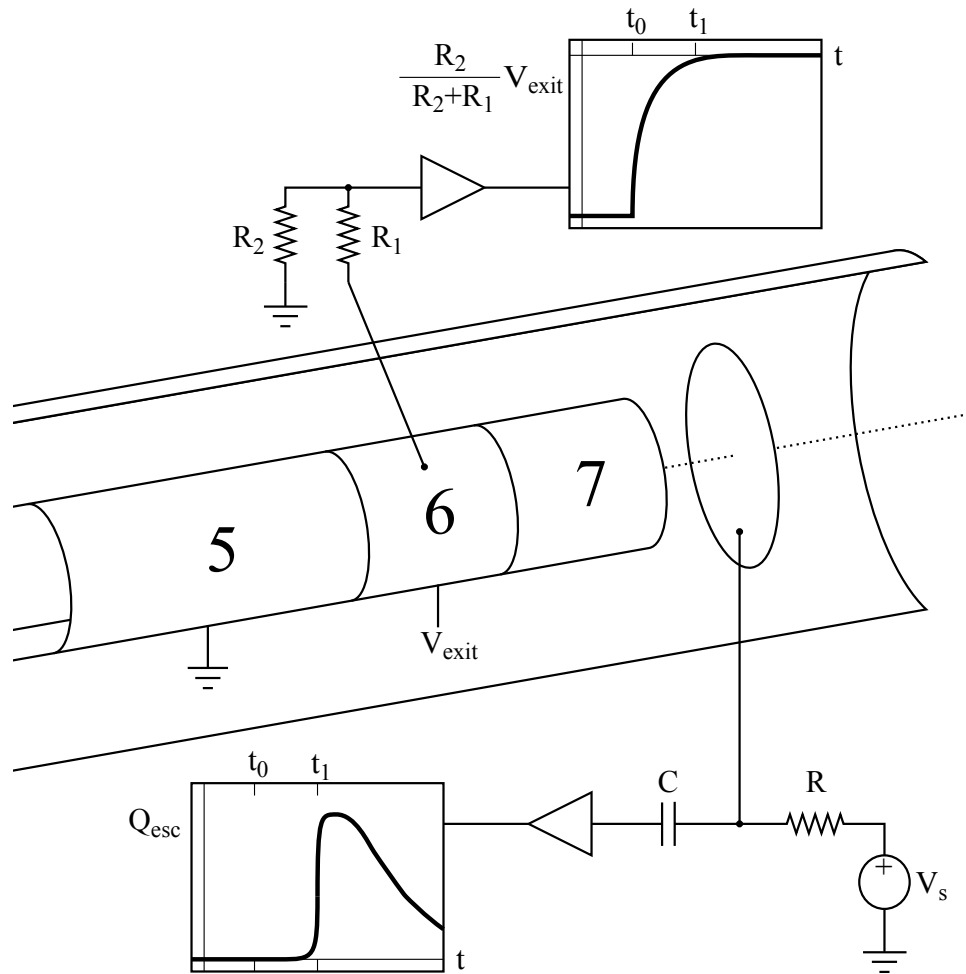


Figure 2.22: Temperature measurement diagram. A simple RC circuit (not shown) is used to slow the voltage change on electrode 6. Only the first 1–2% of the Q_{esc} curve is measured, because additional change in the plasma potential appreciably affects the effective confining voltage thereafter.

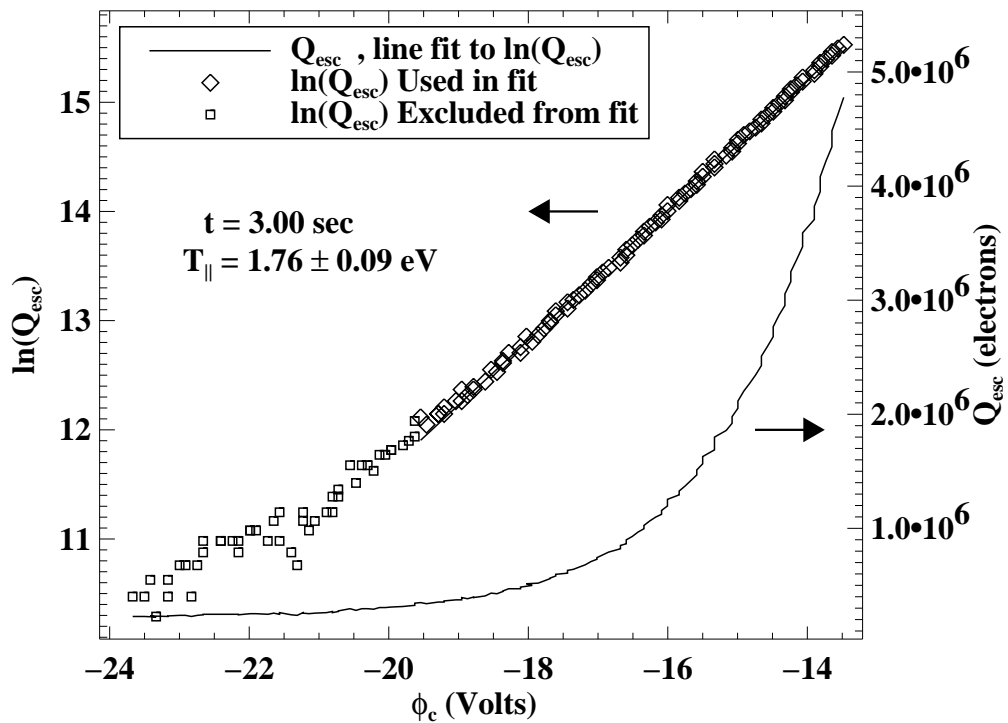


Figure 2.23: Total charge escaped vs. confining voltage as the plasma is released from the trap. The diamonds denote the data used in the fit. This data was taken at magnetic field $B = 600$ G, background gas pressure $P \sim 1 \times 10^{-10}$ Torr, filament heating voltage $V_h = 4.8$ V, and filament bias voltage $V_b = -16.6$ V.

for making total charge measurements with the screen, and a simple RC filter is used to slow the exit electrode voltage drop.

Equation (2.6) was derived [EGGLESTON *et al.*, 1992] for the first 1–2% of the electrons escaping from an idealized plasma column with flat ends [e.g., the plasma length $L(r, \theta) = L_0$], with locally Maxwellian parallel energy distributions, and measured by an electron collector that is small compared to the temperature gradient's radial length scale. However, it should also hold for plasmas with any end shape $L(r, \theta)$ if $\partial L(r, \theta)/\partial \phi_c$ is negligible, as implied by the form of Eqs. (2.7) and (2.14). Applying Eq. (2.6) to data where the aluminum-coated phosphor screen is the collector implicitly treats the plasma as though it had a uniform parallel temperature [$T_{\parallel}(r, \theta) = T_{\parallel 0}$], because the phosphor coating has a greater radius than the entire plasma. The parallel plasma temperature obtained is referred to as the on-axis temperature, however, because the electrons used in the measurement come predominantly from within ~ 6 Debye lengths of $r = 0$. This is because the vacuum confining potential produced by the cylindrical electrodes is weakest at the trap axis, where the plasma's space charge potential is also the strongest. Equation (2.6) only describes the first 1–2% of the electrons that escape because further charge loss appreciably affects the plasma potential and thus the effective potential energy difference that the electrons must overcome to escape the trap (Eq. 2.9).

Equation (2.6) may be computed relatively simply. The charge collected by an electrode at a given radius r and confining potential ϕ_c is represented as

$$Q_{esc}(r, \phi_c) = q \int_{A(r)} dA' L(r') n(r') \int_E^{\infty} \frac{dE'}{\sqrt{E'}} F(r', E'), \quad (2.7)$$

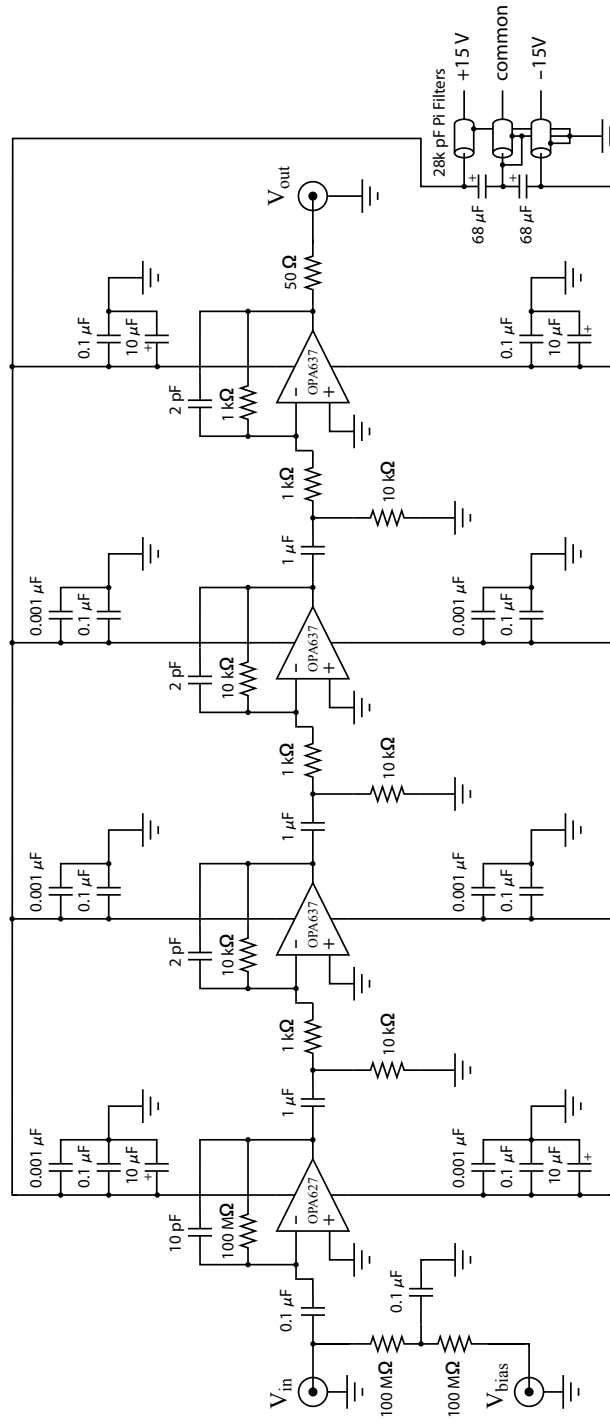


Figure 2.24: On-axis Temperature Diagnostic Amplifier (OTDA) circuit diagram.

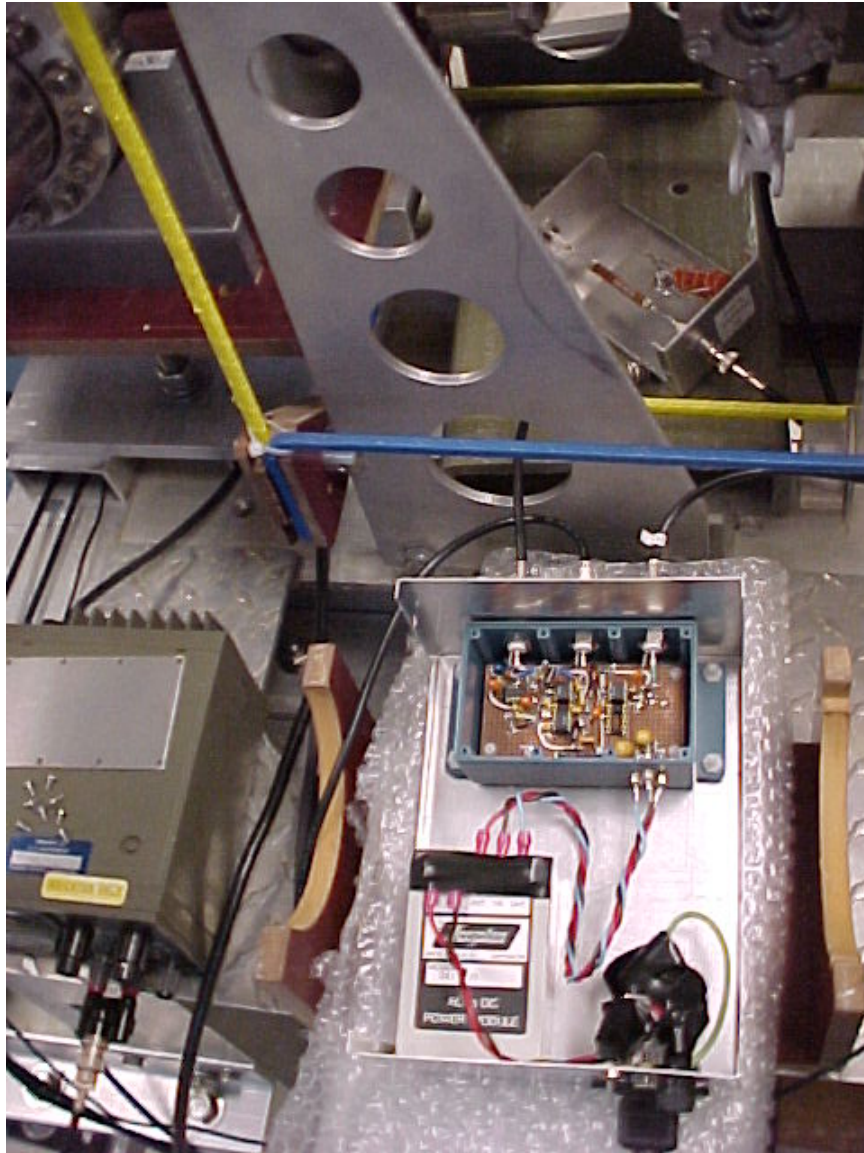


Figure 2.25: The coupling circuit (top), the On-axis Temperature Diagnostic Amplifier (bottom, on the bubble wrap), its HP power supply for biasing (left), and the vacuum feedthrough (top right, with white clips) appear in this image. The white plastic clips hold an aluminum foil shield around the floating MHV feedthrough to ground the amplifier circuit to the machine, reducing circuit noise. The bubble wrap helps reduce noise from vibrations caused by the cryopump.

where $A(r)$ is the area of the electrode located at the radial location r (in our case, $A(r)$ is the entire phosphor screen area and $r = 0$), $L(r)$ is the length of the column, q is the charge of an individual particle in the trap, $n(r)$ is the particle density, and $F(r', E')$ is the parallel energy distribution function with normalization

$$\int_0^\infty \frac{dE'}{\sqrt{E'}} F(r', E') = 1. \quad (2.8)$$

The lower limit on the energy integral in Eq. (2.7) is the threshold energy that a particle must have to escape the confining potential ϕ_c , specifically,

$$E(r, \phi_c) = q [\phi_c - \phi_p(r, \phi_c)], \quad (2.9)$$

where ϕ_p is the plasma potential of the charges remaining in the trap. The plasma potential is determined self-consistently from Poisson's equation,

$$\frac{1}{r} \frac{d}{dr} \left(r \frac{d}{dr} \phi_p(r, \phi_c) \right) = -4\pi q n(r) \left(1 - \frac{Q_{esc}(r, \phi_c)}{Q(r)} \right), \quad (2.10)$$

using the boundary conditions

$$\phi_p(R_w, \phi_c) = 0, \quad (2.11)$$

$$\frac{d}{dr} \phi_p(0, \phi_c) = 0. \quad (2.12)$$

Note that the effects of the radial dependence of the confining voltage are neglected in this derivation [$\phi_c(r) \rightarrow \phi_c$]. For a Maxwellian parallel energy distribution

$$F(r, E) = \frac{1}{\sqrt{\pi T_\parallel}} e^{-\frac{E}{T_\parallel}}, \quad (2.13)$$

Eq. (2.7) becomes

$$Q_{esc}(r, \phi_c) = q \int_{A(r)} dA' L(r') n(r') \operatorname{erfc} \left(\sqrt{\frac{E(r', \phi_c)}{T_\parallel}} \right) \quad (2.14)$$

where erfc is the complementary error function. For $E(r', \phi_c)/T_{\parallel} \gtrsim 2$, Eq. (2.14) becomes Eq. (2.6), with $\sim 5\%$ accuracy.

To measure the plasma temperature in this fashion, there are several fundamental criteria that must be satisfied: The rate at which the confining voltage on the exit electrode changes must be fast enough that the plasma doesn't have time to reestablish local Maxwellian energy distributions, but slow enough that the diagnostic can distinguish more-slowly-moving electrons near the exit electrode from faster-moving electrons that are further away or moving away from the exit electrode. In addition, the measurement must be complete before powerful instabilities that cause radial transport in non-monotonically-decreasing density profiles have time to grow and interfere as the plasma is hollowed out.

These necessary conditions can be expressed as

$$\frac{L}{v_{\parallel}}, \omega_p^{-1} \ll T_{\parallel} \left(\frac{dE}{dt} \right)^{-1} \ll \nu_{ee}^{-1}, \gamma_{\text{inst}}^{-1}, \quad (2.15)$$

where L is the characteristic plasma length, v_{\parallel} is the characteristic parallel velocity, $-(1/e)dE/dt$ is the time rate of change of the difference between the confining potential and the plasma potential [see Eq. (2.9)], ν_{ee} is the electron-electron collision frequency, and γ_{inst} is the growth rate of the hollow-profile instabilities. Using EDG parameters, these conditions become

$$3.6 \times 10^{-7} \text{ sec}, 4 \times 10^{-9} \text{ sec} \ll 1 \text{ eV} \left(\frac{dE}{dt} \right)^{-1} \ll 3 \text{ ms}, \gamma_{\text{inst}}^{-1}. \quad (2.16)$$

Given that the on-axis plasma potential plus a few times T is about 15eV, one obtains the condition

$$4.7 \mu\text{s}, 0.05 \mu\text{s} \ll \tau_{\text{ramp}} \ll 39 \text{ ms}, 15 \cdot \gamma_{\text{inst}}^{-1}. \quad (2.17)$$

The hollow-profile instabilities observed in other experiments did not affect those temperature measurements for $\sim 200\mu\text{s}$ [EGGLESTON *et al.*, 1992], restricting the characteristic ramping time to the range $47\mu\text{s} \ll \tau_{\text{ramp}} \ll \sim 200\mu\text{s}$.

2.3.2 Inferred T_{\perp} from Measured Density Profiles

The perpendicular electron temperatures reported in Fig. 2.11 are estimated by fitting an ideal, thermal quasi-equilibrium density profile [DAVIDSON and MOORE, 1996; O'NEIL and DRISCOLL, 1979] to the measured, axially integrated profiles. The thermal quasi-equilibrium density profile for these plasmas is [DAVIDSON and MOORE, 1996] [Eq. (3.48)]

$$n(r, t) = \hat{n}(t) \exp \left\{ \frac{e\phi(r, t) - e\hat{\phi}(t)}{T} - \frac{r^2}{\langle r^2 \rangle(t)} \left(1 + \frac{N_L e^2}{2T} \right) \right\} \quad (2.18)$$

where $\hat{n}(t)$ is the density at $r = 0$ as a function of time, $\phi(r, t)$ is the electrostatic potential (determined self-consistently from Poisson's equation), and $\hat{\phi}(t)$ is the electrostatic potential at $r = 0$. This thermal quasi-equilibrium profile shape describes expanding, infinite-length, azimuthally symmetric plasmas that enjoy global energy conservation and elastic electron-neutral collisions and have a spatially uniform temperature (see section 3.2). Poisson's equation can be recast in a form [O'NEIL and DRISCOLL, 1979] that shows the underlying profile shape is dependent on only one parameter,

$$\epsilon \equiv \frac{\omega_r \omega_c - \omega_r^2}{\hat{\omega}_p^2/2} - 1, \quad (2.19)$$

where $\omega_c = eB/m_e c$ is the electron cyclotron frequency, ω_r is the equilibrium plasma rotation frequency, and $\hat{\omega}_p$ is the plasma frequency at $r = 0$. ϵ is the only parameter necessary to distinguish the ideal density profiles. Example ideal profile shapes are shown in Fig. (2.26).

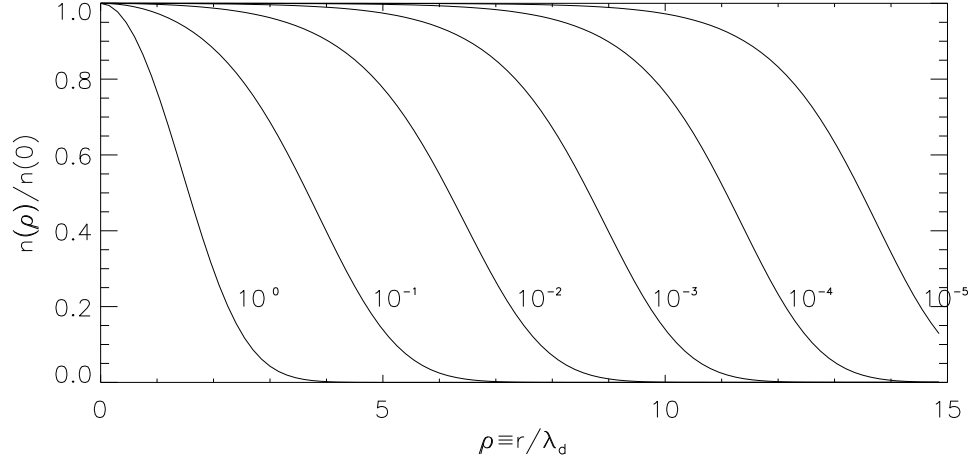


Figure 2.26: Thermal quasi-equilibrium profiles for different values of ϵ . The radial dimension ρ is normalized using the on-axis Debye length $\lambda_D \equiv \sqrt{T/4\pi n_0 e^2}$. (Reproduced from [CHAO, 1999], with permission.)

More precisely, the profiles used to fit the density profile data are numerical solutions of Eq. (2.18) and Poisson's equation. First, the cold radius of the plasma R_{cold} is estimated from the measured density profile according to $\hat{n} \pi R_{\text{cold}}^2 = N_L$. We also allow $\hat{n}(t)$ to vary when fitting the measured density profiles for simplicity, though in principle it should be identifiable from the data. Next, a Debye length is obtained from R_{cold} and the fitting parameter ϵ , using Davidson & Lund's numerical map of $(\lambda_D/R_{\text{cold}})^2$ versus ϵ (Fig. 2.27). [DAVIDSON and LUND, 1994]. Next, the equation

$$\frac{1}{\rho} \frac{\partial}{\partial \rho} \rho \frac{\partial}{\partial \rho} \psi = e^\psi - (1 + \epsilon) \quad (2.20)$$

(Eq. (50) of reference [O'NEIL and DRISCOLL, 1979]), where $\rho \equiv r/\lambda_D$,

$$\psi(\rho) \equiv \left(\frac{e\phi(\rho)}{T} \right) - \rho^2 \left(\frac{\epsilon + 1}{4} \right),$$

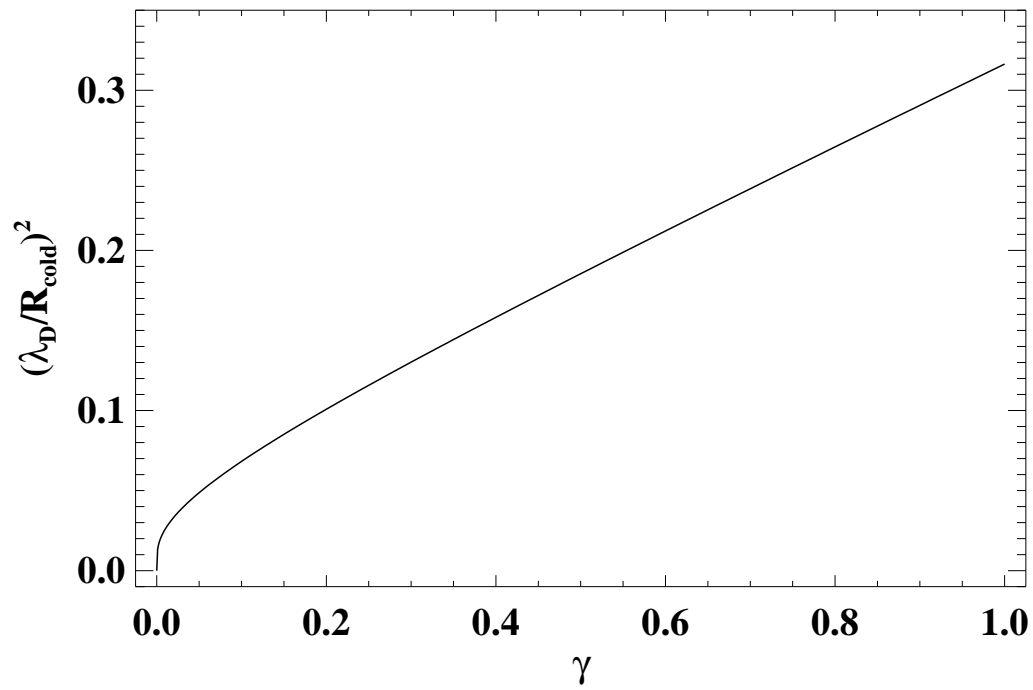


Figure 2.27: Plot of $\lambda_D^2/R_{\text{cold}}^2$ vs. ϵ for thermal quasi-equilibrium profiles (originally computed by Davidson & Lund [DAVIDSON and LUND, 1994]).

is solved numerically using the guess for ϵ and the Debye length. The resulting numerical density profile $n = \hat{n} \exp[\psi(\rho)]$ [O'NEIL and DRISCOLL, 1979] is compared with the data, and new guesses for ϵ and \hat{n} are made. The temperature is computed from the final estimated Debye length using \hat{n} .

2.4 Diocotron Mode Diagnostic

The $m = 1$ diocotron mode, one of the electrostatic surface waves supported in Malmberg-Penning trap plasmas, has density perturbations of the form $\delta n \sim \delta n(r)(\exp[i m \theta - i \omega t])$. The manifestation of this mode has been compared to an overall radial offset of the plasma column from the trap axis, where the displaced plasma rotates around the trap axis at the $m = 1$ diocotron mode frequency and continues to rotate about its own axis at the angular frequency ω_r .

The $m = 1$ diocotron mode amplitude and frequency as functions of time are observed by measuring the current induced to an azimuthally discontinuous electrode segment as the plasma rotates around the trap axis (see Fig. 2.28). The amplitude of the mode can be approximated from this current by using the expression for the current induced to an electrode segment by an off-axis, rotating, finite-length line charge ($R_p = 0$) [CLUGGISH, 1995; KAPETANAKOS and TRIVELPIECE, 1971]

$$I = \frac{2N_L \omega_0 e L_s}{\pi} \sum_{n=1}^{\infty} \sin(n\Delta\theta/2) \sin(n\omega_0 t) \times \left[\left(\frac{D}{R_w}\right)^n - 4 \left(\frac{R_w}{L_s}\right) \sum_{k=1}^{\infty} \frac{J_n(j_{nk} \frac{D}{R_w}) \sinh(j_{nk} \frac{L_s}{2R_w})}{(j_{nk})^2 J_{n+1}(j_{nk})} e^{-j_{nk} L_p / R_w} \right], \quad (2.21)$$

which is determined for an electrode segment described by the surface $\{r = R_w, \theta_o < \theta < \theta_o + \Delta\theta, z_o < z < z_o + L_s\}$. In Eq. (2.21), ω_0 is the infinite-length diocotron

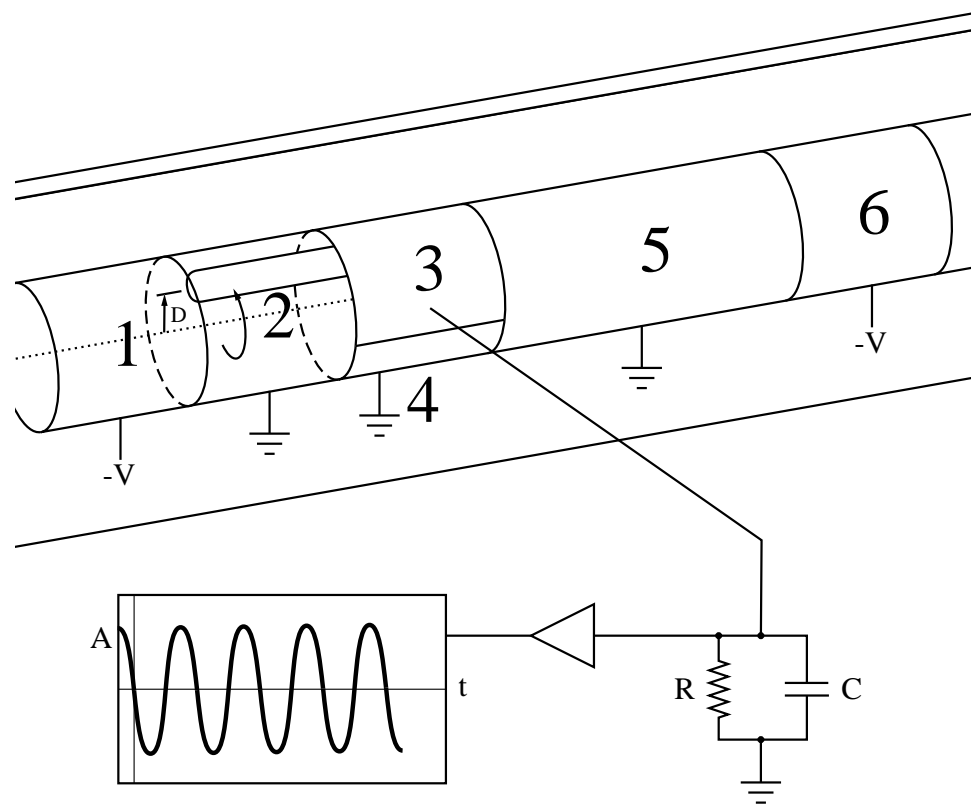


Figure 2.28: Diocotron mode diagnostic setup.

mode frequency, N_L is the line density, L_p is the length of the line charge, L_s is the axial length of the electrode segment (the “sector probe”), $\Delta\theta$ is the angular extent of the electrode segment, R_w is the inner radius of the trap electrode ($1/2 \times$ the trap I.D.), D is the displacement of the plasma axis from the trap axis, and j_{nk} is the k th zero of the Bessel function J_n . Equation (2.21) is a good approximation to the current induced if the plasma is rotationally symmetric, such that its electric field can be mimicked with a line charge.

The induced current is measured by recording the voltage across a resistor and capacitor that are in parallel and inserted between the electrode segment and the point of zero potential (“ground”), as shown in Fig. 2.28. To ensure that the diagnostic doesn’t resistively excite the $m = 1$ diocotron mode (see sections 3.4.2 and 5.1.2), this impedance is chosen to be almost purely reactive: $R = 100 \text{ M}\Omega$ and $C = 2.6 \text{ nF}$ (for $10 \text{ kHz} < \omega_0 < 80 \text{ kHz}$). The voltage is measured with a high-impedance amplifier ($Z_{\text{in}} \sim 10^{13} \Omega$), and recorded with a LeCroy 6810 CAMAC waveform recorder. To improve the signal-to-noise ratio, amplifiers¹ are connected to opposing electrode segments (electrodes 3 and 4) and the difference of the two signals is saved by the waveform recorder.

Data from the diocotron mode diagnostic give the growth rate of the diocotron mode $(1/D) dD/dt$, and either the line density if the displacement is known or the displacement if the line density is known. In Figure 2.29, the displacement calculated from diocotron-mode-diagnostic data using a line density estimated from the mode frequency is compared to the displacement measured from the density diagnostic images. The two diagnostics agree qualitatively in the range 0.05 cm

¹Assembled by Dr. Edward Chao and Dr. Stephen Paul

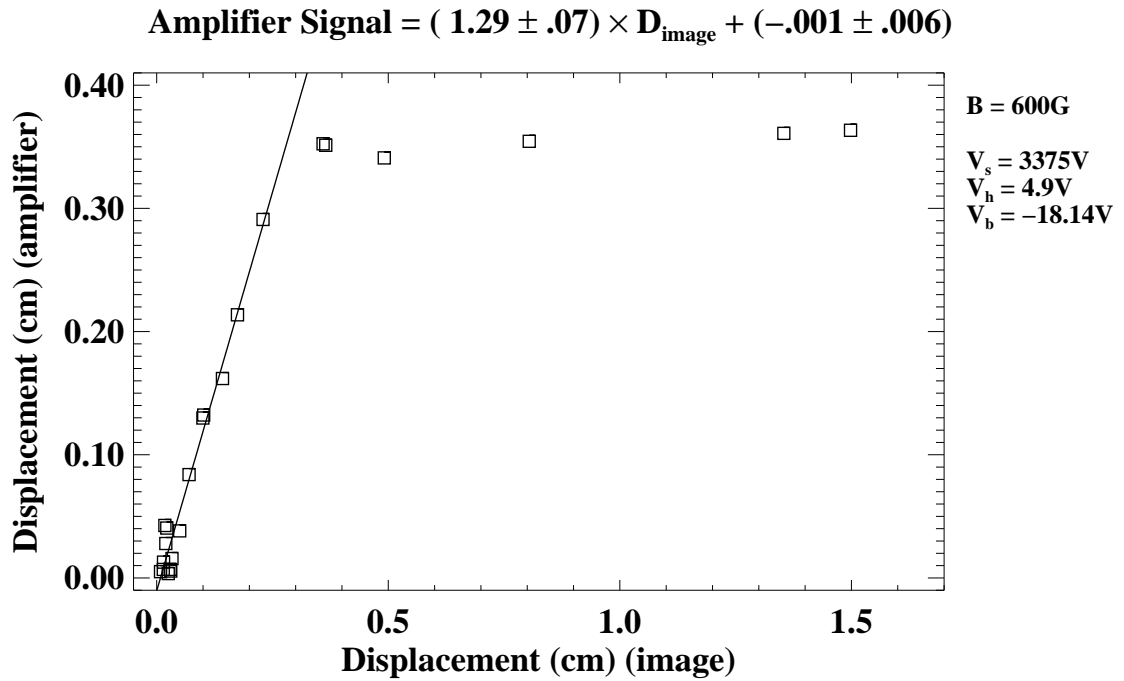


Figure 2.29: Displacement calculation comparison. The $m = 1$ diocotron mode displacement estimated from the diocotron mode diagnostic amplifiers' signals is calculated with a line density estimated from the mode frequency [using the value of $\langle r^2 \rangle$ at $t = 0$ from the density diagnostic images and the finite-length diocotron mode frequency relationship in Eq. (3.60)]. The displacements calculated from the images are estimated for the density values above 1/5 of the peak density value to best describe the large-amplitude modes that squash the plasma against the trap electrodes. The mode is excited using a resistor in series with one of the diocotron mode diagnostic amplifiers.

$< D < 0.3$ cm, but the diocotron mode amplifiers aren't able to measure displacements past $D \sim 0.3$ cm. Above this point, the plasmas in this data set were very distorted azimuthally, and were almost certainly in contact with the trap electrodes (including the electrodes the diocotron mode diagnostic amplifiers are connected to). At low displacements, the density diagnostic is not able to distinguish the displacement accurately due to its spatial resolution. It is not certain why the displacement measurements differ by $\sim 30\%$ in the range of qualitative agreement, but it is important to note that the estimated plasma line density used in this displacement calculation (and for most of the diocotron mode data analysis in this thesis) is for fixed values of $\langle r^2 \rangle(t = 0)$ and plasma length L_P , though the plasma is expanding during the evolution.

The displacement computation is not completely straightforward—inverting Eq. (2.21) is not an easy task. In addition, the effective voltage amplitude computed at each particular point in time is averaged over several diocotron mode periods according to $V_{\text{eff}}^2 = 2\langle V^2 \rangle$, since only around 10 data points are recorded per period. The displacement is therefore estimated by neglecting the finite-length-plasma terms in Eq. (2.21) (those proportional to R_w/L_s , which is acceptable for small displacements), squaring the equation $V = IZ$ [where $Z = (R)/(1 + i\omega RC)$ and I is given by Eq. (2.21)], and averaging over a diocotron mode period, resulting in

$$\frac{2\langle V^2 \rangle}{A^2} = \sum_{\text{odd}(n) \geq 1}^{\infty} \left(\frac{D}{R_w} \right)^{2n} \quad (2.22)$$

$$= \sum_{n=0}^{\infty} \left(\frac{D}{R_w} \right)^{2+4n} \quad (2.23)$$

$$= \frac{\left(\frac{D}{R_w} \right)^2}{1 - \left(\frac{D}{R_w} \right)^4} \quad (2.24)$$

where $A = 2N_L e L_s / (\pi C)$. The mode's growth rate can be conveniently estimated from the effective amplitude V_{eff} by taking the time derivative of Eq. (2.24) and dividing both sides by Eq. (2.24), resulting in

$$\frac{1}{V_{\text{eff}}} \frac{dV_{\text{eff}}}{dt} = \frac{1}{D} \frac{dD}{dt} \left[\frac{\sum_{n=0}^{\infty} (2n+1) \left(\frac{D}{R_w}\right)^{4n}}{\sum_{n=0}^{\infty} \left(\frac{D}{R_w}\right)^{4n}} \right] \quad (2.25)$$

$$= \frac{1}{D} \frac{dD}{dt} \left[\frac{1 + \left(\frac{D}{R_w}\right)^4}{1 - \left(\frac{D}{R_w}\right)^4} \right] \quad (2.26)$$

The factor in the square brackets is $41/40 = 1.025$ for $D/R_w = 1/3$ and $17/15 \approx 1.133$ for $D/R_w = 1/2$, which agrees with observations that plots of $d(\ln V_{\text{eff}})/dt$ and $d(\ln D)/dt$ appear quite similar.

2.5 Basic Equipment

The EDG device is evacuated using a Helix Technologies CryoTorr 8 cryopump (modified to use metal seals) and a Balzers TPU 180H Turbopump backed by a Leybold-Heraeus TriVac D8A roughing pump behind a zeolite trap. The turbopump has a rated pumping speed of 180 liters/sec. and the cryopump is rated to absorb nitrogen at a rate of 1500 liters/sec., water at 4000 liters/sec., and hydrogen at 2500 liters/sec. Pumping the vessel down from atmospheric pressure usually only results in a $\sim 2 \times 10^{-9}$ Torr vacuum, so heating tape and an aluminum foil tent are used to hold the machine at 125 – 150 °C for several days and drive water, hydrocarbons, and other polar molecules off the interior surfaces of the device (to “bake” it). The inner faces of the cylindrical electrodes used in the trap were vapor-coated with gold [MOORE, 1995] to reduce gas desorption inside the trap during plasma evolutions and to provide good electrical conductance. After baking, the

device regularly reaches pressures of $\sim 4 \times 10^{-10}$ Torr and sometimes well into the 10^{-11} Torr range (recently 3.3×10^{-11} Torr). The base pressure is quite sensitive, however, to the temperature in the room and the filament heating voltage, so both are kept as low as practical.

Changes in the background gas pressure are measured with two Balzers IMR 132 Bayard-Alpert nude ionization gauges, one near the cryopump with fair vacuum conductance to the trap and the other near the turbopump with decidedly worse vacuum conductance. A Leybold IE511 extractor gauge was added in late 2001 (before the small filament expansion rate experiments) to the good-conductance side to give better resolution in the $\sim 10^{-11}$ Torr range and a check on the performance of the ionization gauge. Unfortunately, this necessitated enclosing the Bayard-Alpert ionization gauge in a smaller, 3 3/8" tube, which heats up noticeably and produces a higher baseline reading. The ionization gauge on the poor-conductance side was also enclosed in a 3 3/8" tube to reduce stray light affecting the phosphor-screen diagnostic images. Accordingly, the much cooler extractor gauge is currently considered the most reliable indicator of the background gas pressure. It is also necessary to account for the facts that the gauges are roughly 5 times less sensitive to helium gas than they are to nitrogen and are also affected by the magnetic field.

The magnetic field is supplied with 28 water-cooled L2 coils [BONANOS, 1964] arrayed in a solenoidal configuration and driven by an EMI EMHP power supply and a Sorensen SRC 40-50 power supply. Three L2 coils on each end carry 2.7 times the current carried by the inner 22 coils, providing a more uniform magnetic field [Stowell, 1997] along the trap axis (Fig. 2.30). For the experiments using the scanning Faraday-cup density diagnostic, the magnetic field was aligned with the

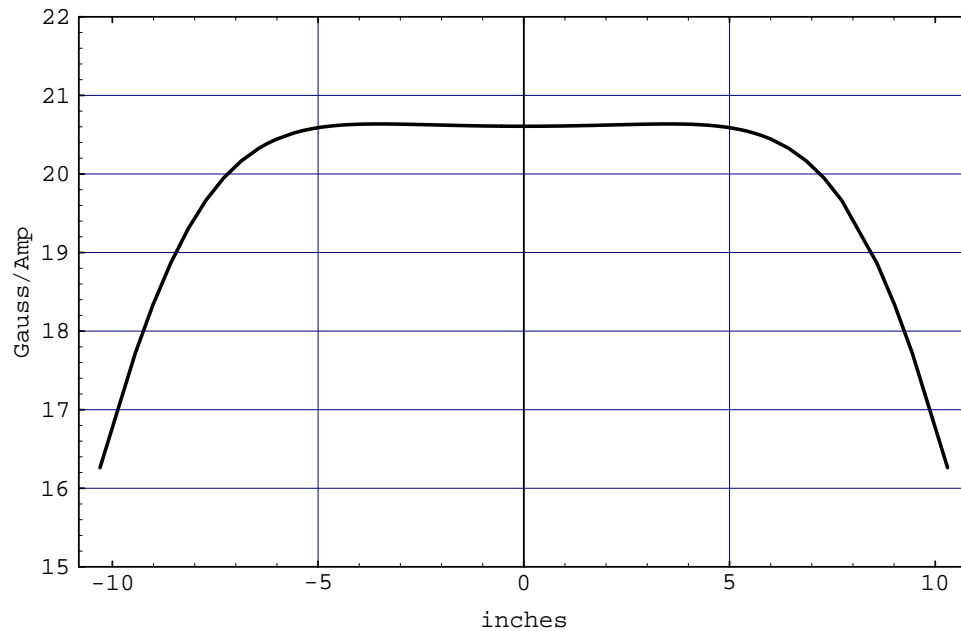


Figure 2.30: Predicted on-axis magnetic field produced per Ampere of central solenoid current as a function of axial distance from the center of the solenoid. (Reproduced from [CHAO, 1999], with permission.)

trap electrodes by centering the entire vacuum vessel inside the coil set, though this was later seen to be a non-ideal criterion. For the 2003 experiments with the phosphor-screen diagnostic, two orthogonal sets of Helmholtz-like trimming coils (adding magnetic field components perpendicular to the trap axis [MOORE, 1995]) were resurrected to simplify the alignment of the magnetic field with the trap electrodes' axis. Using the trimming coils, the trap is considered aligned when the initial diocotron mode amplitude is minimized, though a better criterion could be minimizing the plasma expansion rate [GILSON, 2001]. The better criterion proved to be an impractical method for the EDG device, though cursory measurements suggest that the two criteria coincide for the current filament placement. The trap electrodes are located axially within the solenoid in such a way to provide

a near-uniform field from the phosphor screen to the far end of the trapping region. Specifically, the center of the solenoid is set equidistant from the surface of the phosphor screen and the gap between electrodes 1 & 2. The parts of the vacuum vessel inside the solenoid are made of aluminum to minimize the effects of stainless steel components on the magnetic field structure.

The trap electrodes are made of OHFC copper and held together with Macor supports, long molybdenum support rods, and aluminum and molybdenum hardware (Fig. 2.3). The parts of the vacuum vessel containing the trap and the density diagnostic feedthroughs are aluminum, and the rest of the vessel is stainless steel. These materials were chosen to minimize interference with the imposed magnetic field from the solenoid and the influence of vacuum surface outgassing on the vessel base pressure.

To vary the background gas pressure, helium is usually fed into the chamber using a Vacuum Generators LVM 940 all-metal leak valve. Sufficient control to distinguish changes in plasma behavior in the 10^{-11} – 10^{-10} Torr range is enhanced by lowering the helium pressure behind the leak valve to < 10 Torr in a separate, vacuum-worthy gas reservoir.

Chapter 3

The Dynamics of Long, Warm

Plasmas in Malmberg-Penning Traps*

This chapter is a review of recent work describing long ($R_p/L_p \ll 1$), warm ($T \gtrsim 0.1$ eV) Malmberg-Penning trap plasmas that is relevant to the dynamics of EDG plasmas considered in this thesis. (R_p is the characteristic plasma radius, and L_p is the characteristic plasma length.) First, the good confinement of non-neutral plasmas in these traps (section 3.1.1) and the mechanisms that allow particles and energy to redistribute in the plasma (section 3.1.2) are described. Next, the properties of plasmas in thermal equilibrium and plasmas that are in a slowly changing, thermal quasi-equilibrium state are described (section 3.2). Then, the ways that field asymmetries in the trap can cause the plasma to expand (section 3.3.1) and the plasma expansion due to frequent collisions with gas molecules (section 3.3.2)

*This overview draws substantially from chapters 3 and 5 of reference [CHAO, 1999].

are discussed. Finally, the factors influencing the evolution of the $m = 1$ diocotron mode, an azimuthally propagating electrostatic wave, are detailed (section 3.4).

3.1 Particle Dynamics and Transport

3.1.1 Global Confinement

Plasmas with a single charged species do not suffer from ambipolar particle diffusion as neutral and partially neutralized plasmas do. It is not surprising, then, that these plasmas are confined more robustly than neutral plasmas are. To illustrate this, many authors have noted that conservation of angular momentum constrains the particle transport [O'NEIL, 1980b; MALMBERG *et al.*, 1982]. The total canonical angular momentum of a system of N charged particles may be written as

$$\mathbf{L} = \sum_j \mathbf{r}_j \times \mathbf{P}_j \quad (3.1)$$

$$L = \sum_j (P_j)_\phi r_j = \sum_j \left[m_j v_{\phi j} + \frac{q_j}{c} A_\phi(r_j) \right] r_j, \quad (3.2)$$

where \mathbf{P}_j is the j^{th} particle's canonical momentum, $v_{\phi j}$ is the particle's velocity in the azimuthal direction, q_j is the particle's charge, m_j is the particle's mass, and $A_\phi(r)$ is the magnetic vector potential in the azimuthal direction. In Malmberg-Penning traps, the magnetic field is uniform and in the axial direction (the diamagnetic field is usually negligible), so the magnetic vector potential is $A_\phi(r) \simeq Br/2$, and Eq. (3.2) becomes

$$L = \sum_j (P_j)_\phi r_j \simeq \sum_j \left[m_j v_{\phi j} r_j + \frac{q_j B}{c} \frac{r_j^2}{2} \right]. \quad (3.3)$$

For a sufficiently large magnetic field, the azimuthal particle velocity is small compared to the fast cyclotron orbits that the particles follow, and the first term in the sum may be neglected. (This criterion may be expressed as $(\omega_p/\Omega_c)^2 \ll 1$ [DAVIDSON, 1990].) For particles with the same charge $q_j = q$, Eq. (3.3) becomes

$$L \simeq \sum_j \frac{q_j}{c} \frac{B}{2} r_j^2 = \frac{q}{c} \frac{B}{2} \sum_j r_j^2. \quad (3.4)$$

To the extent that the system's total angular momentum L is conserved, its mean square radius $\langle r^2 \rangle \equiv \sum_j r_j^2 / N$ should also be approximately constant. A more comprehensive treatment [O'NEIL, 1980a; DAVIDSON, 1990] indicates that conservation of total canonical angular momentum and total energy are enough to guarantee that a significant fraction of the trapped particles will never be lost from a perfectly constructed Malmberg-Penning trap. Furthermore, azimuthally asymmetric electron plasmas have been stably trapped for ~ 10 seconds [NOTTE *et al.*, 1992] in *azimuthally asymmetric* traps, demonstrating that only a minimum energy state (for $E \times B$ drift dynamics) [O'NEIL and SMITH, 1992] and not conservation of total canonical angular momentum is necessary for good non-neutral plasma confinement and stability.

In non-neutral plasma experiments, angular momentum can be extracted from or imparted to the system by inherent asymmetries in the confining electric or magnetic fields [EGGLESTON and CARRILLO, 2003; KABANTSEV *et al.*, 2003], intentionally applied asymmetries in the confining fields [HOLLMANN *et al.*, 2000a; ANDEREGG *et al.*, 1998; HUANG *et al.*, 1997], intentionally applied radiation (lasers), and collisions between the plasma particles and neutral gas molecules [DAVIDSON and MOORE, 1996; DOUGLAS and O'NEIL, 1978]. Indeed, by judiciously applying time-varying, azimuthally asymmetric voltages to segmented trap electrodes, enough angular momentum can be continuously added to the plasma to overcome

the effects of inherent trap imperfections. Plasmas have been trapped for arbitrarily long periods of time (weeks) with this technique [HUANG *et al.*, 1997].

3.1.2 Evolution Towards Thermal Equilibrium

When a collection of electrons is initially trapped in a Malmberg-Penning trap, there is no reason to believe that it is in a thermal equilibrium state. However, there is a series of internal plasma processes that will eventually rearrange any initial electron distribution into a thermal equilibrium state if not contravened by external influences.

First, the electrons evolve according to the Vlasov equation

$$\frac{\partial}{\partial t} f(\mathbf{r}, \mathbf{p}) + \mathbf{p} \cdot \frac{\partial}{\partial \mathbf{r}} f(\mathbf{r}, \mathbf{p}) + q \left(\mathbf{E} + \frac{\mathbf{v}}{c} \times \mathbf{B} \right) \cdot \frac{\partial}{\partial \mathbf{p}} f(\mathbf{r}, \mathbf{p}) = 0, \quad (3.5)$$

and reach a collisionless equilibrium through collective, nonlinear processes [DAVIDSON and KRALL, 1970]. For example, electron plasmas with non-monotonically-decreasing (hollow) radial density profiles are unstable to internal diocotron instabilities, and internal $m = 1$ modes have been observed to grow exponentially in experiments [DRISCOLL, 1990; DRISCOLL and FINE, 1990]. The density reorganization can sometimes take hundreds of cold plasma rotation times $\tau_{E \times B} \sim 2\pi/\omega_{E \times B}$, where $\omega_{E \times B} = cE/rB \approx \omega_p^2/2\Omega_c$, for initially hollow density profiles [HUANG *et al.*, 1995]. The cold plasma rotation time is $\tau_{E \times B} < 4\mu\text{s}$ for typical EDG plasmas.

After a quasi-steady Vlasov equilibrium state is achieved, local thermal equilibrium is established along the magnetic field on electron-electron collision timescales. Collisions between particles whose guiding centers are less than two gyroradii apart ($\rho = |\mathbf{R}_1 - \mathbf{R}_2| \lesssim 2r_L$) first eliminate any non-Maxwellian features in the

energy distributions and then remove any residual anisotropy between the perpendicular and parallel temperatures. The electron velocity distribution functions approach Maxwellian distributions in the characteristic time given by the electron-electron Coulomb collision frequency [O'NEIL and DRISCOLL, 1979]

$$\nu_{ee} = \frac{16}{15} \sqrt{\pi} n \bar{v} b^2 \ln \left(\frac{r_L}{b} \right) \quad (3.6)$$

where n is the electron density, $\bar{v} = \sqrt{T/m_e}$ is the thermal velocity at equilibrium, m_e is the electron mass, $b = e^2/T$ is the classical distance of closest approach, $r_L = \bar{v}/\Omega_c$ is the electron cyclotron radius, and $\ln(r_L/b)$ is the Coulomb logarithm. Concurrently, the perpendicular and parallel electron temperatures will start equilibrating at approximately the anisotropic temperature equilibration rate [BECK *et al.*, 1996; HYATT *et al.*, 1987]

$$\nu_T = \frac{8}{5} \sqrt{\pi} n \bar{v} b^2 \ln \left(\frac{r_L}{b} \right) = \frac{3}{2} \nu_{ee}, \quad (3.7)$$

which describes the equilibration of T_{\perp} and T_{\parallel} in reasonably warm plasmas. The Coulomb logarithm in Eqs. (3.6) and (3.7) is changed from the more familiar $\ln(\lambda_D/b)$ (which appeared in the original calculation of ν_T [ICHIMARU and ROSENBLUTH, 1970]), since $r_L \ll \lambda_D$ in typical non-neutral plasmas instead of $r_L \gg \lambda_D$. ($\lambda_D = \sqrt{T/4\pi n e^2}$ is the Debye length.) This replacement is generally acceptable when applying transport theory results for low-magnetic-field regimes ($r_L \gg \lambda_D$) to high-magnetic-field regimes ($r_L \ll \lambda_D$) [MONTGOMERY *et al.*, 1974; SILIN, 1962]. For EDG parameters, $1/\nu_T \approx 4$ ms, so local thermal equilibrium should exist in less than 24 ms after the particles are trapped (including $\sim 500 \times \tau_{E \times B}$ for reaching a collisionless equilibrium).

Finally, radial transport of energy, angular momentum, and particles across the magnetic field should allow the plasma to reach an overall (“global”) thermal equilibrium. The transport in laboratory non-neutral plasmas is usually dominated by Debye-length-scale interactions between particles instead of classical, gyroradius-scale collisions (again, because $r_L \ll \lambda_D$). These Debye-length-scale interactions [DUBIN, 1998; DRISCOLL *et al.*, 2002] (often called $\mathbf{E} \times \mathbf{B}$ drift collisions) allow particles with guiding centers that are well-separated across the magnetic field to exchange energy and angular momentum, and this transport is more effective than gyroradius-scale collisional transport in these plasmas because of the larger number of particles involved. The transport coefficients for Debye-length-scale interactions and gyroradius-scale collisions are compared in Fig. 3.1. The overall transport coefficients include both of these effects and also the effects of lightly damped plasma waves:

$$D_{\text{total}} = D_{E \times B} + D_{\text{class}} \quad (3.8)$$

$$\nu_{\text{total}} = \nu_{E \times B} + \nu_{\text{class}} + \nu_{\text{waves}} \quad (3.9)$$

$$(\chi_T)_{\text{total}} = (\chi_T)_{E \times B} + (\chi_T)_{\text{class}} + (\chi_T)_{\text{waves}}. \quad (3.10)$$

In a Debye-length-scale interaction, two particles that are a transverse distance ρ from one another feel the electric fields from each other as they pass axially, and accordingly $E \times B$ drift across the magnetic field. Their adiabatic invariants $\mu_i = (1/2)m_e(v_\perp)_i^2 / B$ are unchanged to first order in r_L/ρ , but the particles do exchange parallel energy. Because the particles make many velocity-scattering collisions in 1-D along the magnetic field with other particles, they will likely approach one another again and experience multiple, correlated, Debye-length-scale interactions before they are separated [DUBIN, 1997]. This is accounted for with the factor

	Diffusion D	Kinematic Viscosity $\frac{\eta}{nm}$	Thermal Diffusivity $\frac{2}{5n} \kappa$
$\rho < r_L$ classical velocity scattering	$\frac{4}{3} \sqrt{\pi} \nu_c r_L^2 \ln\left(\frac{r_L}{b}\right)$ Longmire & Rosenbluth 1956	$\frac{2}{5} \sqrt{\pi} \nu_c r_L^2 \ln\left(\frac{r_L}{b}\right)$ Longmire & Rosenbluth 1956 Simon 1955	$\frac{16}{15} \sqrt{\pi} \nu_c r_L^2 \ln\left(\frac{r_L}{b}\right)$ Rosenbluth & Kaufman 1958
$r_L < \rho < \lambda_D$ 3-D v_z -resonant	$2 \alpha \sqrt{\pi} \nu_c r_L^2 \ln\left(\frac{\bar{v}}{\Delta v_{\min}}\right) \ln\left(\frac{\lambda_D}{r_L}\right)$ O'Neil 1985, Dubin 1997 Anderegg 1997	$0.59 \alpha \sqrt{\pi} \nu_c \lambda_D^2 \ln\left(\frac{\bar{v}}{\Delta v_{\min}}\right)$ O'Neil 1985, Dubin 1997 Driscoll 1988	$0.48 \nu_c \lambda_D^2$ Dubin & O'Neil 1997 Hollmann 2000
$r_L < \rho < \lambda_D$ 2-D axially- averaged	$8 \pi^2 \frac{f_b}{r \omega'_{E \times B} } \nu_c r_L^2 \ln\left(\frac{r}{d}\right)$ Dubin & Jin 2001 Anderegg 2002	$16 \pi^2 \frac{f_b}{r \omega'_{E \times B}} \nu_c d^2 g\left(\frac{2d}{r}\right)$ Dubin & O'Neil 1998 Kriesel 2001	n.a.

Table 3.1: Comparison of transport coefficients for classical, gyroradius-scale collisions and Debye-length-scale interactions. This table was compiled in [DRISCOLL *et al.*, 2002]. Note the enhancement of the 3-D kinematic viscosity and thermal diffusivity over their classical values by approximately $(\lambda_D/r_L)^2 / \ln(r_L/b)$, and that both 2-D coefficients are proportional to the number of axial bounces a particle makes during an interaction $N_b \equiv f_b / (r \omega'_{E \times B})$, where $f_b = \bar{v} / 2L_p$ is the bounce frequency, $\omega_{E \times B} = cE/rB$, and $r \omega'_{E \times B} = r \partial \omega_{E \times B} / \partial r = S(r)$ is the rotational shear. ν_c is the “collision” frequency $\nu_c \equiv n \bar{v} b^2$, d is the predicted radial interaction distance $d = 2r_L N_b (\partial L_p / \partial r)$, and $g(2d/r)$ is a collision integral. The coefficient α is either $\alpha = 3$ or 1, depending on the collisionality and the rotational shear.

α in Fig. 3.1. If the background shear in the plasma rotation profile is low, then $\alpha \simeq 3$. (The time for the particles to be sheared apart by the background plasma motion, $|\rho(\partial/\partial r)\omega_{E \times B}|^{-1}$, where $\omega_{E \times B} = cE/rB$, has to be much greater than the time for the correlated interactions to occur.) For larger shear, where the pairs of particles are limited to only one collision, $\alpha = 1$. If the plasma is sufficiently energetic that the interacting particles make many axial bounces at the ends of the trap before they are separated, the fast axial motion of the particles can be averaged away and the dynamics becomes a 2-D (perpendicular) evolution of charged rods [DUBIN and O'NEIL, 1998].

Debye-length-scale interactions in EDG plasmas should cause transport described by the 3-D transport coefficients from Fig. 3.1, specifically, the characteristic diffusion coefficient [DUBIN, 1997; ANDEREGG *et al.*, 1997a,b]

$$D = 2 \alpha \sqrt{\pi} \nu_c r_L^2 \ln\left(\frac{\bar{v}}{\Delta v_{\min}}\right) \ln\left(\frac{\lambda_D}{r_c}\right), \quad (3.11)$$

the characteristic kinematic viscosity [DUBIN, 1997]

$$\nu = \frac{\eta}{nm_e} = 0.59 \alpha \sqrt{\pi} \nu_c \lambda_D^2 \ln\left(\frac{\bar{v}}{\Delta v_{\min}}\right), \quad (3.12)$$

and the characteristic thermal diffusivity [DUBIN and O'NEIL, 1997; HOLLMANN *et al.*, 2000b]

$$\chi_T = \frac{2}{5n} \kappa = 0.48 \nu_c \lambda_D^2, \quad (3.13)$$

where ν_c is the common ‘‘collision’’ frequency $\nu_c \equiv n \bar{v} b^2$, $\alpha \simeq 3$ is the enhancement from multiple, correlated collisions, and Δv_{\min} is the minimum relative axial velocity between the two particles where integration over unperturbed orbits is valid. The quantity Δv_{\min} may be limited by shear in the plasma rotation or by velocity-scattering collisions with other particles. Velocity-scattering collisions

are responsible for limiting Δv_{\min} in a near-equilibrium plasma, giving $\Delta v_{\min} \sim (D_v \sqrt{r_L \lambda_D})^{1/3}$, where D_v is the velocity-space diffusion coefficient $D_v \sim n \bar{v}^3 b^2$. κ is the coefficient of heat transport, and η is the coefficient of shear viscosity.

The associated energy flux Γ_E is

$$\Gamma_E = -\kappa \frac{\partial T}{\partial r} \quad (3.14)$$

and the radial particle flux Γ_n is [DUBIN, 1998]

$$\Gamma_n = n v_r = -\frac{c}{eB} \frac{1}{r^2} \frac{\partial}{\partial r} r^3 \eta \frac{\partial}{\partial r} \omega_r, \quad (3.15)$$

where $\omega_r = \omega_{E \times B} + \omega_{\text{dia}}$ is the total, fluid rotation frequency, $\omega_{E \times B} = cE/rB$, and $\omega_{\text{dia}} = (c/enrB) \nabla(nT)$. The plasma has a uniform rotation frequency at all radii in thermal equilibrium due to the plasma's intrinsic radial electric field, and the viscous momentum transport reduces shear in the rotation frequency profile by rearranging the particles until they have an equilibrium density profile.

An estimate of the order of magnitude of the characteristic energy transport time across the field may be made by combining the equation for energy transport²

$$\frac{\partial}{\partial t} \left(\frac{3}{2} n T \right) = -\nabla \cdot \Gamma_T = \nabla \cdot \kappa \nabla T \quad (3.16)$$

with the thermal diffusivity in Eq. (3.13). Making the replacements

$$\begin{aligned} \frac{\partial}{\partial r} T &\rightarrow \frac{\sqrt{2}}{R_p} T \\ r &\rightarrow \frac{R_p}{\sqrt{2}} \\ \frac{\partial}{\partial r} &\rightarrow \frac{1}{\lambda_D}, \end{aligned} \quad (3.17)$$

²This form of the energy transport equation [DUBIN, 1998] neglects the rotational kinetic energy of the plasma and weak sources of heating, such as interaction with field asymmetries, heating of the plasma with oscillating applied confinement fields (particularly "rotating wall" fields [HOLLMANN *et al.*, 2000a]), and collisions with hot neutral gas molecules.

one obtains

$$\frac{1}{\tau_T^{E \times B}} \sim \frac{5}{3} (0.48) \nu_c \left(\sqrt{2} \frac{\lambda_D}{R_p} \right). \quad (3.18)$$

Similarly, the particle transport time may be estimated by combining the particle transport (continuity) equation

$$\frac{\partial n}{\partial t} = -\nabla \cdot \Gamma_n \quad (3.19)$$

with Eqs. (3.12) and (3.15). Making the replacements

$$\begin{aligned} \frac{\partial}{\partial r} \omega_r &\rightarrow \frac{\sqrt{2}}{R_p} \omega_r \\ \omega_r &\rightarrow \omega_{E \times B} = \frac{cE}{rB} \approx \frac{\omega_p^2}{2\Omega_c} \\ r &\rightarrow \frac{R_p}{\sqrt{2}} \\ \frac{\partial}{\partial r} &\rightarrow \frac{1}{\lambda_D}, \\ \Delta v_{\min} &\rightarrow \left(n \bar{v}^3 b^2 \sqrt{r_L \lambda_D} \right)^{1/3}, \end{aligned} \quad (3.20)$$

gives

$$\frac{1}{\tau_n^{E \times B}} \sim (0.59 \alpha \sqrt{\pi}) \left(\frac{2}{3} \pi \right) \nu_c \left(\frac{c}{B} \right)^2 \ln \left(n b^2 \sqrt{r_L \lambda_D} \right) n m_e. \quad (3.21)$$

For comparison, the gyroradius-scale transport coefficients with the replacements

$$\begin{aligned} \frac{\partial}{\partial r} \omega_r &\rightarrow \frac{\sqrt{2}}{R_p} \omega_r \\ \frac{\partial}{\partial r} T &\rightarrow \frac{\sqrt{2}}{R_p} T \\ \omega_r &\rightarrow \omega_{E \times B} = \frac{cE}{rB} \approx \frac{\omega_p^2}{2\Omega_c} \\ r &\rightarrow \frac{R_p}{\sqrt{2}} \\ \frac{\partial}{\partial r} &\rightarrow \frac{1}{r_L} \end{aligned} \quad (3.22)$$

become

$$\frac{1}{\tau_T^{\text{class}}} \sim \frac{16}{9} \sqrt{\pi} \nu_c \ln\left(\frac{r_L}{b}\right) \left(\sqrt{2} \frac{r_L}{R_p}\right) \quad (3.23)$$

$$\frac{1}{\tau_n^{\text{class}}} \sim \frac{2}{5} \sqrt{\pi} (2\pi) \nu_c \ln\left(\frac{r_L}{b}\right) \left(\frac{c}{B}\right)^2 n m_e. \quad (3.24)$$

From these order-of-magnitude estimates, we see that the energy transport time for the Debye-length-scale interactions is approximately a factor of $\tau_T^{\text{class}}/\tau_T^{E \times B} = (15/16)(0.48/\sqrt{\pi})(\lambda_D/r_L)(1/\ln(r_L/b))$ smaller than the classical value. The density profile relaxes with a characteristic time $\tau_n^{\text{class}}/\tau_n^{E \times B} = (5/2)(0.59\alpha) \ln(nb^2\sqrt{r_L\lambda_D})/\ln(r_L/b)$ times smaller than the time estimated for gyroradius-scale collisions.

Using the EDG-typical parameters $n_0 \sim 1.2 \times 10^7/\text{cm}^3$, $T \sim 1 \text{ eV}$, and $B = 600 \text{ G}$, the values obtained for these characteristic times are

$$\tau_T^{E \times B} \sim 0.4 \text{ s}$$

$$\tau_T^{\text{class}} \sim 0.5 \text{ s}$$

$$\tau_n^{E \times B} \sim 29 \text{ s}$$

$$\tau_n^{\text{class}} \sim 77 \text{ s},$$

giving $\tau_T^{\text{class}}/\tau_T^{E \times B} \sim 1$ and $\tau_n^{\text{class}}/\tau_n^{E \times B} \sim 3$. While the characteristic energy transport time for Debye-length-scale interactions is close to the classical transport time, the modified density profile relaxation time is nearly a factor of three shorter than its classical value. The short times for energy transport are reassuring, since EDG plasmas are only observed for fewer than 30 seconds. The new Debye-length-interaction estimate for the particle transport time $\tau_n^{E \times B}$, however, is still fairly long compared to the apparent relaxation time from experiments. This suggests that either some other effect is responsible for the apparently thermal quasi-equilibrium profiles (see section 3.2) observed in EDG, or, more likely, that our crude estimate

does not sufficiently describe the true rates because of their dependence on the details of the density and temperature profiles.

Both the viscosity and thermal diffusivity can be additionally enhanced by the local emission and remote absorption of lightly damped plasma waves [ROSENBLUTH and LIU, 1976; WARE, 1993], which allow transport of energy and momentum at distances much greater than a Debye length. This mechanism is only expected to become the dominant means of energy transport in Malmberg-Penning trap plasmas when $R_p \geq 10^2 \lambda_D$ and the dominant means of momentum transport when $R_p \geq 10^3 \lambda_D$, [DUBIN and O'NEIL, 1997], neither of which are true of the EDG plasma regime.

3.2 Thermal Equilibrium and Thermal Quasi-Equilibrium Plasmas

The thermal equilibrium distribution function [DAVIDSON and LUND, 1994; DAVIDSON, 1990; DAVIDSON and KRALL, 1970] for an infinite-length, non-neutral plasma confined by a uniform magnetic field is

$$f(r, \mathbf{p}) = n_0 \left(\frac{m_e}{2\pi T} \right) \exp \left[-\frac{H - \omega_r L_z}{T} \right]. \quad (3.25)$$

In Equation (3.25), H is the single particle Hamiltonian

$$H = \frac{\mathbf{p}^2}{2m_e} - e\phi(r), \quad (3.26)$$

L_z is the single particle canonical angular momentum

$$L_z = p_\phi r + \frac{-e}{c} A(r) r = p_\phi r - \frac{eB}{2c} r^2, \quad (3.27)$$

and the electrostatic potential $\phi(r)$ is obtained self-consistently from Poisson's equation

$$\frac{1}{r} \frac{\partial}{\partial r} r \frac{\partial}{\partial r} \phi = 4\pi e n(r), \quad (3.28)$$

where $n_0 \exp[e\phi(0)/T]$ is the density at $r = 0$ and T is the electron temperature (in ergs). The fluid rotation frequency ω_r is one of the two roots

$$\omega_r^\pm \equiv (\Omega_c/2) \left\{ 1 \pm \sqrt{1 - \frac{2\hat{\omega}_p^2}{\Omega_c^2} (1 + \epsilon)} \right\}, \quad (3.29)$$

determined from radial force balance on a fluid element, which can be written in the form

$$\omega_r \Omega_c - \omega_r^2 \geq \hat{\omega}_p^2/2, \quad (3.30)$$

$$\frac{\omega_r \Omega_c - \omega_r^2}{\hat{\omega}_p^2/2} \equiv 1 + \epsilon. \quad (3.31)$$

In Equations (3.29) and (3.31), $\Omega_c = eB/m_e c$ is the electron cyclotron frequency, and $\hat{\omega}_p$ is the plasma frequency $\hat{\omega}_p^2 = 4\pi n e^2/m_e$. The radial density profile, obtained from the integral $n(r) = \int d^3p f(r, \mathbf{p})$, becomes

$$n(r) = n_0 \exp \left\{ -\frac{1}{T} \left[-e\phi(r) + \frac{m_e}{2T} \omega_r (\Omega_c - \omega_r) r^2 \right] \right\} \quad (3.32)$$

for an isotropic, Maxwellian particle energy distribution [$\phi(r)$ is again given by Eq. (3.28)].

Using this equation for $n(r)$, the expressions for the mean-square radius

$$\langle r^2 \rangle = \frac{\int r dr d\theta r^2 n(r, \theta, z)}{\int r dr d\theta n(r, \theta, z)} \quad (3.33)$$

and the average angular momentum $\langle L_z \rangle$ (at a constant temperature T) become [DAVIDSON and LUND, 1994]

$$\langle r^2 \rangle_{\text{eq}} = \frac{2T + e^2 N_L}{m_e (\omega_r \Omega_c - \omega_r^2)} \quad (3.34)$$

and

$$\langle L_z \rangle = m_e(\omega_r - \Omega_c/2)\langle r^2 \rangle_{\text{eq}}. \quad (3.35)$$

where $N_L = \int r dr d\theta n(r, \theta)$. Equation (3.35) can be solved for the rotation frequency ω_r , and the result inserted into Eq. (3.34) to obtain expressions for ω_r and $\langle r^2 \rangle_{\text{eq}}$ in terms of the measured quantity T and the conserved quantities N_L and $\langle L_z \rangle$. Equation 3.34 may also be solved directly to obtain the plasma's rotation frequency, which at low densities ($\omega_p^2/\Omega_c^2 \ll 1$) [DAVIDSON and LUND, 1994] becomes

$$\omega_r = \frac{1}{\langle r^2 \rangle} \frac{N_L e^2}{m_e \Omega_c} \left(1 + \frac{2T}{N_L e^2} \right), \quad (3.36)$$

The quantity $\omega_r(\Omega_c - \omega_r)$ in Eq. (3.32) may be replaced using Eq. (3.34) to express the thermal equilibrium density profile in the useful form

$$n(r) = \hat{n}(t) \exp \left\{ \frac{e\phi(r, t) - e\hat{\phi}(t)}{T} - \frac{r^2}{\langle r^2 \rangle_{\text{eq}}} \left(1 + \frac{N_L e^2}{2T} \right) \right\} \quad (3.37)$$

where $\hat{n}(t)$ is the density at $r = 0$ and $\hat{\phi}(t)$ is the electrostatic potential at $r = 0$.

In the pressure range where electron-neutral collisions occur much less frequently than electron-electron Coulomb collisions ($\nu_{en} \ll \nu_{ee}$), the electron-electron collisions (described in section 3.1.2) should keep the plasma temperature uniform even though the plasma is slowly losing angular momentum to the neutral gas. This plasma state may be called thermal quasi-equilibrium, since the the plasma is slowly expanding with time. Fluid equations have been used to model this quasi-equilibrium by considering the expansion of an ideal, infinite-length, azimuthally symmetric electron plasma in the presence of background gas [DAVIDSON and MOORE, 1996; DAVIDSON and CHAO, 1996b]. The electron-neutral collisions included in the evolution are elastic, occur at a constant frequency ν_{en} , and appear as a drag on the system in the fluid momentum equation

$$\frac{d\mathbf{v}}{dt} = -\frac{T}{nm_e} \nabla n - \frac{e}{m_e} \left(\mathbf{E} + \frac{1}{c} \mathbf{v} \times \mathbf{B} \right) - \nu_{en} \mathbf{v}. \quad (3.38)$$

First, the dv/dt “inertial” term is neglected, restricting subsequent solutions to slowly rotating plasmas where $\omega_r \ll \Omega_c$. \mathbf{E} is determined from Poisson’s equation,

$$\frac{1}{r} \frac{\partial}{\partial r} r \frac{\partial}{\partial r} \phi = 4\pi en \quad (3.39)$$

$$-(\partial\phi/\partial r)\hat{\mathbf{r}} = \mathbf{E}. \quad (3.40)$$

Equations (3.38) and (3.40) combine to give the radial and azimuthal particle fluxes:

$$nV_r = -\frac{\nu_{en}}{(\nu_{en}^2 - \Omega_c^2)} \frac{1}{m_e} \left(T \frac{\partial n}{\partial r} - ne \frac{\partial \phi}{\partial r} \right), \quad (3.41)$$

$$nV_\phi = -\frac{\Omega_c}{(\nu_{en}^2 - \Omega_c^2)} \frac{1}{m_e} \left(T \frac{\partial n}{\partial r} - ne \frac{\partial \phi}{\partial r} \right). \quad (3.42)$$

Note that, predictably, $V_r \rightarrow 0$ as $\nu_{en} \rightarrow 0$, and (perhaps not so predictably)

$V_r = V_\phi \cdot (\nu_{en}/\Omega_c)$. With the expression for the radial particle flux, the plasma’s mean-square radius can be obtained [DAVIDSON and MOORE, 1996] from the fluid continuity equation

$$\frac{\partial}{\partial t} n - \frac{1}{r} \frac{\partial}{\partial r} (rnV_r) = 0, \quad (3.43)$$

$$\int_0^{R_w} dr 2\pi r r^2 \left(\frac{\partial}{\partial t} n - \frac{1}{r} \frac{\partial}{\partial r} (rnV_r) \right) = 0, \quad (3.44)$$

$$\frac{d}{dt} \langle r^2 \rangle = \frac{2}{N_L} \int dr 2\pi r rnV_r, \quad (3.45)$$

giving

$$\frac{d}{dt} \langle r^2 \rangle = \frac{2N_L e^2}{m_e} \frac{\nu_{en}(t)}{\Omega_c^2 - \nu_{en}^2(t)} \left(1 + \frac{2T(t)}{N_L e^2} \right) \quad (3.46)$$

The only quantities on the right hand side of Eq. (3.46) that vary with time (in an infinite-length plasma) are the temperature T and the electron-neutral collision frequency ν_{en} , since the plasma’s electrostatic potential energy is transferred to the

particles' kinetic energy as the plasma expands. Nonlinear evolution of the mean-square radius has been predicted [DAVIDSON and CHAO, 1996b] using Eq. (3.46), conservation of energy, and neglecting the temperature dependence of ν_{en} .

It is important to note that Eq. (3.46) is valid for all uniform-temperature plasmas with density profiles satisfying Eqs. (3.41), (3.43), and (3.39), even those that are not thermal quasi-equilibrium density profiles. If the plasma is in thermal quasi-equilibrium, the additional constraint

$$\frac{\partial}{\partial t} \left(\frac{2\pi n \langle r^2 \rangle}{N_L} \right) = 0 \quad (3.47)$$

applies, where $\eta \equiv 2\pi n \langle r^2 \rangle / N_L$ is essentially a normalized radial density profile called the profile shape function. Combining Eqs. (3.41), (3.43), (3.47), and (3.46), the thermal quasi-equilibrium density profile may be expressed as the solution to

$$n(r, t) = \hat{n}(t) \exp \left\{ \frac{e\phi(r, t) - e\hat{\phi}(t)}{T} - \frac{r^2}{\langle r^2 \rangle(t)} \left(1 + \frac{N_L e^2}{2T} \right) \right\} \quad (3.48)$$

and Poisson's equation (Eq. 3.39) [DAVIDSON and MOORE, 1996]. Again, $\hat{n}(t)$ is the density at $r = 0$ as a function of time, $\phi(r, t)$ is the electrostatic potential determined self-consistently from Poisson's equation, and $\hat{\phi}(t)$ is the electrostatic potential at $r = 0$. This solution has the same form as the thermal equilibrium density profile in Eq. (3.37), which was obtained from the thermal equilibrium distribution $f(r, \mathbf{p})$ [with the identifications $n_0 \rightarrow \hat{n}(t) \exp\{-e\hat{\phi}(t)/T(t)\}$ and $\langle r^2 \rangle_{\text{eq}} \rightarrow \langle r^2 \rangle(t)$]. The addition of electron-electron Coulomb collisions allows the plasma's mean-square radius $\langle r^2 \rangle(t)$ to increase with time according to Eq. (3.46). In addition, Davidson and Moore showed that an expanding, thermal, quasi-equilibrium state maximizes the plasma entropy, and both electron-electron collisions and electron-neutral collisions eventually cause the plasma to relax to it.

3.3 Non-Ideal Plasma Expansion

3.3.1 Asymmetry-Induced Plasma Expansion

Imperfections in the trap fields allow the plasma to expand much more quickly than is expected from the influence of background gas molecules alone. Trap imperfections were first suspected to influence the plasma dynamics at low pressures ($\nu_{en} \ll \nu_{ee}$) in the initial measurements of pressure-induced plasma expansion [MALMBERG and DRISCOLL, 1980], and this suspicion was confirmed when a more carefully constructed trap (with fewer mechanical misalignments and better materials) produced greatly reduced transport [DRISCOLL *et al.*, 1986]. This transport took a characteristic time $\tau_{n0/2} \propto (L_p/B)^{-2}$, where $\tau_{n0/2}$ is the time for the electron density at $r = 0$ to drop by a factor of 2.

Part of the asymmetry-induced transport is due to single-particle effects, where particles whose motion is resonant with an asymmetry experience greater cross-field drifts than non-resonant particles [EGGLESTON and O'NEIL, 1999]. It is clear that individual particles participate in the transport because the $\tau_{n0/2} \propto (L_p/B)^{-2}$ scaling seen for plasmas was reproduced in a test particle experiment where the bulk of the plasma was replaced with a biased wire at $r = 0$ and the electron density was low enough that $\lambda_D > R_w$ [EGGLESTON, 1997].

The predicted radial flux [EGGLESTON and O'NEIL, 1999] for a plasma in the “resonant plateau” regime, where frequent velocity-scattering collisions knock particles out of resonance with the asymmetry before they bounce once in the asymmetry potential ($\nu_{\text{eff}} \gg \omega_b$), was calculated to be

$$\Gamma_{\text{plateau}} = - \sum_{l,m,\omega} \frac{n}{\sqrt{2\pi\bar{v}^2}} \frac{L_p}{|l|} \left| \frac{cm\phi_{l,m,\omega}(r)}{rB_z} \right|^2 \times \left[\frac{1}{n} \frac{dn}{dr} + \frac{1}{T} \frac{dT}{dr} \left(x^2 - \frac{1}{2} \right) + \sqrt{2} \frac{l\pi}{L_p} \frac{r\Omega_c}{m\bar{v}} x \right] e^{-x^2}, \quad (3.49)$$

where $n = n(r)$ is the electron density, $\bar{v} = \sqrt{T/m}$, $T \neq T(r)$, $x = v_{\text{res}}/\sqrt{2}\bar{v}$, $v_{\text{res}} = (L_p/l\pi)(\omega - m\omega_{E \times B})$, $\omega_{E \times B} = cE/rB$ is the azimuthal $E \times B$ rotation frequency, and $\phi_{l,m,\omega}(r)$ is the Fourier amplitude of an asymmetry mode with axial mode number $l = k_z L_p/\pi$, azimuthal mode number m , and angular frequency ω . The effective collision frequency is $\nu_{\text{eff}}^3 \approx \nu_{ee}(l\pi\bar{v}/L_p)^2 = \nu_{ee}l^2\omega_b^2$, where $\omega_b = \pi\bar{v}/L_p$ is the axial bounce frequency. The radial flux Γ_{plateau} was shown to be in good qualitative but not quantitative agreement with experiments where m , l , ω , B , dn/dr , the axial wire bias ϕ_{cw} (which produces E_r), and $\phi_{l,m,\omega}(r)$ were varied [EGGLESTON and CARRILLO, 2003, 2002].

The flux for the “banana” regime, where particles make multiple bounces in the asymmetry potential ($\nu_{\text{eff}} < \omega_b$) and the characteristic particle transport length is the banana width, was heuristically determined to be

$$\Gamma_{\text{banana}} = - \sum_{l,m,\omega} \frac{n}{\sqrt{2\pi}} \frac{\nu_{ee} \left(\frac{L}{l\pi} \right)^2 \left(\frac{m\bar{v}}{r\Omega_c} \right)^2 \left(\frac{e\phi_{l,m,\omega}(r)}{T} \right)^{1/2}}{\left\{ 1 - \left(\frac{mL}{l\pi} \right)^2 \left(\frac{1}{r\Omega_c} \right) \left(\frac{d\omega_{E \times B}}{dr} \right) \right\}^{3/2}} \times \left[\frac{1}{n} \frac{dn}{dr} + \frac{1}{T} \frac{dT}{dr} \left(x^2 - \frac{1}{2} \right) + \sqrt{2} \frac{l\pi}{L} \frac{r\Omega_c}{m\bar{v}} x \right] e^{-x^2}, \quad (3.50)$$

but has not been verified experimentally.

In addition to single-particle effects, collective effects can also contribute to asymmetry-induced transport. This has been demonstrated [KABANTSEV *et al.*, 2003; KABANTSEV and DRISCOLL, 2003a] by trapping particles in an imposed electric asymmetry potential and exciting trapped-particle modes in the presence of additional imposed electric or magnetic “tilt” asymmetries ($m = 1$, $k_z = \pi/L_p$).

The normalized asymmetry-induced expansion rate was convincingly determined to scale with the trapped-particle mode damping rate for this particular configuration according to [KABANTSEV *et al.*, 2003; KABANTSEV and DRISCOLL, 2003c]

$$\nu_p \equiv \frac{1}{\langle r^2 \rangle} \frac{d\langle r^2 \rangle}{dt} \approx 6.3 \times 10^{-5} \gamma_a \left(\frac{N_L^{\text{tr}}}{N_L} \right) \left(\frac{eN_L^2}{B} \right) \left(\frac{L_p}{R_w} \right)^2 [\underline{\alpha}_B + \underline{\alpha}_E]^2 \quad (3.51)$$

where ν_p is the normalized expansion rate, γ_a is the trapped-particle mode damping rate, (N_L^{tr}/N_L) is the fraction of trapped particles, $\underline{\alpha}_B$ is the magnetic asymmetry tilt $\underline{\alpha}_B = (B_x/B_z)\hat{x} + (B_y/B_z)\hat{y}$, and $\underline{\alpha}_E$ is the electric asymmetry tilt $\underline{\alpha}_E \propto (V_x/2eN_L)\hat{x} + (V_y/2eN_L)\hat{y}$. The implied transport mechanism is that particles will become trapped axially in an electric asymmetry potential, and a trapped particle mode will imperceptibly grow. Some of the trapped particles the mode has promoted to a larger radius will undergo velocity scattering collisions that convert them to passing particles, and they will effectively take a radial step. These passing particles will in turn be trapped at the larger radius and again moved further out by the mode and collisions. The damping rates measured in experiments with electrically trapped particles and $m = 1$, $k_z = \pi/L_p$ magnetic asymmetries are in quantitative agreement with the theoretical description of the trapped particle mode damping [HILSABECK *et al.*, 2003] and readily reproduced in computer simulations [MASON, 2003].

Particles trapped in magnetic asymmetry potentials also contribute to the asymmetry-induced expansion, but the nature of the trapped particle modes in this case have not been determined or measured. The preliminary scaling for magnetically trapped particles with additional “tilt” asymmetries is [KABANTSEV *et al.*, 2003]

$$\nu_p^{(M)} \propto \left(\frac{N_L^{\text{tr}}}{N_L} \right)^0 \left(\frac{eN_L^2}{B} \right) \left(\frac{L_p}{R_w} \right)^2 [\underline{\alpha}_B + \underline{\alpha}_E]^2, \quad (3.52)$$

which, surprisingly, is not a function of the trapped particle fraction. The normalized expansion rate scalings for both electrically and magnetically trapped particles were determined by imposing a trapping potential at the axial center of the plasma, so they don't necessarily apply directly to cases with axially offset or multiple trapping asymmetries (such as ripple in the magnetic field). Even so, the measurements show $\nu_p \propto \gamma_a/B \propto B^{-1.5}-B^{-2}$ for electrically trapped particles, $\nu_p \propto \alpha_E L_p^2 \propto L_p^2$ for electrically trapped particles in the presence of a magnetic tilt asymmetry, and $\nu_p \propto \alpha_E L_p^2 \propto L_p^{-2}$ for electrically trapped particles in the presence of an electric "tilt" asymmetry, and the first two scalings agree with the $\tau_{n0/2} \propto (L_p/B)^{-2}$ scaling measured in earlier studies. Overall, the experiments suggest that axial trapping of particles is critical for asymmetry-induced transport, and that magnetically trapped particles interacting with additional magnetic asymmetries are responsible for the inherent asymmetry-induced transport due to collective effects in existing traps (though the $\tau_{n0/2} \propto (L_p/B)^{-2}$ scaling is consistent with both equations 3.51 and 3.52).

Asymmetry-induced expansion is the dominant particle transport mechanism at low pressures ($P < 10^{-8}$ Torr in EDG), and may fortunately be treated as an offset for pressure-induced expansion since it has no explicit scaling with pressure.

3.3.2 Plasma Evolution at Higher Pressures

For pressures where the electron-neutral collision frequency is much greater than the electron-electron collision frequency ($\nu_{en} \gg \nu_{ee}$), Douglas and O'Neil postulated that an infinite-length plasma expands with the characteristic time scale

[DOUGLAS and O'NEIL, 1978]

$$\tau_{\text{exp}} = \frac{1}{\nu_{en}} \frac{\Omega_c^2}{\omega_p^2} = \frac{1}{2} \frac{1}{\nu_{en}} \frac{\Omega_c}{\omega_{E \times B}} \quad (3.53)$$

from the form of the Boltzmann equation expanded in orders of $1/B$. This characteristic time has also been shown to describe plasmas where $\nu_{en} \ll \nu_{ee}$ using fluid equations [DAVIDSON and MOORE, 1996]. The time for the electron density at $r = 0$ to drop by a factor of two, $\tau_{n_0/2}$, and the time for the total number of electrons N to drop by a factor of two, $\tau_{N/2}$, were indeed measured to increase linearly with pressure in this regime [MALMBERG and DRISCOLL, 1980; DEGRASSIE and MALMBERG, 1980], though the plasmas used for the measurements did not extend radially to the trap electrodes. The equation for the plasma expansion rate (Eq. (3.46)) in section 3.2, which was determined from the fluid equations (3.38)–(3.45) and assumes $\nu_{en} \ll \nu_{ee}$ [equivalently, $T \neq T(r)$], matches Eq. (3.53) in the limit $T \rightarrow 0$ with the identifications $\langle r^2 \rangle \rightarrow R_{\text{cold}}^2 = N_L / (\pi \int dz n(r = 0, \theta, z))$ and $1/\tau_{\text{exp}} \sim (1/\langle r^2 \rangle) d\langle r^2 \rangle / dt$. Applying either Eq. (3.53) or Eq. (3.46) to data in the regime $\nu_{en} \gg \nu_{ee}$ effectively ignores the effects of temperature gradients in the expanding plasma. In this regime, temperature gradients are expected to arise [DOUGLAS and O'NEIL, 1978] because more-energetic particles escape the trap (radially) more quickly than less-energetic particles do and the plasma doesn't have enough time to thermally equilibrate.

The electron-neutral collision frequency ν_{en} may be represented as

$$\nu_{en} = n_n \int_0^\infty dv \sigma v P(v) \equiv n_n \langle \sigma v \rangle \quad (3.54)$$

where n_n is the neutral gas density, σ is the momentum-transfer collision cross section of the gas molecules to electron impact [Eq. (A.3)], v is the electron velocity, $P(v)$ is the probability distribution function giving the fraction of electrons with

electron velocity v , and the “volumetric collision rate” $\langle\sigma v\rangle$ is essentially the volume a typical particle sweeps through between collisions. The electron-neutral collision frequency in EDG can be estimated using the volumetric collision rates $\langle\sigma v\rangle$ for Maxwellian $P(v)$ (reproduced from Dr. Chao’s thesis in Appendix A) and an estimate for n_n that treats the neutral molecules as an ideal, room-temperature gas:

$$n_n = \frac{P}{T_n} = P[\text{Torr}] \cdot 3.22 \times 10^{16} \quad (3.55)$$

The point where $\nu_{en} \approx \nu_{ee}$ is $P \approx 1.2 \times 10^7$ Torr in EDG for a 1 eV plasma with $B = 600$ G and $n_0 \approx 1 \times 10^7 \text{ cm}^{-3}$.

Equations regarding the behavior of the plasma in the pressure range where the electron-neutral collision frequency and the electron-electron Coulomb collision frequency are similar in magnitude ($\nu_{en} \sim \nu_{ee}$) have been obtained by Malmberg and Driscoll [MALMBERG and DRISCOLL, 1980], though they do not take into account the effects of Debye-length-scale interactions (see section 3.1.2) on the energy transport.

3.4 $m = 1$ Diocotron Mode Evolution

Diocotron modes are low-frequency ($\omega \ll \omega_{pe} \ll \Omega_c$), electrostatic waves that propagate azimuthally across the magnetic field in non-neutral Malmberg-Penning trap plasmas. The density and potential perturbations for an infinite-length plasma are of the form

$$\delta n \sim \delta n(r) \exp[i(m\phi - \omega_\infty t)], \quad (3.56)$$

where m is the azimuthal mode number, and ω_∞ is the mode frequency. The frequency of small-amplitude ($D/R_w \ll 1$) $m = 1$ modes was determined to be

[LEVY, 1968; DAVIDSON, 1990]

$$\omega_\infty = \frac{2ecN_L}{R_w^2 B} \quad (3.57)$$

using a perturbative analysis. The $m = 1$ diocotron mode may also be described as a radial displacement D from the trap axis of an otherwise unperturbed plasma. The plasma is then in a dynamical equilibrium state, and the plasma axis rotates around the trap axis in the $\mathbf{E} \times \mathbf{B}$ direction at the mode frequency (nominally, ω_∞).

3.4.1 $m = 1$ Diocotron Mode Frequency

The $m = 1$ mode frequency in finite-length plasmas is predicted to be higher than the infinite-length-plasma estimate ω_∞ in Eq. (3.57). Considering the plasma to be in the off-axis dynamical equilibrium, the frequency for a constant-density, constant-temperature plasma is predicted to be [FINE and DRISCOLL, 1998]

$$\frac{\omega_1}{\omega_\infty} = 1 + \left(\frac{R_w}{L_p}\right) \left[\frac{j_{01}}{2} \left(\frac{1}{4} + \ln \left(\frac{R_w}{R_p} \right) + \frac{T}{N_L e^2} \right) - 0.671 \right], \quad (3.58)$$

where j_{01} is the first zero of the Bessel function $J_0(x)$. The term $0.671(R_w/L_p)$ is the correction to the effective field the plasma feels from the image charges on the trap electrodes (because the image charges are more diffuse near the end of the plasma). The terms with the coefficient $j_{01}/2$ account for the radial component of the force from the confining potentials at either end of the plasma. This equation was shown to be in good agreement with experiments where R_w/R_p , T , and L_p were varied [FINE and DRISCOLL, 1998].

For comparison, a perturbative analysis using fluid equations previously yielded the frequency [FINE, 1988; PRASAD and O'NEIL, 1983]

$$\frac{\omega_1}{\omega_\infty} = 1 + \left(\frac{R_w}{L_p}\right) f_1\left(\frac{R_p}{R_w}\right) \quad (3.59)$$

$$\simeq 1 + \left(\frac{R_w}{L_p}\right) \left[\left(1.30 - 1.08 \frac{R_p}{R_w}\right) \left(\frac{R_w}{R_p} - \frac{R_p}{R_w}\right) \right]. \quad (3.60)$$

for a constant-density plasma with constant length L_p and a short electron mean-free-path ($\nu_{ee} \gg \omega_b$). The function $f_1(R_p/R_w)$ is estimated [FINE, 1988] for the range $0.1 < R_p/R_w < 0.8$ from Fig. 6 of reference [PRASAD and O'NEIL, 1983]. A subsequent Vlasov derivation [PRASAD and O'NEIL, 1984] expanded the drift-kinetic equation and Poisson's equation in terms of Bessel and cosine functions and allowed particles to bounce axially ($\nu_{ee} \leq \omega_b$), producing the same functional form as Eq. (3.60) and a slightly enhanced result for $f_1(R_p/R_w)$. Equation (3.60) predicts larger frequency shifts than those observed in the experiments, where $\nu_{ee} \ll \omega_b$ [FINE and DRISCOLL, 1998].

In addition to finite-length effects, the mode frequency is measured to increase as the mode amplitude becomes a substantial fraction of the wall radius ($D/R_w \lesssim 1$) and the plasma is distorted azimuthally [FINE *et al.*, 1989]. Again considering the response of a plasma in the dynamical equilibrium produces the frequency shift [FINE, 1992]

$$\frac{\omega_{1s}}{\omega_1} = 1 + \left(\frac{D}{R_w}\right)^2 - \frac{1}{2}q_2 \left(\frac{R_p}{R_w}\right)^2 \quad (3.61)$$

where ω_{1s} is the shifted frequency, ω_1 is the unshifted, finite-length frequency, and q_2 is the quadrupole moment of the plasma density perpendicular to the trap axis

$$q_2 \equiv \frac{\int dx dy (y^2 - x^2) n(x, y, z = z_0)}{\int dx dy (y^2 + x^2) n(x, y, z = z_0)}. \quad (3.62)$$

The origin of the coordinate system used to compute q_2 is at the centroid of the density distribution $n(x, y, z = z_0)$, the y axis lies along the major axis of the plasma cross section (ostensibly in the azimuthal direction), and the x axis should be in

the radial direction. The term $(D/R_w)^2$ in Eq. (3.61) comes from a more careful estimate of the effective electric field the displaced plasma experiences from its image charges. The term $-(1/2)q_2(R_p/R_w)^2$ describes the decrease in the effective electric field the plasma experiences due to the plasma's distortion along the inner surface of the grounded trap electrodes (the plasma cross section becomes approximately elliptical, and the image charges on the electrodes can also spread out azimuthally). The relationship $q_2 = 16.7(R_p/R_w)^4(D/R_w)^2$ describes the plasmas in the experiments well [FINE *et al.*, 1989], and Eq. (3.61) is then in good agreement with the measured frequency shift

$$\frac{\omega_{1s}}{\omega_1} = 1 + \left[1 - 7.3 \left(\frac{R_p}{R_w} \right)^6 \right] \left(\frac{D}{R_w} \right)^2 \quad (3.63)$$

The measurements also match the predictions of a fluid theory [PRASAD and MALMBERG, 1986] at small displacements $D/R_w \lesssim 0.1$. The useful result in Eq. (3.61) from the simple dynamical equilibrium model has been explained more carefully and extended to more realistic density profiles using fluid equations [CORNGOLD, 1996].

Equations (3.58) or (3.60) and Eq. (3.61) can be easily combined to make a more complete prediction of the finite-length plasma diocotron mode frequency.

3.4.2 $m = 1$ Diocotron Mode Growth Rate

The $m = 1$ diocotron mode in an infinite-length plasma is not predicted to grow or damp [LEVY, 1968]. For finite-length plasmas, however, there are several effects that contribute to the growth rate of the $m = 1$ diocotron mode.

Even in the absence of trap field imperfections, the $m = 1$ diocotron mode is damped by "rotational pumping" [CLUGGISH and DRISCOLL, 1996; CROOKS and

O'NEIL, 1995; CLUGGISH and DRISCOLL, 1995], where the radial dependence of the confining potentials allow the plasma to expand and drain angular momentum from the mode. The growth rate for $\omega_b \gg \omega_{E \times B}$ is calculated to be [CROOKS and O'NEIL, 1995]

$$\gamma_{\text{rp}} = -\frac{1}{N} C^2 \int d^3r \, 2\nu_T n(r) r^3 \frac{T}{\left[-e \frac{\partial \Phi}{\partial r}\right] L_P^2 R_w^2} \quad (3.64)$$

where C is a numerical constant and Φ is the potential in a frame rotating at the diocotron mode frequency ω_D . In the coordinate system centered on the plasma axis, $\Phi = \phi(r) - \omega_D Br^2/(2c)$, and $\omega_{E \times B} = (c/Br)\partial\Phi/\partial r = \omega_r - \omega_D$. Equation (3.64) may be estimated for a isothermal, constant-density plasma with radius R_p to be

$$\gamma_{\text{rpest}} = -2C^2 \nu_T \left(\frac{\lambda_D^2}{L_P^2} \right) \left(\frac{\left(\frac{R_p}{R_w}\right)^2}{1 - \left(\frac{R_p}{R_w}\right)^2} \right) \quad (3.65)$$

where $C \simeq 2.4$, but good agreement with the data instead requires numerical integration of Eq. (3.64) using realistic density profile data that describes the ends of the plasma well [Eq. (3.65) is consistently a factor of 4–6 too low]. The temperature and magnetic field dependence of this damping is the same as that of the anisotropic temperature equilibration rate ν_T , so the damping is strongly dependent on plasma temperature and only weakly dependent on magnetic field (where $\Omega_c < \bar{v}/b$). For the regime $\omega_{E \times B} \gg \omega_b > \nu_{ee}$, resonant particle interactions are predicted to amplify the growth rate in Eq. (3.64) by the factor

$$\frac{(\gamma_{\text{rp}})_{\text{res}}}{\gamma_{\text{rp}}} = \frac{1}{64} \sqrt{\pi} \frac{\omega_R^6}{2 \omega_b^5 \nu_T} \exp\left(-\frac{\omega_R^2}{8\omega_b^2}\right). \quad (3.66)$$

For small-filament plasmas in EDG, $\omega_{E \times B}/2\pi \sim 0.3$ MHz, $\omega_b/2\pi \sim 1.4$ MHz, $\nu_T \sim 300$ Hz, and $5 \times \gamma_{\text{rpest}} \sim -0.7$ /s.

Rotational pumping can be understood by considering the motion of an individual flux tube in the plasma [CROOKS and O'NEIL, 1995]. Since the plasma may

be described as a largely unperturbed, off-axis, dynamic equilibrium in the presence of the $m = 1$ mode, it continues to rotate around its axis of symmetry at the rotation frequency ω_r . As the displaced plasma rotates around its axis, any particular flux tube in the plasma will experience confining voltages that vary as it moves towards and away from the trap axis (between its own particular “perihelion” and “aphelion”, if its distance from the plasma axis is greater than D). The flux tube oscillates in length as a result, and its parallel temperature along the field line also oscillates. Electron-electron collisions attempt to equilibrate the perpendicular temperature with the changing parallel temperature, and, on average, the flux tube is heated, draining electrostatic energy and causing the plasma to expand. This expansion also requires angular momentum, which is only available from the mode, so the mode damps. The total canonical angular momentum in the presence of a diocotron mode for a rotationally symmetric plasma is simply [CROOKS and O’NEIL, 1995]

$$L \simeq \frac{-eB}{2c} N \left[\langle r^2 \rangle + D^2 \right], \quad (3.67)$$

[compared with Eq. (3.4)], which may be determined from the vector form of Eq. (3.2) with the identification $\mathbf{r}_j \rightarrow \mathbf{r}_j + \mathbf{D}$.

Finite resistance in any of the trap electrodes (especially the zero-Volt electrodes next to the plasma) can allow imperfections in the trap fields that cause the mode to grow. This “resistive wall” effect is readily observed [CHAO *et al.*, 2000], and may be used to strongly excite the $m = 1$ mode. For a resistance R and capacitance C in parallel between the point of zero potential (machine ground) and an electrode segment $\Delta\phi$ wide (azimuthally) and L_s long (see Fig. 2.28), the $m = 1$ diocotron

mode growth rate is predicted to be [WHITE *et al.*, 1982]

$$\gamma_R = \frac{1}{\pi^2} \frac{L_s^2}{L_p} \omega_{1s}^2 \left(\sin^2 \frac{\Delta\phi}{2} \right) \left(\frac{R}{1 + (\omega_{1s}RC)^2} \right), \quad (3.68)$$

where L_p is the plasma length and ω_{1s} is the mode frequency. The electrode segment impedance allows small voltages to exist on the segment as the plasma passes by, since the plasma induces currents to it from machine ground Equation (3.68) is derived by setting the change of the plasma potential energy to the power dissipated by the impedance, using the image charge current expression in Eq. (2.21). Note that this is appropriate because the $m = 1$ mode is a negative-energy mode, meaning that it is energetically favorable for the plasma if the mode's amplitude increases (since the trap electrodes surrounding the plasma are at a potential of zero Volts). The minimum resistive wall growth for the EDG plasma is caused by the input impedance of the diocotron mode diagnostic amplifiers, and this impedance has been chosen to minimize any excitation of the mode; in EDG, $(\gamma_R)_{\min} \simeq 5.6 \times 10^{-4} \text{ s}^{-1}$ for $R = 100 \text{ M}\Omega$, $C = 2.6 \text{ nF}$, and $\omega_D = 200 \text{ kHz}$.

A small number of ions in the trap can also cause the $m = 1$ diocotron mode to grow. For ions that are completely trapped in the plasma's potential well (e.g., in an infinite-length plasma), this phenomenon is called the ion resonance instability [DAVIDSON, 1990; LEVY *et al.*, 1969; DAVIDSON and UHM, 1977, 1978]. In this case, the ions rotate in the trap at a different rotation frequency than the electrons, causing an azimuthal two-stream instability that grows exponentially. Ions in a finite-length trap generally escape the plasma axially, even if only to be trapped in one of the confining potential wells. Studies of these "transient" ions generated by ionization of the background gas by warm ($T \gtrsim 4 \text{ eV}$) plasmas showed that the diocotron mode grew linearly with time, at a rate that was linearly dependent on the number of ions escaping the plasma [PEURRUNG *et al.*, 1993]. Rather than

a sharp resonance between the diocotron mode frequency and the oscillation frequency of the ions in the plasma as predicted before [LEVY *et al.*, 1969], a broad resonance was seen, and is much better explained by a theory allowing continual axial loss of the generated ions [FAJANS, 1993].

The presence of accumulated “transiting” ions passing through an electron plasma axially has recently been observed to cause substantial growth of $m = 1, 2$, and 3 diocotron modes [KABANTSEV and DRISCOLL, 2003b]. This mechanism is quite similar to the “transient ion” resonance instability observed by Peurrung [PEURRUNG *et al.*, 1993], but is enhanced by the ability of the UCSD trap to store the ions introduced [KABANTSEV and DRISCOLL, 2003b]. The transiting ions in these experiments were created by ionization of the background gas either near the electron source or in the bulk of the plasma, and were trapped between the positively charged electron source grid and a positively charged density diagnostic on the far end of the trap (such as a phosphor screen density diagnostic) where they would accumulate. The mode was observed to grow exponentially due to the accumulation of the transiting ions, but its growth rate dropped immediately by a factor of 10 when the accumulated ions were released from the trap and only transient ions remained. The growth rates measured were linearly proportional to the ion accumulation rate in the trap ($\gamma_m \propto \kappa_m \nu_+$), with constants of proportionality κ_m much greater than 1 ($\kappa_1 \sim 400$). In EDG, the electron temperature is low enough that no ions should be created by the plasma electrons, and any transiting ions would flow into the trap from the area of the filament. There is no quantified mechanism at present that describes the generation of ions near the filament assembly, however.

Finally, the direct influence of background gas on the plasma is predicted to cause exponential growth of the $m = 1$ mode at the growth rate [DAVIDSON and CHAO, 1996b,a]

$$\gamma_n = \frac{\nu_{en}}{\Omega_c} \omega_{1s} \quad (3.69)$$

for elastic collisions between the plasma electrons and gas molecules, where ω_{1s} represents the real $m = 1$ mode frequency. The fluid theory used for this estimate only describes mode growth that is quick enough that the plasma density profile changes very little during the mode evolution. The computed growth rate $\gamma_n \sim 3 \times 10^{-6} \text{ s}^{-1}$ for EDG plasmas at $P = 1 \times 10^{-10} \text{ Torr}$ is much smaller than the minimum normalized expansion rate $\nu_p \equiv (1/\langle r^2 \rangle) d\langle r^2 \rangle/dt \sim .05 \text{ s}^{-1}$ due to asymmetry-induced expansion, so this effect is not measurable in EDG.

In addition to these known mechanisms for mode growth and damping, an unexplained exponential damping was observed previously on the EDG device [CHAO *et al.*, 1999c] that appeared to vary as $\gamma_{\text{unex}} \propto (N_L/B)^2 \propto \omega_D^2$. By choosing appropriate values of the line density and magnetic field, this $(N_L/B)^2$ damping can be minimized for EDG experiments. Note that this $(N_L/B)^2$ scaling disagrees completely with the scaling of rotational pumping, which is very insensitive to density and magnetic field, but agrees with the scaling of certain types of asymmetry-induced expansion. Also, the estimated characteristic density relaxation rates from Eqs. (3.21) and (3.24) show that the density profile relaxation scales roughly as $(n/B)^2$,

$$\begin{aligned} \frac{1}{\tau_n^{E \times B}} &\propto \left(\frac{n}{B}\right)^2 \ln\left(\frac{n^{3/2} b^4 m_e c \bar{v}}{B e} (\lambda_D \sqrt{n})\right) \\ \frac{1}{\tau_n^{\text{class}}} &\propto \left(\frac{n}{B}\right)^2 \ln\left(\frac{1}{B} \frac{m_e c \bar{v}}{e b}\right), \end{aligned} \quad (3.70)$$

leaving open the possibility that the plasma relaxation to thermal quasi-equilibrium is somehow coupled to the mode evolution.

The measured growth rates for the $(N_L/B)^2$ damping were also compared with a prediction based on coupling between the $m = 1$ mode and Landau-damped, $k_z \neq 0$ modes (Trivelpiece-Gould modes) [PRASAD and O'NEIL, 1984], which was given by

$$\gamma_{\text{mc}} = -(0.4) \frac{2\lambda_d (\omega_r - \omega_\infty)^2}{L_p \omega_p} \ln \left(\frac{\omega_p}{(\omega_r - \omega_\infty)^2} \right) \quad (3.71)$$

for a constant-density plasma with flat ends, $\omega_p \ll \omega_c$, and $R_p \ll L_p$. Equation 3.71 has a similar scaling with N_L and B [$\gamma_{\text{mc}} \propto (N_L/B)^2 \ln(B/N_L)$, since $\omega_\infty = \omega_r (R_p/L_p)^2$ for a constant-density plasma], but is only applicable in the limit where $1 \gg (m\omega_r - \omega_D)/\omega_p \gg (\lambda_D/L_p)$, which isn't satisfied by EDG parameters: $((m\omega_r - \omega_D)/\omega_p \approx 8 \times 10^{-3}) \not\gg ((\lambda_D/L_p) \approx 1.4 \times 10^{-2})$. The growth rate predicted with this formula for typical small-filament plasma parameters is $\gamma_{\text{mc}} \approx -110$ /s, which is much larger than any of the growth rates observed in EDG. Equation 3.71 was also clearly argued to be and shown to be a poor prediction of the plasma growth rate in the similar EV device at UCSD [FINE, 1988].

3.5 Summary of Theoretical Predictions

In this chapter, several current descriptions of the behavior of plasmas in Malmberg-Penning traps were reviewed. The relatively good confinement of particles in these traps is understood as the manifestation of powerful conservation constraints on the particle motion, and only imperfections in the trap fields or vacuum can allow particles to eventually escape from the trap radially. When the

torques from these imperfections are small enough, the plasma is predicted to relax to a thermal quasi-equilibrium profile with a uniform electron temperature, and the radial density profile and several other quasi-equilibrium quantities have been derived to describe the plasma's evolution in this state. The mechanisms in the plasma that help it relax to this quasi-equilibrium state from any initial state have also been described, and new effects in cross-field particle and energy transport have been discovered in these traps that add to our general knowledge of plasma behavior. The dynamics of a particularly well studied electrostatic wave, the $m = 1$ diocotron mode, have also been presented. This collection of theoretical efforts provides many useful tools for describing the phenomena observed in the EDG device.

Chapter 4

Measurements of Plasma Expansion and Temperature Evolution

The EDG experimental device was originally constructed in order to determine whether measurements of electron plasma expansion at low background gas pressures could be quantitatively predicted as a function of the background gas pressure, and this model system used as a standard for pressure measurement. According to the predictions in sections [3.2](#) and [3.3.2](#), elastic collisions between the EDG plasma electrons and the background gas molecules should cause the plasma to expand, with the liberated electrostatic potential energy converted to particle kinetic energy. In this chapter, we will describe measurements of the plasma expansion (section [4.2](#)) and the accompanying changes in the plasma temperature (section [4.3](#)).

4.1 Expansion Rate Determination

To determine the expansion rate for an EDG plasma, radial density profiles (such as those in Fig. 4.1) are recorded at different points in the plasma evolution, the mean-square radius of each profile is calculated, and the slope of the mean-square radius data versus time is considered to be the expansion rate. In most cases, we fit some subset of the mean-square radius data with a line to obtain the slope. This approach is reasonable if the change in temperature (and therefore the collision frequency) is negligible for the data subset we are fitting, because these are the only two time-varying quantities in the predicted expansion rate [Eq. (3.46)].

The plasma's mean-square radius is estimated from a measured, axially integrated density profile $Q(r)$ according to

$$\langle r^2 \rangle = \frac{\int_0^{R_w} dr 2\pi r (r^2) Q(r)}{\int_0^{R_w} dr 2\pi r Q(r)}, \quad (4.1)$$

where the total number of electrons in the trap $N = \int_0^{R_w} 2\pi r dr Q(r)$, and the integrals are evaluated numerically using the five-point, Newton-Cotes algorithm included in the programming language IDL (version 5.3, routine `int_tabulated`). For a density diagnostic with infinite radial resolution, the axially integrated density profile would simply be $Q(r) = \int dz n(r, \phi_0, z)$. For the Faraday-cup density diagnostic, $Q(r)$ may be related to the true electron density $n(r', \phi, z)$ by

$$Q_F(r) = -\frac{e}{A_h} \int_0^L dz \int_{A_h} dr' d\phi n(r', \phi, z), \quad (4.2)$$

where A_h is the area of the collimating hole, L is the trap length, and $n(r', \phi, z)$ is the three-dimensional number density of the plasma electrons. For the phosphor

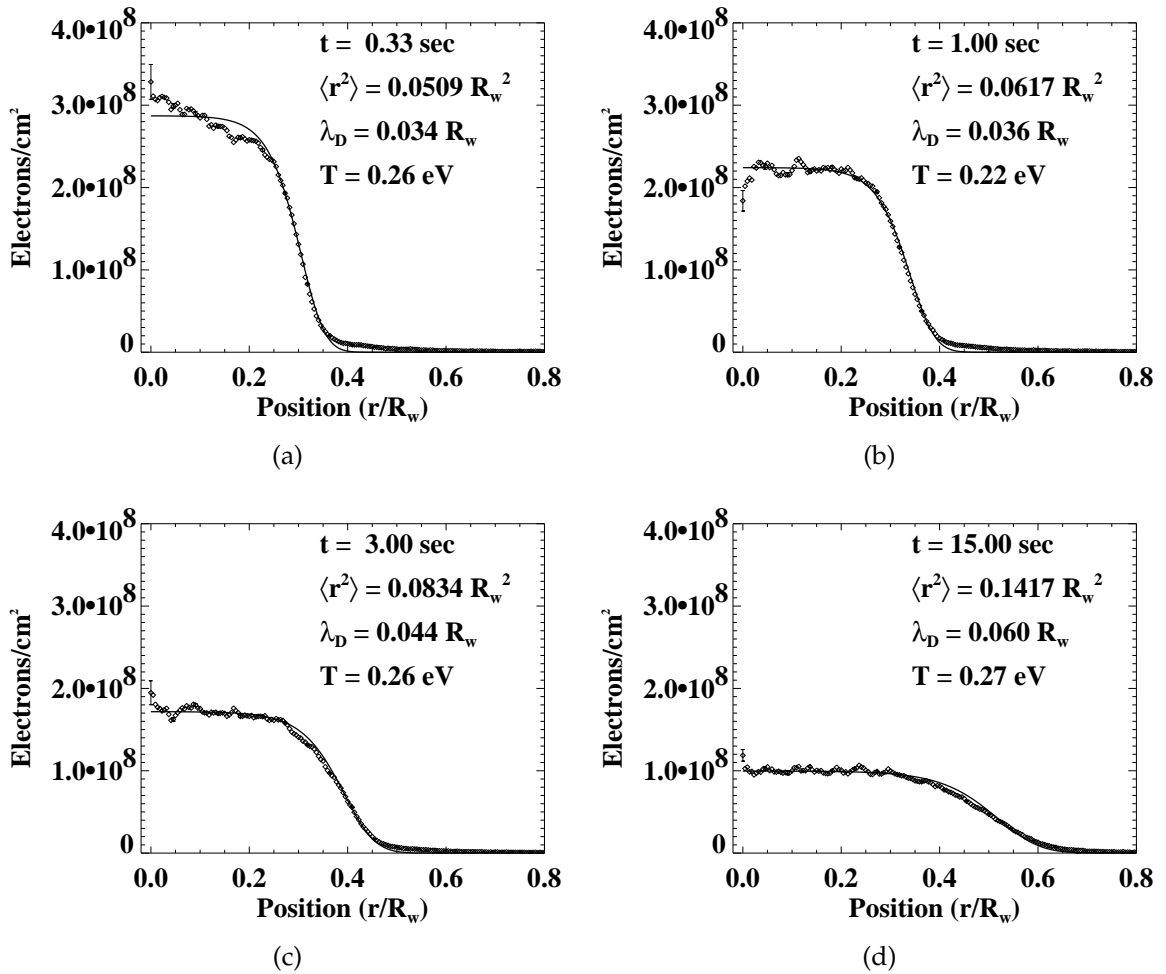


Figure 4.1: Evolution of density profiles in EDG at $P \sim 6 \times 10^{-9}$ Torr. The solid lines are the fitted, thermal quasi-equilibrium profiles predicted with the fluid theory.

screen density diagnostic, $Q(r)$ is approximately

$$Q_P(r) = -\frac{e}{2\pi r \delta r} \int_0^{2\pi} \int_r^{r+\delta r} r' dr' d\phi \int_0^L dz n(r', \phi, z), \quad (4.3)$$

where $A_p = \delta r^2$ is the approximate area of the screen that one CCD camera pixel sees. The axially integrated density profile from the phosphor screen diagnostic is actually determined by taking the medians of the image data in azimuthal rings of radial width δr , as described in section 2.2.2, and is better expressed as

$$Q_P(r) = -\frac{e}{(\delta r)^2} \left\{ \text{Median} \left[\int_0^L dz \int_{A_p(r')} dr'' d\phi n(r'', \phi, z) \right] \middle| r \leq r' < r + \delta r \right\}. \quad (4.4)$$

The uncertainty in the experimentally determined mean-square radius for a given density profile is estimated from the standard errors of the mean for $Q(r)$, $\sigma_{\bar{Q}}(r_i)$, at each radial location r_i in the profile, and is used to determine the uncertainty in the computed expansion rate. Specifically, the mean-square-radius uncertainty is approximated by calculating the uncertainty of this less-sophisticated computation of the mean-square radius:

$$\langle r^2 \rangle = \frac{\sum_i (2\pi r_i \delta r) r_i^2 Q(r_i)}{\sum_i (2\pi r_i \delta r) Q(r_i)}. \quad (4.5)$$

The result is [CHAO, 1999]

$$\begin{aligned} \sigma_{\langle r^2 \rangle}^2 &= \frac{1}{N_{\text{sum}}} \sum_i \left(2\pi r_i \delta r r_i^2 \sigma_{\bar{Q}(r_i)} \right)^2 \\ &= \frac{(2\pi \delta r)^2}{N_{\text{sum}}} \sum_i r_i^6 \sigma_{\bar{Q}(r_i)}^2 \end{aligned} \quad (4.6)$$

where $\sigma_{\bar{Q}(r_i)} = \sigma_{Q(r_i)} / \sqrt{m_i}$ is the uncertainty of the mean density measurement at $r = r_i$, m_i is the number of density measurements at $r = r_i$, and $N_{\text{sum}} =$

$\sum_i (2\pi r_i \delta r) Q(r_i)$ is the denominator of Eq. (4.5). The uncertainty in the numerically integrated value $N \equiv \int_0^{R_w} 2\pi r dr Q(r) \approx N_{\text{sum}}$ is often neglected in the computation of $\sigma_{\langle r^2 \rangle}$, as it is usually at least a factor of two smaller than the contributions from $\sigma_{\overline{Q}(r_i)}$.

The uncertainty in the plasma expansion rate is determined by the algorithms used to fit the mean-square-radius evolution, and is calculated automatically by the fitting routines in the programming environment IDL. The routine `linfit` included in IDL 5.3 was used primarily, and it was made from the routines `fit.c`, `gammq.c`, `gser.c`, and `gcf.c` from section 15.2 of “Numerical Recipes in C” [PRESS *et al.*, 1992]. The `curvefit` routine in IDL 5.3 was also used, and is an implementation of the function `curfit` [BEVINGTON and ROBINSON, 1992] which uses a modified Marquardt algorithm [MARQUARDT, 1963].

It is important to note that the $Q(r)$ used for the mean-square radius determinations are ignored past a chosen plasma-edge radius R_{edge} ; specifically, $Q(r > R_{\text{edge}}) \equiv 0$. This is necessary because small errors in the profile due to detector noise can contribute considerably at higher radii to the $\langle r^2 \rangle$ computation, as they are amplified by the factor r^3 in the numerical integral in Eq. (4.1) (see Figures 4.2 and 4.3). For profiles taken with the Faraday-cup density diagnostic, R_{edge} is defined as the last radial point in the profile before the measured $Q(r)$ is negative (due to the noise). For profiles taken with the phosphor screen density diagnostic, R_{edge} is taken to be the first radial point where the profile data drops within one standard deviation of zero [see Fig. 4.2], although for some of the phosphor-screen data presented in this thesis R_{edge} was defined as a weighted average between the point where $Q(r)$ is 5% of the peak value $\max(Q(r))$ (weighted by 4/5) and the radial point where the digitized profile data values stop changing with increasing

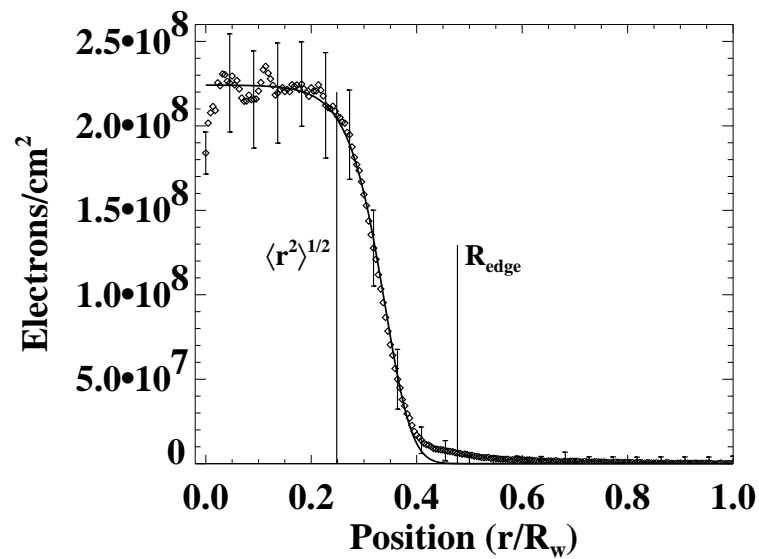


Figure 4.2: This is the density profile from Fig. 4.1(b), except with error bars representing the standard deviation of the points at a particular radius rather than the standard deviation of the mean of the points. The solid line is again the fitted thermal quasi-equilibrium profile predicted with the fluid theory. The root-mean-square radius and edge radius are marked in the plot, and the two different edge radius definitions described in the text coincide for this density profile.

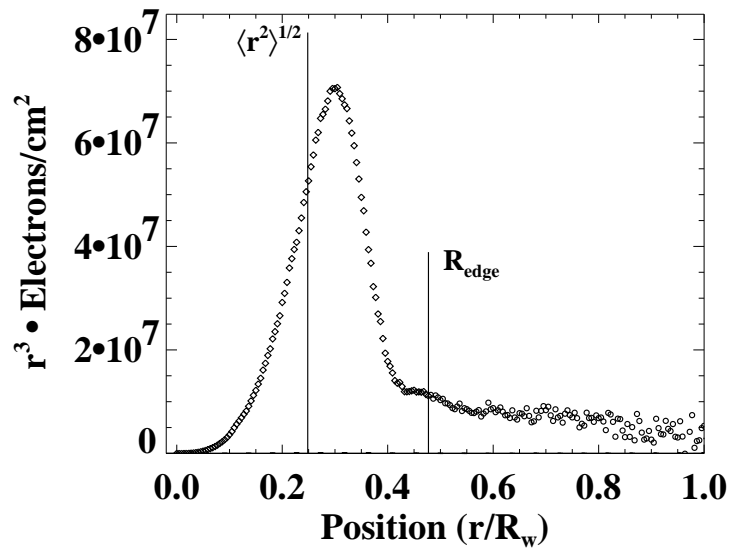


Figure 4.3: Displayed here is the product of the profile in Fig. 4.2 and r^3 , where the circles represent the data that is ignored in the mean-square-radius calculation. The root-mean-square radius and edge radius are again noted, and the two different edge radius definitions described in the text coincide for this density profile. Including the data beyond R_{edge} in the calculations (and keeping the same density normalization) would increase the apparent total charge by only 3.7% but increase the calculated mean-square radius by 15%.

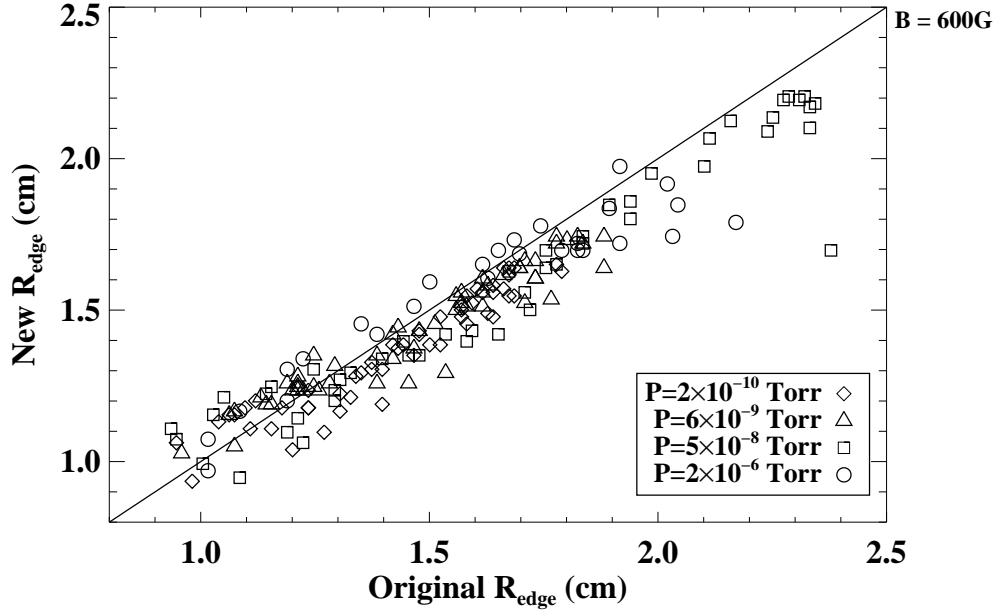


Figure 4.4: Comparison of R_{edge} computations. The “new” R_{edge} is defined as the first radial point where the profile data drops within one standard deviation of zero, and the “old” R_{edge} is close to the point where the profile drops to 5% of the peak profile value $\max(Q(r))$. The solid line is the line (“new” R_{edge}) = (“old” R_{edge}).

radius (weighted by $1/5$). This latter, complicated definition for the phosphor-screen data’s R_{edge} was developed because of the unexplained long tails in the density distribution [e.g., see Figures 4.2, 4.1(a), and 4.1(b)]. These tails may be due to unaccounted-for background light reflecting off the phosphor screen, an unidentified imperfection in the profile determination from the raw image data, a focusing problem with the camera optics, or unexpected scattering in the phosphor itself. The two definitions for the phosphor-screen data’s R_{edge} usually result in similar values, as illustrated in Fig. 4.4.

In nearly all of the calculations in this thesis of quantities derived from radial electron density profiles, the measured, axially integrated electron density profiles

were used directly. The axially integrated electron density profile is not the same as the true radial density profile because the radially dependent confining potentials cause the plasma's ends to be curved [$L_p = L_p(r)$]. A better estimate of the true radial density profile (that exists far from the trap's confining electrodes or in an infinite-length electron plasma) can be obtained for plasmas in thermal quasi-equilibrium by solving Poisson's equation [Eq. (3.28)] numerically in the region inside the trap electrodes [CHAO, 1999; CHAO *et al.*, 1999a]. This is accomplished iteratively by alternately assigning a Boltzmann distribution to the plasma electrons [$n(r, z) \propto \exp\{e\phi(r, z)/T\}$, with constant temperature T] to obtain an estimate for $n(r, z)$, and solving Poisson's equation to obtain the corresponding $\phi(r, z)$. Each new solution of $\phi(r, z)$ is used to make a better estimate for $n(r, z)$, and eventually the plasma and vacuum fields relax into an equilibrium. Programs incorporating this algorithm have been used by several experimental groups (including EDG) to make better radial density profile estimates, but the axially integrated profiles have been used here instead for several reasons: (1) The inferred temperature and mean-square-radius values calculated using the measured, axially integrated, radial density profiles do not differ significantly from those calculated using the better radial density profile estimates (this is determined for large-filament plasmas); (2) the "Poisson solver" code that performs the density profile estimation is computationally intensive; (3) the "Poisson solver" code does not always converge on a numerical solution, and has an especially difficult time converging when noise in the measurements makes $Q(r)$ non-monotonically-decreasing (which is the case for the high-resolution phosphor-screen data); (4) not all the plasmas measured are in thermal quasi-equilibrium; and (5) the temperature inferences necessary to make the self-consistent density profile estimates have not been unequivocally

demonstrated to be representative of the true plasma temperature, even for plasmas in thermal quasi-equilibrium.

The overall effect of not accounting for the curved ends of the plasma is that the axially integrated density profiles are enhanced over the true radial density profiles near the trap axis. This should cause the inferred temperatures to be artificially low, the calculated mean-square radii to be artificially low, and, since the relative discrepancy becomes greater as the plasma expands, the determined expansion rates to be artificially low. These discrepancies will also be smaller for the small-filament data, generally, because plasmas formed with the smaller filament interact with an effectively more uniform confining field than the larger plasmas do.

Lastly, there is also a radially varying background for the axially integrated density profiles that can be obtained by performing the image profile calculation on an image with no plasma. While this apparently computational artifact is uncharacterized, its maximum amplitude is not a substantial fraction of the signal at the plasma center. This background is thought to be related to the unexplained long tails in the density profiles.

4.2 Expansion Rate Scaling with Pressure

4.2.1 Review of the Previous Data

The expansion of electron plasmas due to background gas was first explored with measurements of the density evolution at $r = 0$ [MALMBERG and DRISCOLL, 1980; DEGRASSIE and MALMBERG, 1980]. The characteristic quantities $\tau_{n0/2}$, the time for the density at $r = 0$ to decrease to half of its initial value; $\tau_{N/2}$, the time for the plasma to lose half of its electrons radially to the trap electrodes; and τ_n , the

rate of increase of the inverse central density $\tau_n = (d/dt)[1/n(r = 0, t)]$, were all observed to vary approximately as B^2/P at higher pressures, in agreement with the simple scaling from the Boltzmann equation predicted in Eq. (3.53). At pressures below $P = 10^7$ Torr, the quantities $\tau_{n_{0/2}}$ and $\tau_{N/2}$ were observed to be independent of pressure, and the plasma's minimum level of expansion was later demonstrated to be due to imperfections in the trap construction (asymmetry-induced expansion), as described in section 3.3.1. For the measurements of $\tau_{N/2}$ and τ_n , the plasmas extended radially to the trap electrodes, and presumably had some uncharacterized interaction with them.

Initial measurements of the plasma's expansion rate as a function of pressure in EDG [CHAO *et al.*, 2000; CHAO, 1999; CHAO *et al.*, 1999b] suggested that the plasma expands at a rate more than four times faster than that predicted by the uniform-temperature plasma expansion rate [Eq. (3.46)]

$$\frac{d}{dt}\langle r^2 \rangle = \frac{2N_L e^2}{m_e} \frac{\nu_{en}(t)}{\Omega_c^2 - \nu_{en}^2(t)} \left(1 + \frac{2T(t)}{N_L e^2} \right). \quad (4.7)$$

This data, in the range 10^{-8} Torr $< P < 10^{-6}$ Torr in Fig. 4.5, was an improvement over the earlier, $r = 0$ density evolution data because the EDG plasmas were clearly not in contact with the trap electrodes and the expansion rate was computed directly from radial density profiles rather than assumed to be proportional to $\tau_{n_{0/2}}$ or $\tau_{N/2}$. In addition, the measurement of density profiles provided information on the electrostatic potential energy evolution, the evolution of the density profile shape (giving an indication of how close the plasma state is to a thermal quasi-equilibrium state), and the effective, inferred temperature evolution from fitting predicted thermal quasi-equilibrium density profiles to the data. At the lowest pressures ($P \lesssim 1 \times 10^{-8}$ Torr), the measured expansion rates in EDG clearly disagreed with the theoretical prediction, and this threshold level of expansion

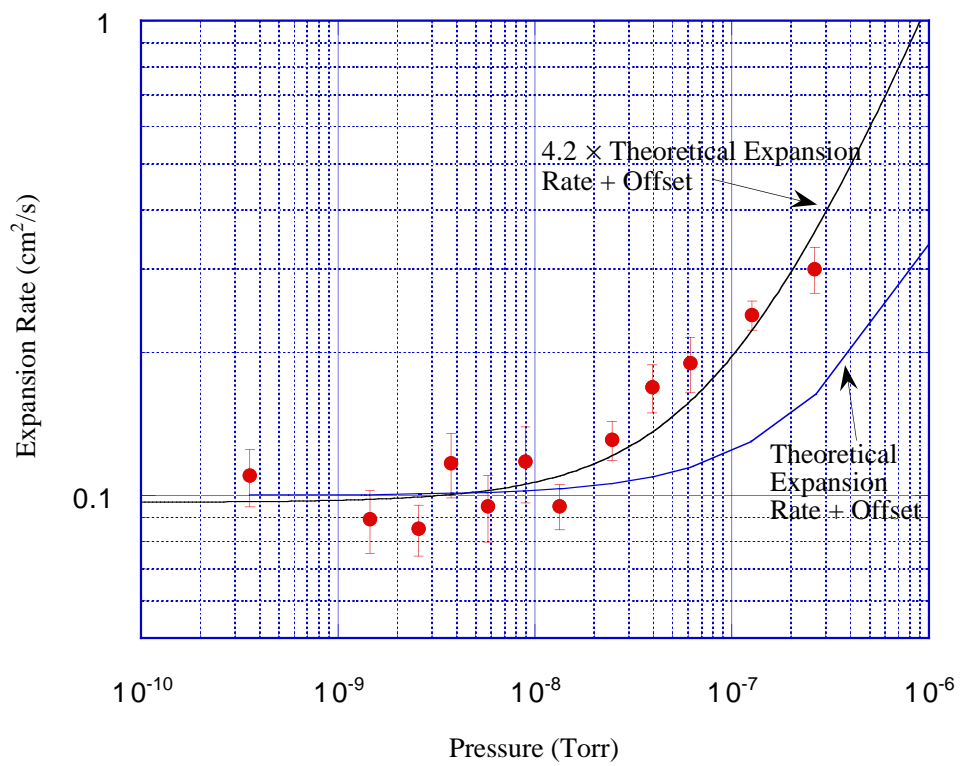


Figure 4.5: Plasma expansion rate as a function of pressure. For this data, $B = 610$ G and $N_L = 3.4 \times 10^7$ electrons/cm. (Reproduced from [CHAO, 1999], with permission.)

was suspected to be the asymmetry-induced expansion observed before. Since asymmetry-induced expansion has at most a weak dependence on pressure, it is accounted for by adding an arbitrary offset to the theoretical linear dependence in Eq. (3.46). This data shows that it is very difficult to unambiguously determine the gas pressure in EDG below $P \lesssim 1 \times 10^{-8}$ Torr using a Faraday-cup density diagnostic with similar sensitivity.

4.2.2 Large-Filament Data

A natural question evoked by the pressure dependence in Fig. 4.5 is whether the plasma continues to expand more quickly than predicted at higher background gas pressures. This question is somewhat academic, since $\nu_{en} > \nu_{ee}$ above $P \approx 1.2 \times 10^7$ Torr (see section 3.3.2) and the uniform-temperature expansion rate formula in Eq. (3.46) is no longer necessarily applicable. Equation (3.46) reduces to the simple Boltzmann equation scaling in Eq. (3.53) for $T = 0$, however, so the measurement should still give us insight into whether a factor of four is missing from the theoretical prediction. Furthermore, the different dynamics in a parameter range where temperature gradients could exist are worthy of study.

The expansion rate data set in Fig. 4.5 was therefore extended to higher pressures [MORRISON *et al.*, 2001, 2002], and the results are presented in Fig. 4.6. In this figure, the data denoted by circles and squares corresponds to the low-pressure data set used for Fig. 4.5, the data denoted by diamonds and triangles is the new data, and the dash-dot curve is the theoretical prediction + offset. The data represented by diamonds is determined by fitting the mean-square radius evolution data taken before the point in the evolution where the measured total number of plasma electrons had decreased by 2%, and the data represented by diamonds is

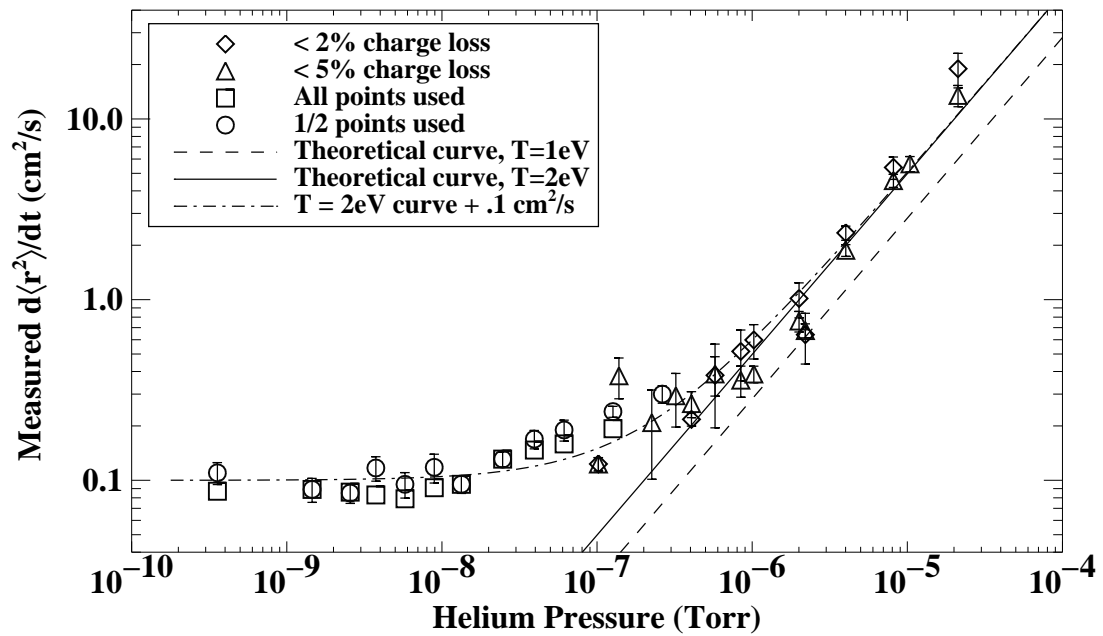


Figure 4.6: Plasma expansion rates vs. pressure at $B = 610 \text{ G}$ for 2.8×10^7 electrons/cm $< N_L < 3.4 \times 10^7$ electrons/cm. The dash-dot theoretical curve uses $T = 2 \text{ eV}$, $N_L = 3.41 \times 10^7$ electrons/cm, and an offset of $0.1 \text{ cm}^2/\text{sec}$.

determined by fitting the mean-square radius evolution data taken before the measured total number of electrons had decreased by 5%. The similar expansion rates estimated from these different subsets of the same mean-square radius evolution illustrate that the changes in the expansion rate during the plasma evolution (described below and displayed in Fig. 4.7) are not dramatic enough to obscure the linear dependence of the expansion rate on helium gas pressure. The differences between the expansion rates estimated for different subsets of the evolution give an indication of the uncertainty in the calculated expansion rates under these trap conditions.

The new data in Fig. 4.6 is more consistent with the theoretical prediction for $T = 2$ eV than for a $T = 1$ eV theoretical curve with an additional factor of four, suggesting that the previous data simply did not extend to a high-enough pressure (where asymmetry-induced expansion was sufficiently small compared to the electron-neutral-collision-dominated plasma expansion) to see the correct pressure dependence. The absolute pressure reported is measured with ionization gauges and is therefore only known to be within a factor of two of the true pressure, so it is possible the measured expansion rates could actually be consistent with either the prediction for $T = 1$ eV plasmas or $T = 4$ plasmas. The plasma temperature is the only quantity in the uniform-temperature expansion rate formula that isn't directly measured in this data set, and though the plasma temperatures inferred from the higher-pressure density profiles varied in the range $0.2 \text{ eV} < T < 4 \text{ eV}$ they were generally close to $T = 2$ eV. If the temperature was definitively known to be $T = 2$ eV, the plotted theoretical curve would be an absolute prediction from the fluid theory.

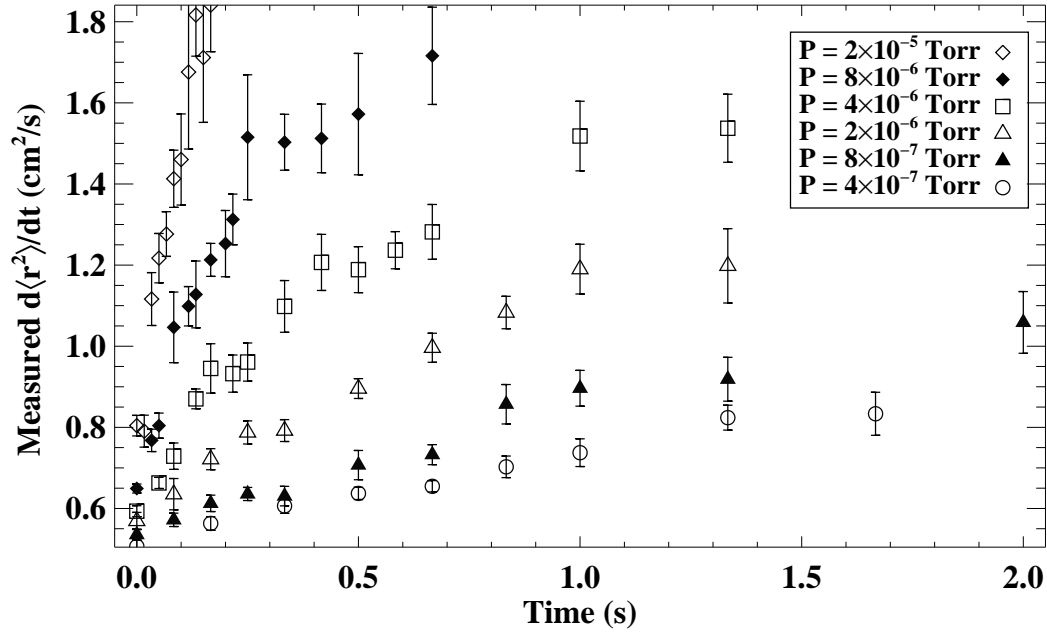


Figure 4.7: Mean-square radius vs. time for $t < 2$ seconds. This data is for the new expansion rate points in Fig. 4.6.

The mean-square radius data used to estimate the expansion rates in Fig. 4.6 was taken in the first 4.5 seconds of plasma evolution, and there is a noticeable decrease in the expansion rate towards the end of the evolutions. This is shown in Fig. 4.7 for the new expansion rate data, which only extended to $t = 2$ seconds. At the higher pressures, this phenomenon was suspected to be due to difficulties in observing diffuse profiles because of diagnostic noise and to interference with the plasma expansion by the trap electrodes. The latter difficulty is indicated because the total plasma charge measured with the total collector decreased during the mean-square radius evolution, as shown in Fig. 4.8. This effect was more pronounced as the background pressure was increased. At the lower pressures, the

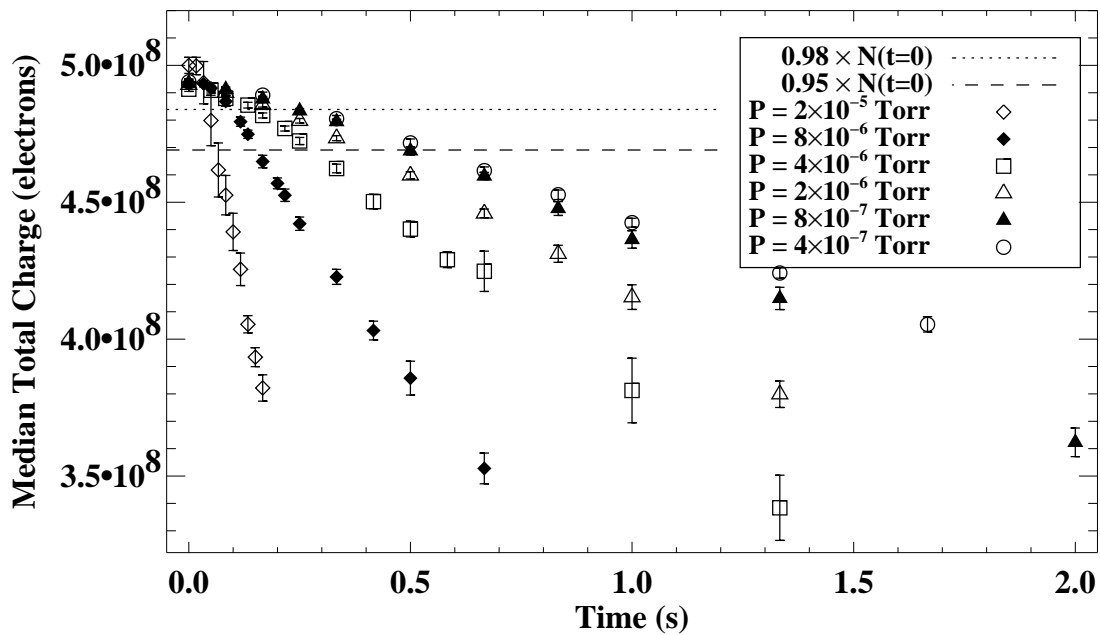


Figure 4.8: Median total charge vs. time for $t < 2$ seconds. This data is for the new expansion rate points in Fig. 4.6. The error bars are the standard deviation of the total charge data taken for the density profile at each point in time. The lines denoting the level of 98% and 95% charge loss are computed using the $t = 0$ median total charge for $P = 8 \times 10^{-6}$ Torr.

decrease in the expansion rate was thought to indicate that the plasma temperature was slowly decreasing with time. The expansion rates displayed in Fig. 4.6 were determined for early subsets of the mean-square-radius evolution in order to cope with these details. Specifically, the diamonds are calculated using the mean-square-radius data points measured before the total plasma charge drops by 2%; the triangles are calculated using the data points measured before the total plasma charge drops by 5%; the circles are calculated using the data taken in approximately the first 2.25 seconds of evolution; and the squares are calculated using the entire, 4.5-second mean-square radius evolution.

The plasma expansion was also measured at $B = 300$ G for comparison [MORRISON *et al.*, 2001, 2002], and this data is presented in Fig. 4.9. In this data set, the expansion rate points agree well with the theoretical prediction using $T = 1$ eV and an offset of $0.5 \text{ cm}^2/\text{sec}$. The diamonds and triangles are calculated in the same manner as for the $B = 610$ G data, and the squares are obtained by manually choosing the number of mean-square radius values to fit such that only points with a relatively small calculated uncertainty are included. (Specifically, $\sigma_{\langle r^2 \rangle}$ is noticeably smaller for the included points than for the excluded points.) The error bars in the plot are determined using the mean-square-radius measurement uncertainties $\sigma_{\langle r^2 \rangle}$, but, again, the differences between the different estimates for the same evolution are also important indications of the precision of the expansion rate measurement.

In contrast with the $B = 610$ G data, the temperatures inferred from the axially integrated density profiles above $P = 10^{-6}$ Torr in the $B = 300$ G data increased quickly from $T \approx 1$ eV to $T \approx 4$ eV during the evolution. This increase was even greater for the temperatures inferred using estimated radial density profiles from

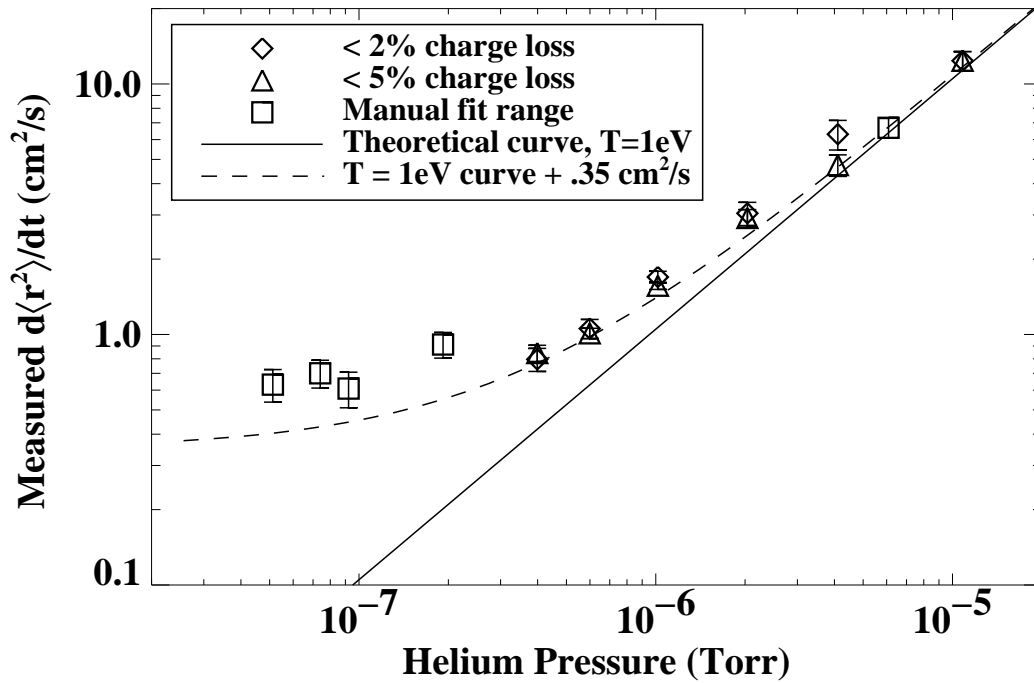


Figure 4.9: Plasma expansion rates vs. pressure at $B = 300 \text{ G}$ and $N_L \approx 2.6 \times 10^7$ electrons/cm. The theoretical prediction uses $T = 1 \text{ eV}$ and an offset of $0.5 \text{ cm}^2/\text{sec}$.

the “Poisson solver” code. Accordingly, it is not clear why the expansion rates obtained from these profiles should agree with the $T = 1$ eV theoretical prediction. One possible explanation could be that interaction with the trap electrodes was changing the density profile without affecting the plasma temperature, and such an effect could only be diagnosed with a direct temperature measurement.

4.2.3 Small-Filament Data

To allay concerns that the slower expansion towards the end of the one-second mean-square-radius evolutions and the dramatic inferred temperature increases for the $B = 300$ G data were due to interference by the trap electrodes, the “large”, 0.5-inch-radius filament was replaced with a smaller, 0.25-inch-radius filament. The plasmas created with the smaller filament take more time to expand to a given size than larger plasmas do, and have very similar values of total plasma charge since both filaments can handle similar amounts of heating current and voltage.

The dependence of the plasma expansion rate on background gas pressure was measured for smaller plasmas in the same manner as for the large-filament plasmas, and the results are displayed in Figures 4.10 and 4.11. In Fig. 4.10, the data appears largely consistent with the $T = 1$ eV theoretical curve (using the same offset as the previous, $B = 610$ G data set), again supporting the prediction in Eq. (3.46). The individual mean-square radius evolutions for the small-filament data have the same decrease in the expansion seen at the end of the large-filament plasma evolutions, though, suggesting that interactions with the trap electrodes are having a negligible impact on the density profile evolution in both cases.

The clearest discrepancy between the $B = 600$ G, small-filament data and the $B = 610$ G, large-filament data is that the smaller-filament expansion rates above

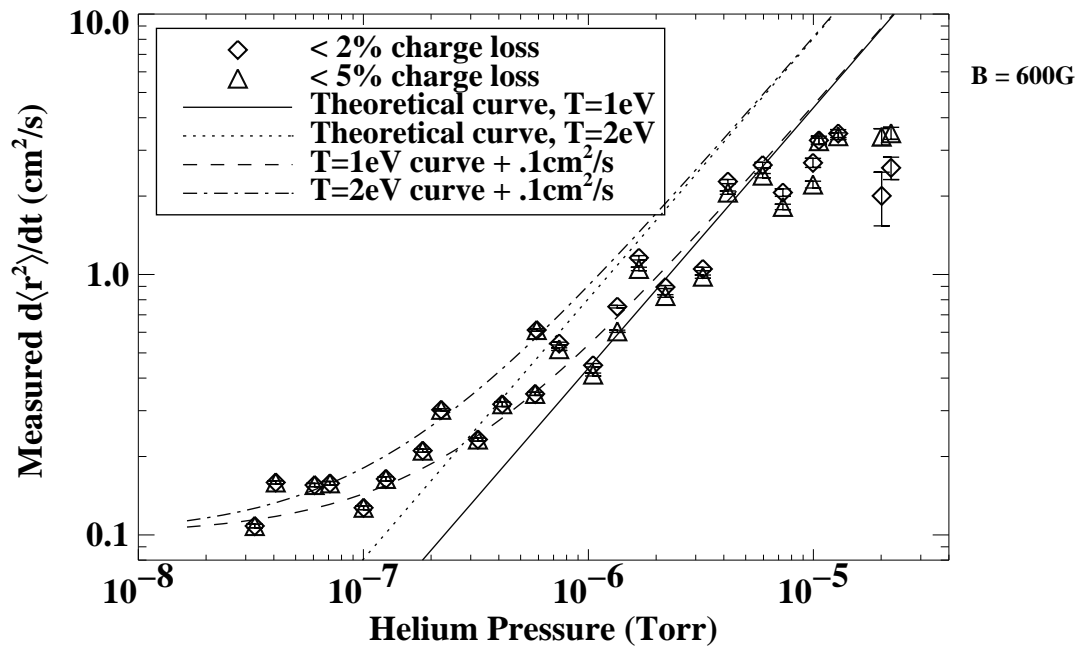


Figure 4.10: Small-filament-plasma expansion rate vs. pressure at $B = 600 \text{ G}$. For this data, $N_L \approx 3.4 \times 10^7$ electrons/cm.

$P \approx 1 \times 10^{-5}$ Torr fall below the theoretically predicted curves by as much as a factor of five. This discrepancy could be due to noise in the density profiles, but suspiciously coincides with increases in the filament heating voltage (raised ultimately to $V_h = 6.8$ V) to counter the decrease in the filament emission and total plasma charge as the gas pressure is increased. (This decrease is suspected to be caused by cooling of the filament surface by the gas, which would change the rate of thermionic emission.) The earlier, large-filament data do not show this feature, and the heating and bias voltages were hardly changed at all when measuring that data. In section 5.2.1, the hypothesis that the discrepancy is due to $m = 1$ diocotron mode growth is discussed.

Figure 4.11 shows small-filament expansion rate data taken at $B = 300$ G that more convincingly follows the theoretically predicted curve for $T = 2$ eV with an offset of $0.35 \text{ cm}^2/\text{s}$. Presumably, this data set has less scatter because the faster plasma expansion at $B = 300$ G is more easily measured. The two different expansion rate computations (for diamonds and triangles) match for several of the lower-pressure points in Figures 4.10 and 4.11 because less than 2% of the total charge was lost throughout those expansions and the number of mean-square radius points used in the calculations is identical.

For the small-filament expansion rate data, thermal quasi-equilibrium profiles could not be reliably fit to the density profiles. Temperature inferences are therefore not available for comparison to the values suggested by the expansion rate curves. This is because plasmas produced with the smaller filaments are small enough that the electron density changes appreciably over the area of the collimating hole ($R_p \sim 4R_h$, in fact), and a more complicated profile should be used; to fit this data, an azimuthally symmetric, theoretical 2-D density profile created from a

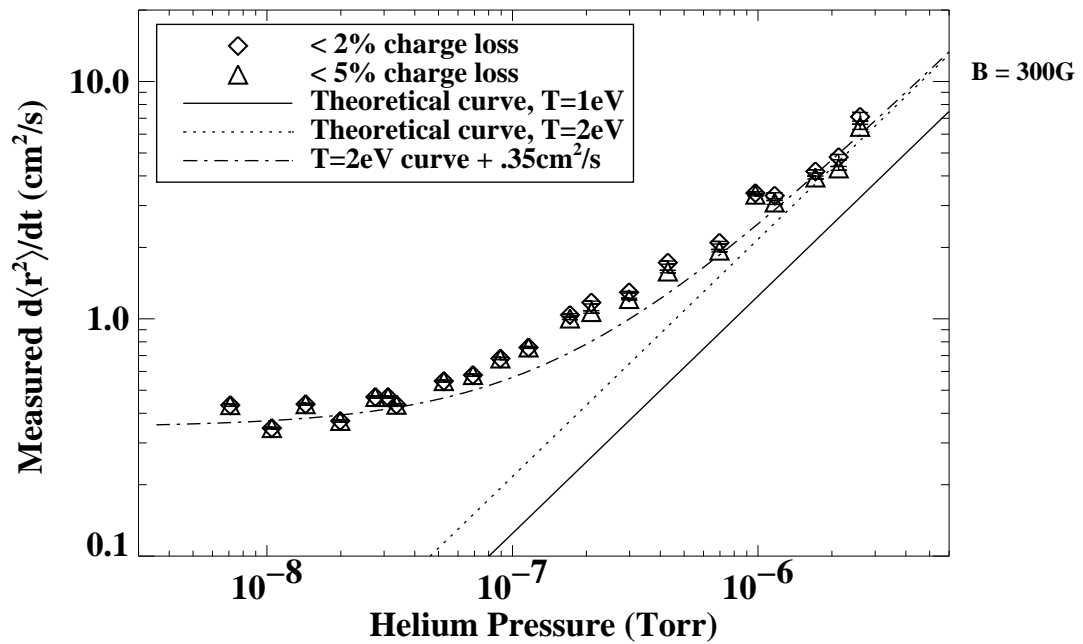


Figure 4.11: Small-filament-plasma expansion rate vs. pressure at $B = 300\text{ G}$. For this data, $N_L \approx 3.3 \times 10^7$ electrons/cm.

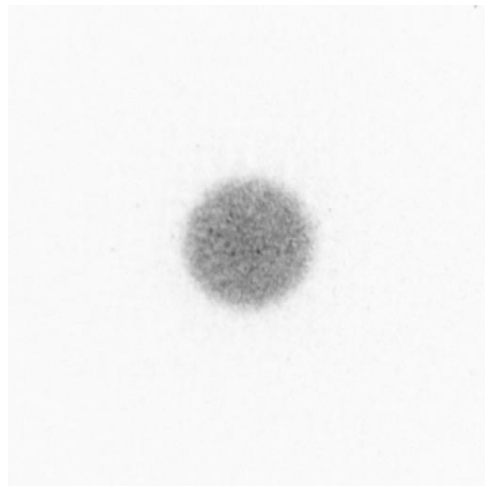
thermal quasi-equilibrium radial density profile must be integrated over the area of the collimating hole at each radial location observed. Since the thermal quasi-equilibrium density profile used to make the 2-D profile is a numerical solution of Eq. (3.48) and Poisson's equation [Eq. (3.39)], the integral over the collimating hole area must also be numerical, and the predicted density profiles are no longer very sensitive to the inferred plasma temperature due to numerical noise. The predicted profile measurement is also quite sensitive to the diagnostic alignment with the trap; if the collimating hole travels across the plasma on a chord that does not intersect the plasma axis, the integral over the collimating hole area can be strongly affected (since $R_p \sim 4R_h$). In addition, the measured density profiles upon inspection appeared somewhat peaked at $r = 0$, making a fit more problematic [see Fig. 2.11(b)]. Though no comparison can be made with inferred temperatures, it is interesting to note that the expansion rate data for the large filament at $B = 610$ G and for the small filament at $B = 300$ G suggest an effective temperature of $T = 2$ eV, and the expansion rate data for the large filament at $B = 300$ G and for the small filament at $B = 600$ G instead suggest $T = 1$ eV.

Both the large- and small-filament data suggest a linear dependence of the plasma expansion rate $(d/dt)\langle r^2 \rangle$ on the background gas pressure above a minimum level of expansion. Since the plasma expansion rates measured at higher pressures where temperature gradients could exist ($\nu_{en} \gg \nu_{ee}$) are consistent with the rates predicted for uniform-temperature plasmas, it would seem that any temperature gradients in the plasma do not have a dramatic effect on the plasma expansion.

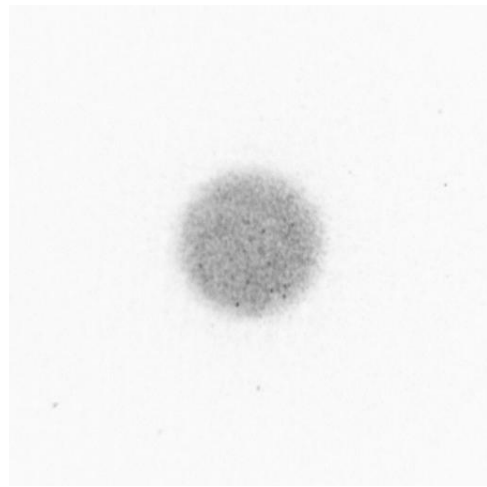
4.2.4 Phosphor-Screen Data

The next improvement to the EDG device diagnostic set was the replacement of the Faraday-cup density diagnostic with a phosphor-screen density diagnostic (see section 2.2.2), which can produce an entire axially integrated, 2-D density profile for an individual plasma. This new diagnostic allows better measurement of small-filament plasma density profiles and allows the measurement of density profiles when large diocotron modes are present. It also eliminates several sources of noise in the plasma density profiles by both greatly reducing the amount of time necessary to take the profile measurement and optically coupling the profile measurement to the recording electronics. Each image of a single plasma provides a better radial density profile than determined previously from a minimum of 85 separate plasmas (17 radial locations \times 5 readings) with the Faraday-cup density diagnostic. Examples of FFT-filtered images of expanding plasmas taken with this diagnostic are presented in Fig. 4.12.

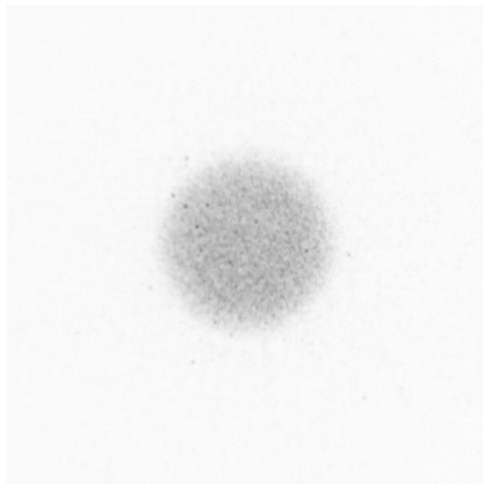
The speed with which the phosphor-screen density diagnostic can record a 2-D density profile allows reliable measurement of the plasma evolution well past 1 second before the trap conditions change appreciably. Figure 4.13 shows a plasma mean-square radius evolution taken with this diagnostic at $P \approx 6 \times 10^{-9}$ Torr [MORRISON *et al.*, 2003], where asymmetry-induced expansion is expected to dominate the plasma behavior. The most interesting feature of this data is the nonlinear evolution between $t = 0$ seconds and $t = 3$ seconds (the “initial phase” of the expansion). The rate is clearly changing with time in the initial phase of the plasma expansion and relaxing to the steady rate observed after $t = 3$ seconds (in the “later phase” of the plasma expansion). It is tempting to identify the initial phase of the plasma evolution as a relaxation to thermal quasi-equilibrium of an



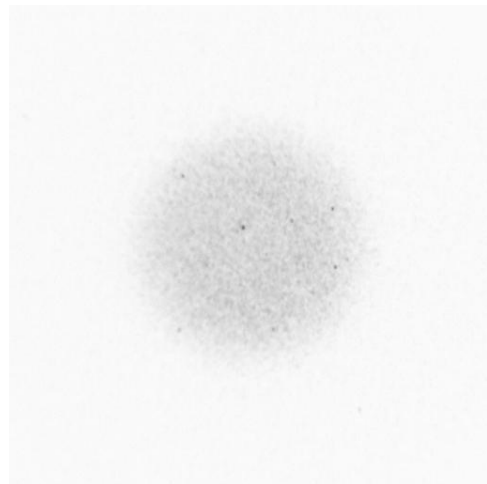
(a) Trapped for 1/3 s.



(b) Trapped for 1 s.



(c) Trapped for 3 s.



(d) Trapped for 15 s.

Figure 4.12: Images of expanding plasmas at $P \sim 6 \times 10^{-9}$ Torr. These images were used to determine the density profiles shown in Fig. 4.1.

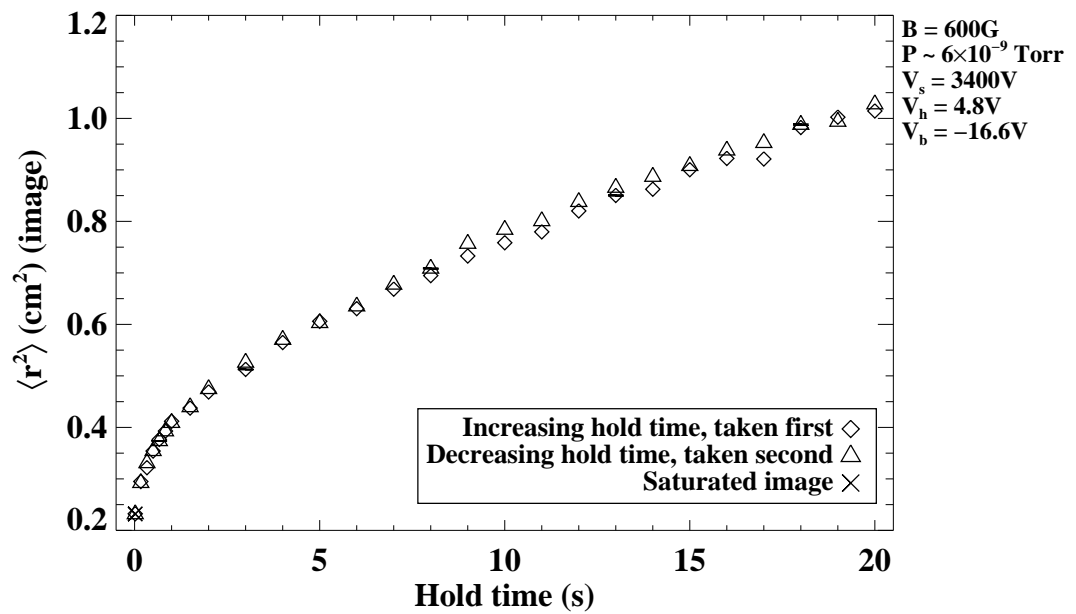


Figure 4.13: The plasma mean square radius as a function of time at $P \approx 6 \times 10^{-9}$ Torr. For this data, $B = 600$ G and $N_L \approx 3.3 \times 10^7$ electrons/cm. The agreement between the data taken while increasing the hold time and decreasing the hold time (the time the plasma is held in the trap) indicate the plasma's reproducibility and the uncertainty in the mean-square radius. The few error bars plotted illustrate the uncertainty in the mean-square radius due to the nature of the calculation.

initially non-equilibrium plasma and identify the later phase of the evolution as the true asymmetry-induced plasma expansion at this pressure. This would mean that all the expansion rates determined from the Faraday-cup density diagnostic data were computed for plasmas that were not in thermal quasi-equilibrium. Supporting this hypothesis is the fact that the initial phase of the evolution is observed to be quite similar for different filament voltages and background gas pressures below $P \sim 2 \times 10^{-7}$ Torr. This three-second evolution of the plasma to thermal quasi-equilibrium disagrees with the estimated characteristic time for density equilibration of about 30 seconds computed in section 3.1.2, which is interpreted to mean that a realistic estimate is only possible by taking into account the details of the plasmas' density and temperature profiles.

Expansion rates determined from the later phase of the plasma expansion are compared with the early-phase expansion rates from Fig. 4.10 in Fig. 4.14 [MORRISON *et al.*, 2003]. In Figure 4.14, it is again clear that the late-time expansion rates can be much lower than what was previously thought to be the minimum, asymmetry-induced expansion rate in the plasma. The new, late-time rates at the lowest pressures are expected to be the true asymmetry-induced expansion rates, and the difference between them and the previous values is characteristic only of the initial plasma relaxation. In fact, expansion rates estimated from the first ~ 0.5 seconds of phosphor screen data for the two low-pressure evolutions agree with the $0.1 \text{ cm}^2/\text{s}$ threshold rate identified in Figures 4.6 and 4.10. At $P \approx 1 \times 10^{-6}$ Torr, where the plasma is expanding much more quickly than the plasma can relax, the rate computed during the plasma relaxation *is* indicative of the collisionally induced plasma expansion and agrees fairly well with the previous data set.

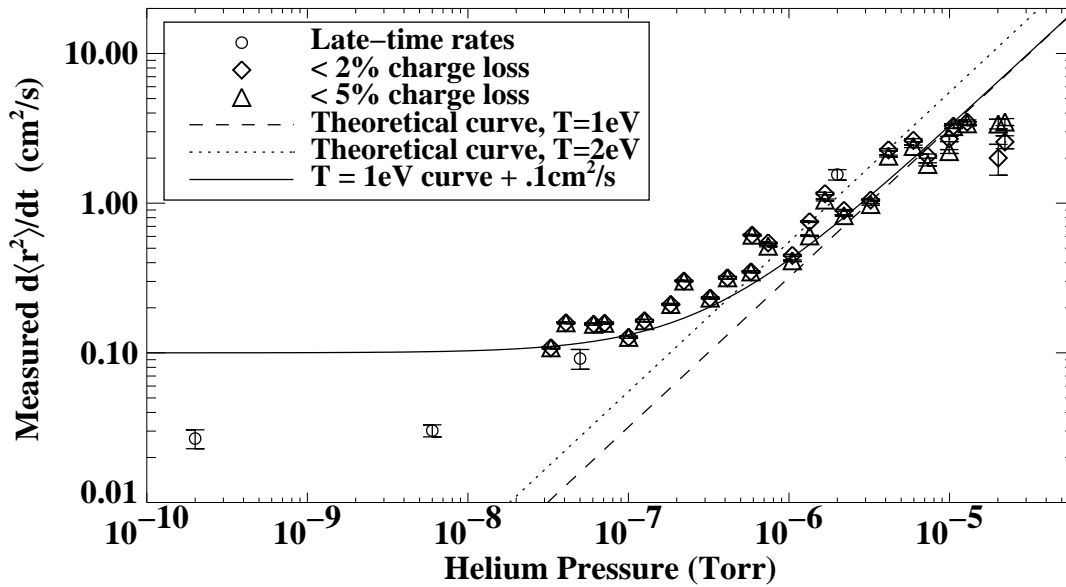


Figure 4.14: Comparison of expansion rates determined from the Faraday-cup and phosphor-screen density diagnostics for small-filament plasmas at $B = 600$ G. The circles denote the new expansion rates obtained by excluding the initial plasma relaxation where possible.

Even with the ability to scrutinize extended plasma evolutions, it is apparent from the difference between the two lowest-pressure late-time expansion rates that the changes in expansion due to differences in background pressure below $P \approx 1 \times 10^{-8}$ Torr are still minute compared to the asymmetry-induced expansion, and the improved measurements of the expansion rate are not particularly sensitive indicators of the background gas pressure in this range.

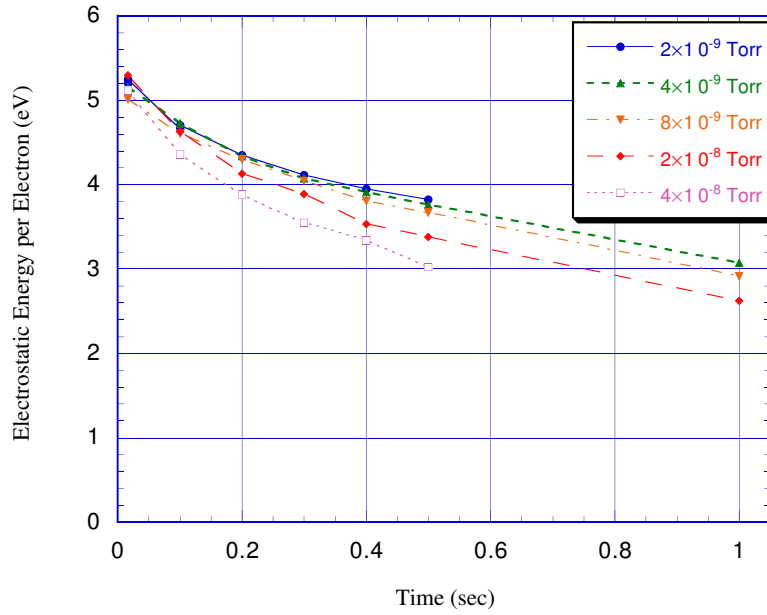
4.3 Temperature Evolution

The best way to determine whether the plasma is in thermal quasi-equilibrium is to observe its temperature profile. Since this is somewhat difficult to do, more convenient, $r = 0$ parallel temperature evolutions have been measured instead. The plasma temperature is also a factor in the plasma expansion rate, and it is important to see whether the increasing inferred temperatures observed for the data in Fig. 4.9 are indicative of the true plasma temperatures. Increasing temperatures are to be expected because of energy conservation (as described in section 4.3.1), but have not been observed at the lowest pressures in EDG.

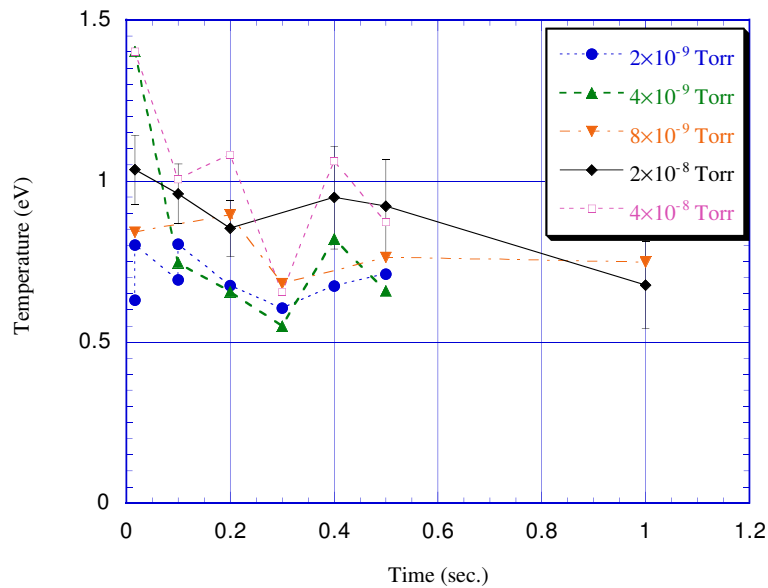
4.3.1 Review of the Inferred Temperature Data

Figure 4.15 shows a comparison between the estimated electrostatic potential energy per particle and the inferred electron temperatures obtained from the early, large-filament density profile data. [CHAO *et al.*, 2000] The electrostatic potential energy per particle is given ideally by

$$U_e = \frac{1}{N} \int dV \frac{|\mathbf{E}|^2}{8\pi} = -\frac{1}{N} \int dV \left(\frac{en\phi}{2} \right), \quad (4.8)$$



(a) Electrostatic potential energy.



(b) Inferred perpendicular temperature.

Figure 4.15: Earlier energy evolution results from large-filament plasmas. (Reproduced from [CHAO, 1999], with permission.)

where $\mathbf{E} = -\nabla\phi$ is the electric field, and the reported values in Fig. 4.15(a) are computed using the n and ϕ determined from the Poisson solver code. It is apparent from Fig. 4.15(a) that electrostatic potential energy is liberated as the plasma expands. Because (1) collisions between helium atoms and electrons are very elastic for $T < 4$ eV, (2) the magnetic field is low enough that very little energy is radiated from the plasma, (3) the plasmas are well separated from the trap electrodes, and (4) the computed quasi-equilibrium rotational kinetic energy per electron

$$K_\phi = \frac{1}{N_L} \int_0^{R_w} dr r \frac{m_e (r\omega_r)^2}{2} \int dz d\phi n(r, \phi, z) \quad (4.9)$$

$$= \frac{1}{2} m_e \omega_r^2 \langle r^2 \rangle \quad (4.10)$$

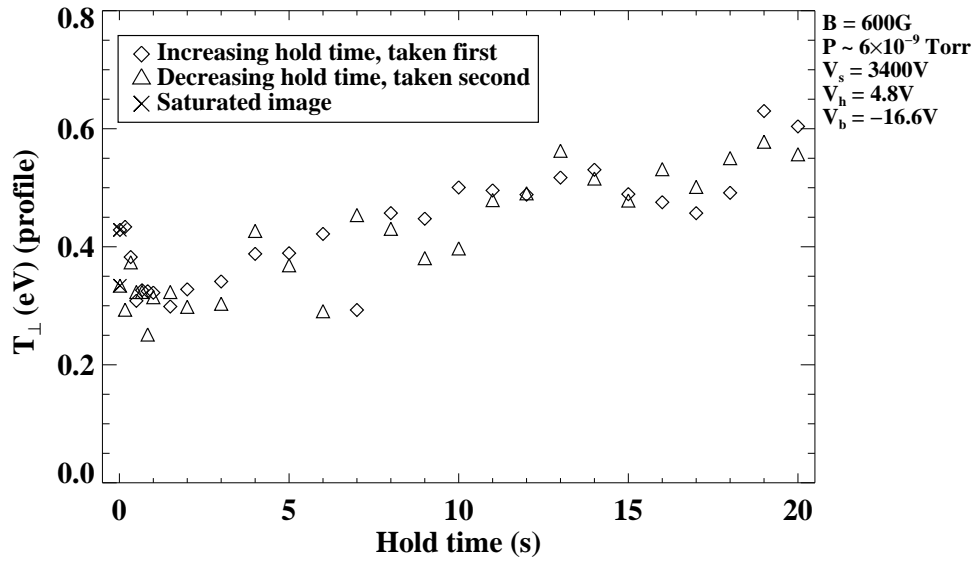
is negligible, one would expect that the plasma would be heated by the additional energy. Figure 4.15(b) instead shows that the inferred temperatures in the first second of evolution do not increase with time. The original explanation for this behavior was that trace amounts of impurity gases (e.g., hydrocarbons, water, nitrogen) experiencing highly inelastic collisions with the trapped electrons must be present to absorb the excess plasma energy. The density evolutions measured with the phosphor screen diagnostic (e.g., in Fig. 4.13), however, suggest that the plasma isn't in thermal quasi-equilibrium until approximately $t = 3$ seconds, so these temperatures inferred in the early phase of the evolution might not be accurate.

To verify that trace gases are affecting the energy evolution, in Fig. 4.15(b) the inferred temperature evolution must be shown to be representative of the true electron temperature evolution and the plasmas must be shown to not be in contact with the trap electrodes. The best way to verify the temperature inferences is to compare them with temperatures measured directly, and this is the purpose of this section. The phosphor-screen diagnostic data described in section 4.2.4 (and

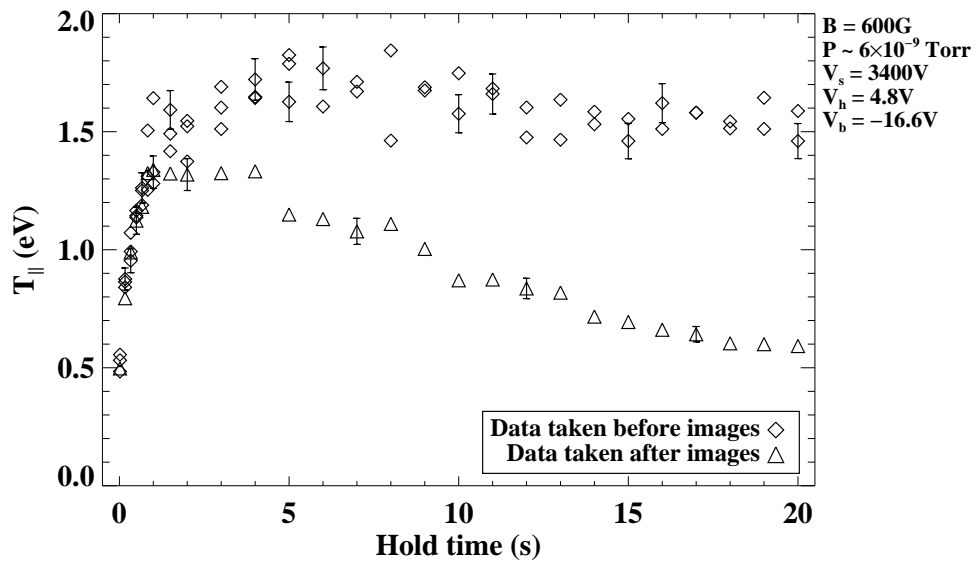
shown in Fig. 4.1) has indicated that the plasmas are well removed from the trap electrodes for the first 15 seconds of plasma expansion at $P \approx 6 \times 10^{-9}$ Torr, removing the second concern. While using a Residual Gas Analyzer (RGA) to determine the gas species present in the trap would be a direct way to confirm that trace gases were involved in the dynamics, no sufficiently ultra-high-vacuum-compatible RGA was available to make this measurement.

4.3.2 Comparison of Inferred and Measured Temperature Evolutions

The parallel electron temperature evolution at $r = 0$ was measured at the same conditions as density profile evolutions at $P \approx 6 \times 10^{-9}$ Torr and $P \approx 2 \times 10^{-6}$ Torr [MORRISON *et al.*, 2003]. Figure 4.16(a) shows that the inferred perpendicular temperatures at $P \approx 6 \times 10^{-9}$ Torr (determined from the density profiles used to make Fig. 4.13) do not change appreciably during the plasma evolution, since the inferred temperatures are only estimated to be accurate to within ± 0.25 eV. Figure 4.16(b) shows the measured temperature evolution for the same plasma conditions, and it is apparent that the parallel temperature at $r = 0$ increases by approximately 1 eV in the first couple seconds of plasma evolution, in contrast with the inferred temperature evolutions in Figures 4.15(b) and 4.16(a). However, the measured parallel temperature is only indicative of the temperature at $r = 0$ rather than the total plasma kinetic energy until it is certain that the plasma has a uniform temperature (e.g., in the later phase of the expansion when the plasma is clearly in thermal quasi-equilibrium). The initial evolution of the measured temperatures,



(a)

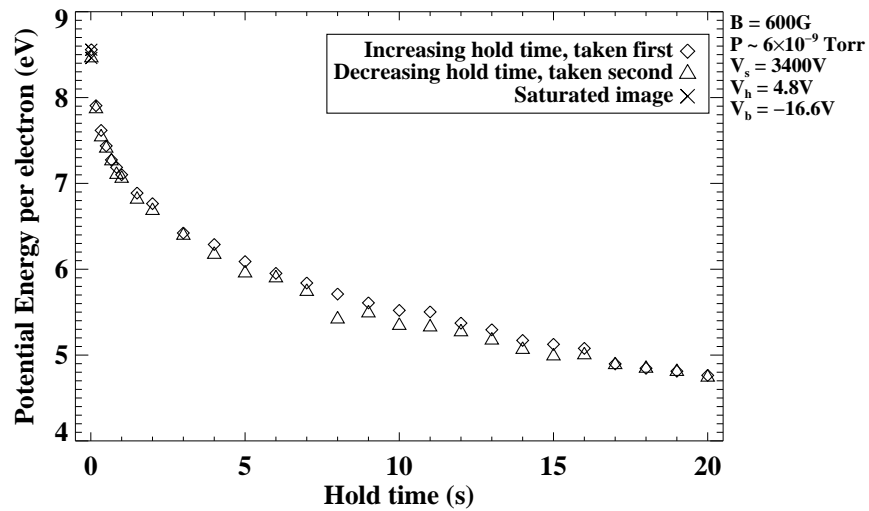


(b)

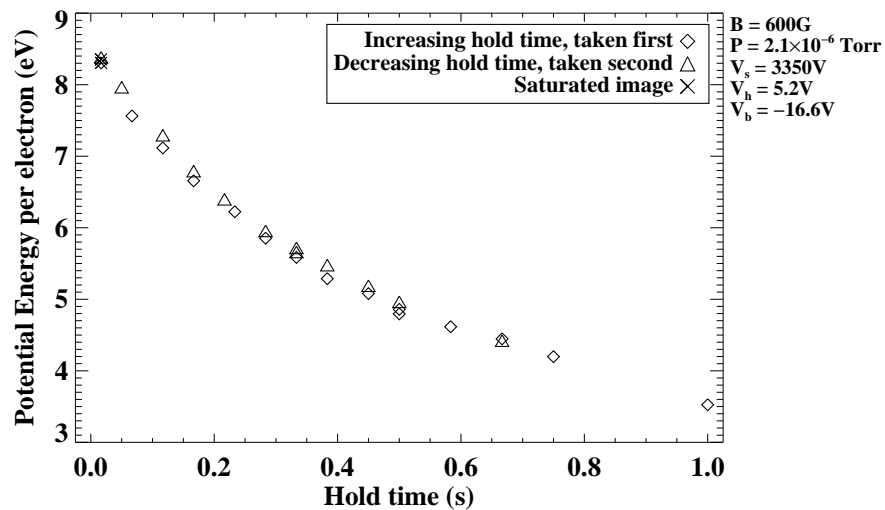
Figure 4.16: The inferred perpendicular temperature evolution (a) and the measured, on-axis parallel temperature (b) at $P \approx 6 \times 10^{-9}$ Torr. For this data, $B = 600$ G and $N_L \approx 3.3 \times 10^7$ electrons/cm.

which takes approximately 1 second, is consistent with the characteristic energy transport times of approximately 0.5 seconds estimated in section 3.1.2.

The initial measured temperature increase primarily indicates that the plasma is relaxing to thermal quasi-equilibrium. This is especially evident because the measured temperatures do not increase in the later phase of the expansion even though the plasma expands more in the later phase than it does in the initial phase (see Fig. 4.13); the estimated electrostatic potential energy evolution in Fig. 4.17(a) clearly shows that just as much potential energy is liberated after $t = 3$ seconds as in the initial expansion. The inconsistency of there being both non-increasing measured temperatures and decreasing electrostatic potential energy again suggests that trace background gas molecules that undergo inelastic collisions with the plasma electrons are draining kinetic energy from the plasma. This hypothesis is consistent with the discrepancy in Fig. 4.16(b) between the data sets represented by diamonds and triangles because the set represented by diamonds was taken at a lower partial pressure of gases desorbed from the trap surfaces than the set represented by triangles. (The partial pressure of these desorbed gases is observed to increase with time after the filament is turned on.) A higher partial pressure of the desorbed gas, which presumably contains the trace gas molecules, would drain energy from the plasma more quickly, explaining why the plasma temperature decreases more quickly. To make a proper comparison between the change in electrostatic energy and the change in the plasma temperatures, it should be noted that the change in the parallel temperature should be $\Delta T_{\parallel} = (1/3) \Delta U_e$ and the change in the perpendicular temperature should be $\Delta T_{\perp} = (2/3) \Delta U_e$ for a given change in the electrostatic potential energy ΔU_e , because of energy equipartition.



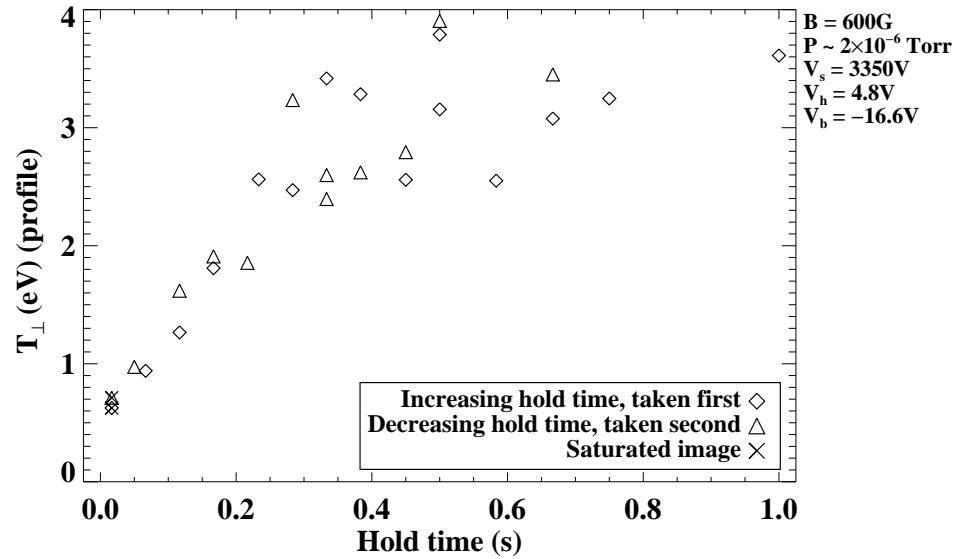
(a)



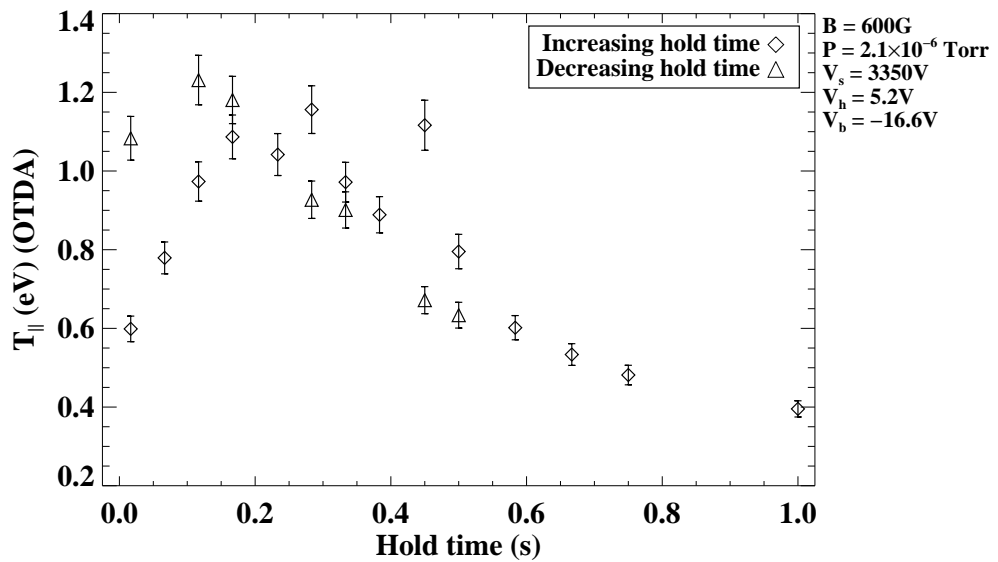
(b)

Figure 4.17: Estimated electrostatic potential energy evolution. The data in Fig. 4.17(a) is determined from the axially integrated density profiles used to make the perpendicular temperature inferences in Fig. 4.16, and the data in Fig. 4.17(b) corresponds to the data in Fig. 4.18. The potential energy per electron is calculated by estimating the electric field from the axially integrated density profiles. The error bars estimated for this data are much smaller than the size of the plot symbols, and are omitted.

Temperature measurements were also made at $P \approx 2 \times 10^{-6}$ Torr, where the electron-neutral collisions are more frequent than electron-electron collisions ($\nu_{en} \gg \nu_{ee}$) and temperature gradients could easily form. Figure 4.18(b) shows the measured temperature evolution at this pressure, which is also seen to increase initially. The plasma loses 2% of its electrons by about $t = 0.4$ seconds (not shown), and the measured temperatures quickly decrease just before that point. It would appear that the plasma equilibration is interrupted by interactions between the plasma and the trap electrodes. In contrast, the inferred temperatures from the density profiles increase dramatically during the evolution [Fig. 4.18(a)], and only stop increasing about the time that the plasma is suspected to be in contact with the trap electrodes. The measured parallel temperatures at $P \approx 2 \times 10^{-6}$ Torr do not increase any more than they did at the low pressures in spite of the quick increase in the inferred temperatures, further supporting the hypothesis that the plasmas are not in thermal quasi-equilibrium. Since the plasma is apparently not in thermal quasi-equilibrium, the change in the inferred temperatures is only indicative of how fast the plasma density profile shape is changing as the plasma quickly expands; the temperatures inferred are not expected to be representative of the actual temperature profile in the plasma. Trace gases experiencing inelastic collisions with the electrons are again invoked to explain the discrepancy between the measured temperatures in Fig. 4.18(a) and the calculated change in electrostatic potential energy in Fig. 4.18(b). At these pressures, where the plasma does not have time to reach thermal quasi-equilibrium, inferring the plasma temperature from the density profile is not a useful endeavor. As a result, the rapidly increasing inferred temperatures for the $B = 300$ G expansion rate data in Fig. 4.9 are not meaningful.



(a)



(b)

Figure 4.18: The inferred perpendicular temperature evolution (a) and the measured $r = 0$ parallel temperature (b) at $P \approx 2 \times 10^{-6}$ Torr. For this data, $B = 600$ G and $N_L \lesssim 3 \times 10^7$ electrons/cm. The density profile data used to compute T_{\perp} in Fig. 4.18(a) was taken between the T_{\parallel} data sets represented by the diamonds and triangles.

The finding that the small-filament plasmas are not in thermal quasi-equilibrium until $t \approx 3$ seconds in the evolutions also affects the understanding of other measurements made of EDG plasmas. The plasma expansion rate in the asymmetry-induced expansion regime was previously observed to be proportional to $B^{-3/2}$ [CHAO *et al.*, 2000], but since this was determined using plasmas trapped for less than 1 second, this dependence is now interpreted to be characteristic of the plasmas' relaxation to thermal quasi-equilibrium as a function of B. It should therefore be compared to the estimated dependences in Eqs. 3.70

$$\frac{1}{\tau_n^{E \times B}} \propto \left(\frac{n}{B}\right)^2 \ln\left(\frac{n^{3/2} b^4 m_e c \bar{v}}{B e} (\lambda_D \sqrt{n})\right)$$

$$\frac{1}{\tau_n^{\text{class}}} \propto \left(\frac{n}{B}\right)^2 \ln\left(\frac{1}{B} \frac{m_e c \bar{v}}{e b}\right),$$

[determined from the estimates for the characteristic density relaxation times $\tau_n^{E \times B}$ and τ_n^{class} in Eqs. (3.21) and (3.24)] instead of the B^{-2} dependence in Eq. (3.46) for thermal quasi-equilibrium plasmas. This comparison, though, is still not satisfying because the estimates in Eqs. 3.70 do not appear to describe the suspected density equilibration time in EDG (see section 4.2.4). The expansion rates used in the preliminary $B^{-2.2}$ dependence measured at higher pressures [MORRISON *et al.*, 2001], though, should not be overly affected by the relaxation process and still constitute a fair result. In addition, the $m = 1$ diocotron mode evolutions discussed in Chapter 5 and measured previously [CHAO *et al.*, 2000; CHAO, 1999; CHAO *et al.*, 1999b] are often strongly influenced by the behavior of the mode in the first few seconds of plasma evolution, sometimes because that is precisely the interesting part of the evolution. The best way to overcome this difficulty would be to use an applied, "rotating-wall", electric-potential asymmetry [HOLLMANN *et al.*, 2000a] to better confine the plasma until it had time to fully equilibrate before releasing it

to observe the ensuing dynamics, but this amount of investment was not available for this thesis work. It is, of course, possible that the large-filament plasmas were closer to thermal quasi-equilibrium at $t = 0$ and took less time to equilibrate than the small-filament plasmas do, but the similar initial-phase expansion rates and similar decrease in the expansion rate near the end of the evolutions suggest that the equilibration takes a similar amount of time for both large- and small-filament plasmas.

Lastly, it is reassuring to note that both of the the plasma evolutions observed with the phosphor-screen diagnostic at $P \approx 2 \times 10^{-6}$ Torr and $P \approx 5 \times 10^{-8}$ Torr show that the later-phase plasma expansion changes noticeably after approximately 2% of the total plasma charge has been lost. This is evident from the measured and inferred temperature evolutions at $P \approx 2 \times 10^{-6}$ Torr and from a clear change in the mean-square-radius evolution at $P \approx 5 \times 10^{-8}$ Torr (not shown). These observations indicate that the expansion rates calculated for the data recorded before 2% of the total charge was lost (in Figures 4.6, 4.9, 4.10, and 4.11) are more representative of unperturbed plasma expansion than the 5%-lost rate calculations.

4.4 Summary of Plasma Expansion Studies

In this chapter, measurements of the plasma density profile and temperature evolutions demonstrate that the plasma indeed expands linearly with pressure when the effects of trap field asymmetries are negligible, in agreement with the

prediction for uniform-temperature plasmas. This plasma expansion rate dependence on pressure has been measured at $B = 300$ G and $B \approx 600$ G for two different initial plasma radii, and is not observed to be affected by interactions between the plasma and the trap electrodes. High-resolution density profiles taken with the new phosphor-screen density diagnostic in the asymmetry-induced expansion regime suggest that this expansion rate data was taken during the plasma's initial, nonlinear relaxation to thermal quasi-equilibrium. This suspicion was confirmed by the quick increase in the on-axis ($r = 0$) parallel temperature measured with the new, on-axis temperature diagnostic amplifier. The improved density and temperature diagnostics show that EDG plasmas take approximately 3 seconds to reach a thermal quasi-equilibrium state when $\nu_{en} \ll \nu_{ee}$, which is similar to the observed behavior in other devices [DRISCOLL *et al.*, 1988]. It is surprising that these non-equilibrium plasmas expand at rates similar to the predicted rates for uniform-temperature plasmas above $P \approx 4 \times 10^{-7}$ Torr. This indicates that any temperature gradients that exist have a relatively small effect on the plasma expansion in EDG. The plasma expansion at low pressures is found to be almost entirely due to the plasma's relaxation to thermal quasi-equilibrium and the effects of trap asymmetries. Finally, the new, late-time expansion rates measured with the phosphor screen density diagnostic appear largely insensitive to the background gas pressure below $P \approx 1 \times 10^{-8}$ Torr.

The measured plasma temperature evolutions also indicate that the plasma temperature is not increasing during the newly identified asymmetry-induced expansion, so the liberated electrostatic potential energy leaves the plasma through some undetermined mechanism. The electrostatic potential energy is estimated from the axially integrated density profiles, and clearly changes by more than 1

eV/electron during the $P \approx 6 \times 10^{-9}$ Torr expansion. The non-increasing plasma temperatures suggest the possibility that the expected temperature gradients at HV gas pressures are suppressed in our plasmas by the energy loss mechanism, possibly explaining the agreement between our measured expansion rates and the theoretically predicted rates. It was illustrated previously [CHAO, 1999] that even a small number of gas molecules that experience strongly inelastic collisions with ~ 1 eV electrons could explain the drop in plasma energy, and this remains the most likely explanation for the lack of energy balance. Since the measured temperatures also disagree with the temperatures inferred from the density profiles, it is concluded that inferring the effective, thermal quasi-equilibrium plasma temperature when the plasmas are not fully in thermal quasi-equilibrium does not produce a representative measure of the plasma thermal energy.

Chapter 5

Measurements of $m = 1$ Diocotron

Mode Evolution

The $m = 1$ diocotron mode, an electrostatic surface wave with $k_z \approx 0$ (and described in section 3.4), is the most easily observed and controlled wave in Malmberg-Penning trap plasmas. Because EDG plasma expansion is not observed to be particularly sensitive to background gas pressure for $P \lesssim 10^{-8}$ Torr (see chapter 4), measurements were made of the $m = 1$ diocotron mode evolution to see if it was more dependent on the pressure [CHAO *et al.*, 2000; CHAO, 1999; CHAO *et al.*, 1999b]. This previous work showed that the diocotron mode evolution is indeed sensitive to pressure in the UHV regime, but the dependence was not readily explained by any existing theoretical model. Subsequent measurements described in this thesis have revealed that the $m = 1$ mode evolution is also very sensitive to other trap parameters, such as the choice of filament heating voltage. It is again clear that careful characterization of the trap conditions must be performed in order to use the evolution of this wave as a UHV pressure standard.

In this chapter, the comparisons made in the previous work [CHAO, 1999] between the $m = 1$ diocotron mode characteristics in EDG and in other similar plasmas are reviewed in section 5.1. Next, the newly observed sensitivity of the mode evolution to the electron source voltages is described in section 5.2. Finally, new measurements of the mode growth rate versus pressure are presented in section 5.3, and measurements of the transiting ions that are suspected to cause this destabilization (see section 3.4.2) are discussed in section 5.4.

5.1 Review of Basic Comparisons with Theory

In the previous study of the $m = 1$ diocotron mode evolution in EDG plasmas, care was taken to ensure that the observed modes agreed in all measurable ways with the $m = 1$ modes in other experiments and with the theoretical descriptions. In particular, the mode frequency and the mode's strong growth in the presence of resistive trap electrodes were observed, and these measurements are summarized here.

5.1.1 Agreement with Predicted Finite-Length Frequency

Section 3.4.1 describes the ways that the measured $m = 1$ diocotron mode frequency in a finite-length, Malmberg-Penning trap plasma should differ from the $m = 1$ diocotron mode frequency ω_D predicted for small-amplitude modes on an infinite-length electron column [LEVY, 1968]. Figure 5.1 [CHAO, 1999] shows a comparison between the measured frequencies and the corresponding, predicted, finite-length frequencies for EDG data using Eqs. (3.58) and (3.60) from section 3.4.1. It is clear that the measured EDG frequencies (the circles) are higher than the

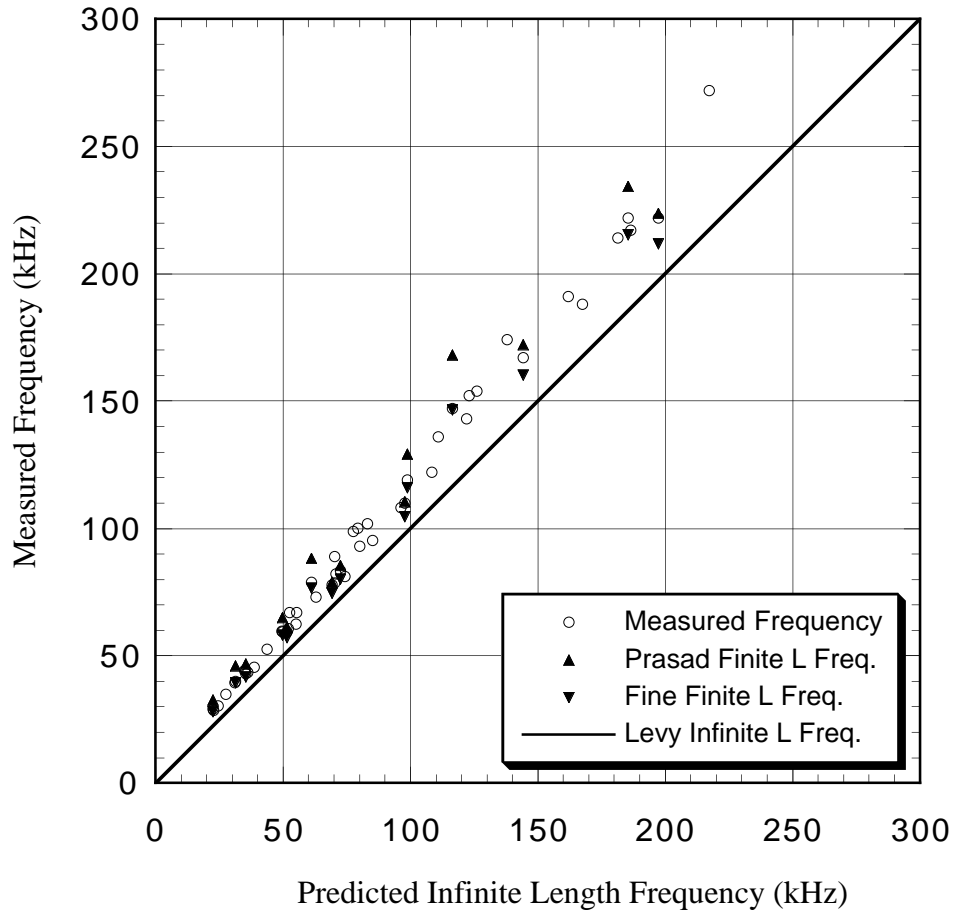


Figure 5.1: Plot of measured $m = 1$ diocotron mode frequencies and predicted finite-length mode frequencies versus the infinite-length $m = 1$ mode frequency. The mode frequency was adjusted by varying the plasma line density in the range $2 \times 10^7 \text{ electrons/cm} \leq N_L \leq 6 \times 10^7 \text{ electrons/cm}$ and the magnetic field in the range $92 \text{ G} \leq B \leq 614 \text{ G}$. The circles represent the measured frequencies, the solid line represents the infinite-length-plasma mode frequency, the upright, solid triangles are the values produced using Eq. (3.60) [PRASAD and O'NEIL, 1983], and the inverted triangles are those predicted using Eq. (3.58) [FINE and DRISCOLL, 1998]. (Reproduced from [CHAO, 1999], with permission.)

infinite-length diocotron mode frequency (the solid line), and appear consistent with both sets of finite-length frequency predictions (the triangles). The scatter in both the frequency data and the predicted values is too great to confirm the finding in other experiments [FINE and DRISCOLL, 1998] that the frequency prediction in Eq. (3.58) (that considers the plasma to be in a dynamic equilibrium) is the better one, however. The plasma radius R_p used in the finite-length frequency predictions for EDG was estimated from the density profile data to be $R_p \approx \sqrt{2 \langle r^2 \rangle}$, while the plasma radius used for the study confirming Eq. (3.58) [FINE and DRISCOLL, 1998] was defined as the radial point where the density dropped to half of its $r = 0$ value [$n(R_p) = n(r = 0)/2$]. However, these two calculations should not differ markedly.

The additional, $(\Delta f/f_0) \propto (D/R_w)^2$ frequency shift in Eq. (3.61) for large-amplitude ($D/R_w \lesssim 1$) modes was also observed [CHAO, 1999] by exciting the mode to large amplitudes with a resistive trap electrode (see section 5.1.2). These measurements give us confidence that we are properly measuring the plasma frequency and mode amplitude (the plasma “displacement” off the trap axis).

5.1.2 Resistive-Wall Mode Growth

Appreciable electrical resistance between points on a trap electrode’s surface and the point of zero potential (“ground”) can have a strong effect on the growth rate of the $m = 1$ diocotron mode [WHITE *et al.*, 1982], as described in section 3.4.2. The dependence of the diocotron mode growth rate on an applied resistance between an azimuthally discontinuous trap electrode and the point of zero potential was previously measured in EDG [CHAO *et al.*, 2000; CHAO, 1999], and the results are presented in Fig. 5.2. The solid line in Fig. 5.2 is the theoretical

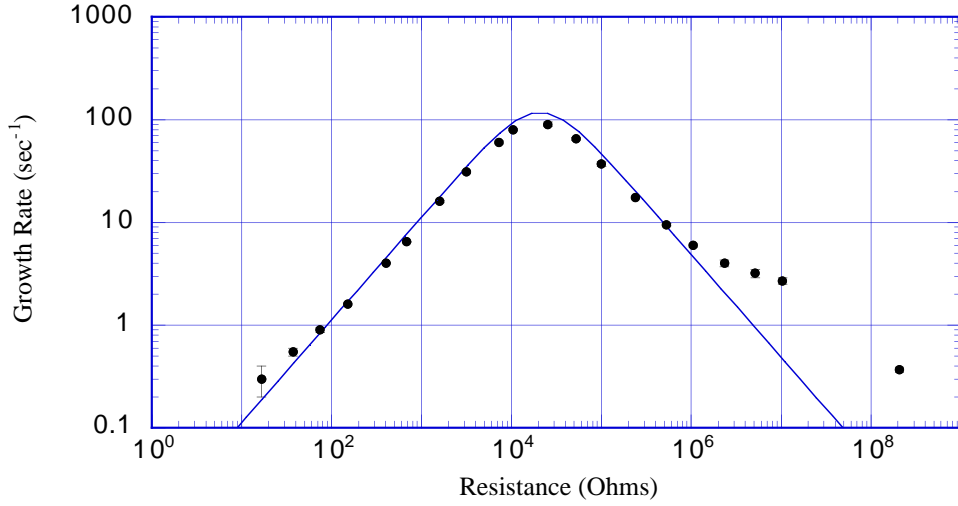


Figure 5.2: Plot of the diocotron mode growth rate vs. electrode resistance to ground. For this data, $B = 610$ G and $\omega_D/2\pi \approx 38.0$ kHz, which corresponds to $N_L \approx 3.3 \times 10^7$ electrons/cm. (Reproduced from [CHAO, 1999], with permission.)

prediction in Eq. (3.68), and exhibits the characteristic shape given by the factor $\gamma_R \propto \text{Real}\{Z\} = R/(1 + (\omega_D RC)^2)$. The impedance Z between the electrode and the point of zero potential is a combination of the inherent $C = 200$ pF capacitance to ground of the the trap electrode (either electrode 3 or 4), the inherent cable capacitance, and a metal-oxide resistor in parallel. The data agree rather well with the predicted growth rates and the prior experimental data up to a resistance of $R \approx 10^6 \Omega$, but the growth rates measured above $R \approx 10^6 \Omega$ are unexpectedly large. The source of the discrepancy at high resistances has not been determined [JENKINS *et al.*, 2002] and could represent some novel plasma effect, though non-ideal behavior by the applied resistors or the measurement amplifiers has not been completely ruled out.

With the phosphor screen diagnostic, this exponential growth can be confirmed by determining the plasma displacement from successive plasma images and fitting the evolution with an exponentially increasing curve. This procedure has been

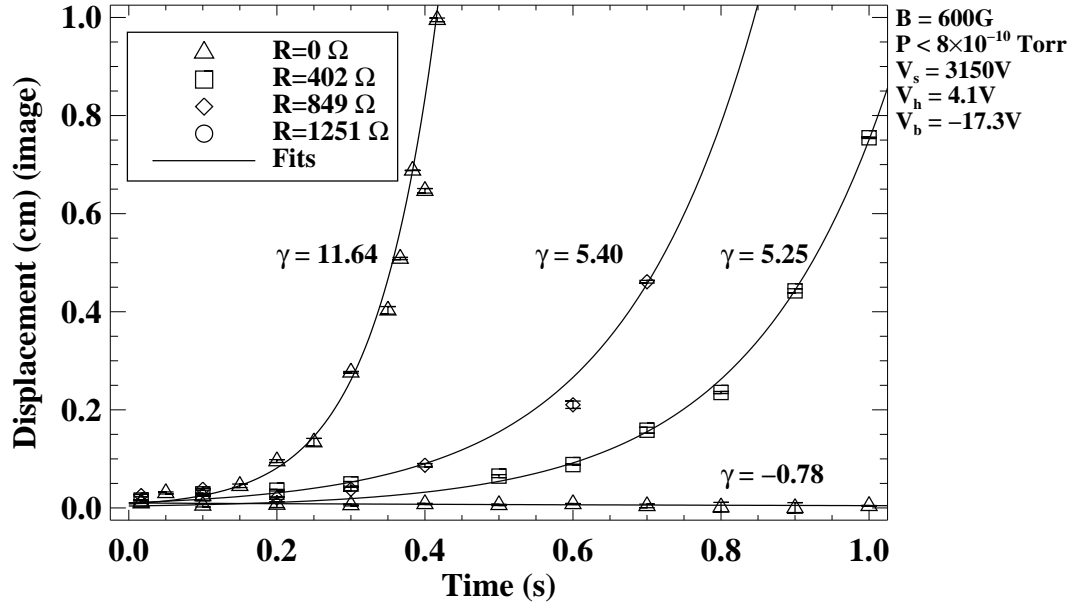


Figure 5.3: Image-derived diocotron mode amplitude vs. time using three different resistors. For this data, $V_b = -17.34 \text{ V}$, $V_h = 4.1 \text{ V}$, $B = 600 \text{ G}$, $P \lesssim 1 \times 10^{-9} \text{ Torr}$, and $N_L \approx 3.5 \times 10^7 \text{ electrons/cm}$. This data was taken before the magnetic field alignment was improved with the Helmholtz coils. Note that the error bars are smaller than the plot symbols in all cases.

performed for small-filament plasmas, and the results are displayed in Fig. 5.3. The growth rates estimated from the image-computed displacements agree well with the theoretically predicted values plotted in Fig. 5.2. The evolution of the plasmas' root-mean-square radius can also be calculated from the image data, and is shown in Fig. 5.4. The root-mean-square radius data shows that the plasma does not expand decidedly faster at low pressures when a quickly growing $m = 1$ diocotron mode is present than when it is not. Points for which the plasma was obviously distorted by proximity to and possible contact with the trap electrodes have been omitted from Figures 5.3 and 5.4.

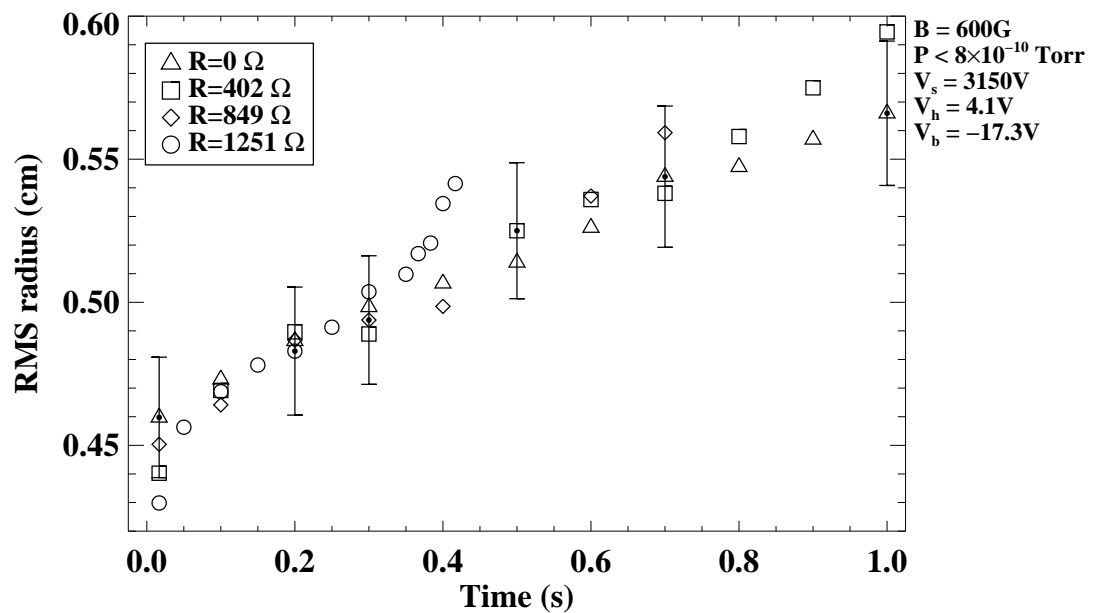


Figure 5.4: Plasma root-mean-square radius evolutions for the data in Fig. 5.3. Black dots are additionally plotted inside the symbols to which the characteristic error bars apply.

Strong mode growth is produced so reliably in the presence of a resistive trap electrode that researchers sometimes introduce a resistor momentarily (using a relay) to produce large initial diocotron mode amplitudes. The subsequent evolution of the mode is observed once the resistor is again eliminated from the circuit. Any amplitude dependence of the mode growth has not been adequately investigated in EDG, however.

5.1.3 “Anomalous” Mode Damping

One unexpected observation made during the characterization of the diocotron mode behavior in EDG was of an underlying exponential damping [$D \propto \exp(\gamma_{\text{anom}} t)$, where $\gamma_{\text{anom}} < 0$] with a growth rate γ_{anom} varying roughly as $(N_L/B)^2$. The data demonstrating this behavior is presented in Fig. 5.5. These measured growth rates were compared to the predicted growth rates for rotational pumping [Eq. (3.65)] and for coupling between the $m = 1$ diocotron mode and Landau-damped, $k_z \neq 0$ plasma modes [Eq. (3.71)]. It was noted that rotational pumping is independent of the magnetic field B , and the mode-coupling theory (which does have an approximately $\gamma_{\text{mc}} \propto \omega_\infty^2$ dependence) predicts growth rates that are an order of magnitude too large (and negative). The “anomalous” damping’s scaling is similar to that of some types of asymmetry-induced plasma expansion and the density profile relaxation timescales in Eq. (3.70). It has therefore been hypothesized that plasma expansion is involved in the mode damping, as it is in rotational pumping. No clear relationship other than the rotational pumping mechanism has been made between mode damping and plasma expansion in the literature, however.

With an appropriate selection of plasma parameters (particularly, $B \sim 600$ G), the effects of this “anomalous” damping are minimized in EDG.

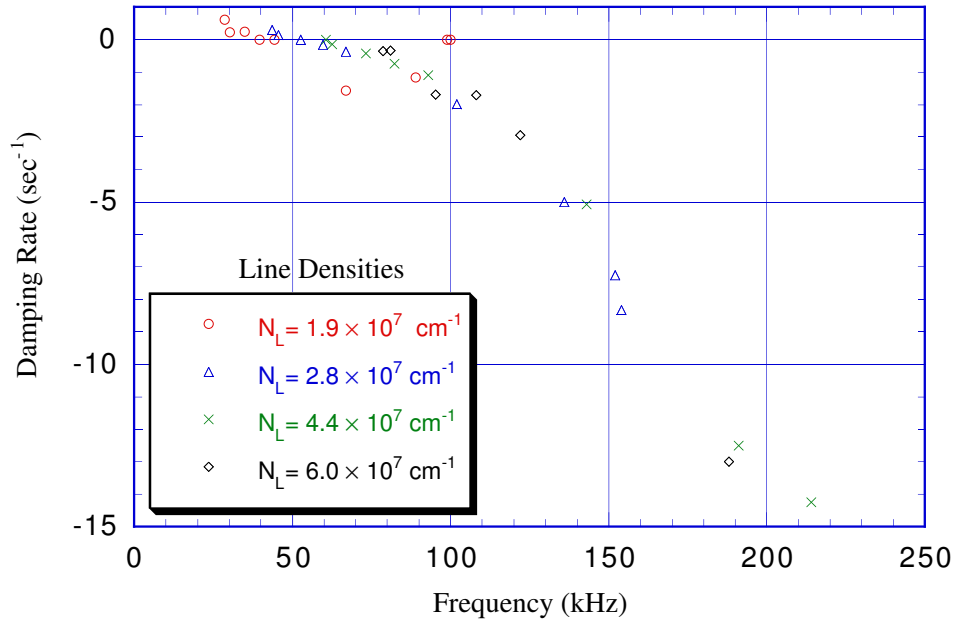


Figure 5.5: Plot of the diocotron mode growth rate vs. frequency. The diocotron mode frequency was adjusted by varying the line density in the range 1.9×10^7 electrons/cm $\leq N_L \leq 6 \times 10^7$ electrons/cm and the magnetic field in the range $160 \text{ G} \leq B \leq 620 \text{ G}$. This data was taken at a base pressure of $P \approx 3 \times 10^{-9}$ Torr, a heating voltage of $V_h = 8 \text{ V}$, and bias voltages $V_b = -7.9 \text{ V}$, -11 V , -14.2 V , and -17.4 V . Note that the mode grows at the lowest values of N_L/B [$\omega_D/(2\pi) < 50$ kHz]. There is no measured change in the total plasma charge during this damping. (Reproduced from [CHAO, 1999], with permission.)

5.2 Mode Sensitivity to Filament Conditions

With the knowledge that resistive-trap-electrode growth and anomalous damping can affect the $m = 1$ diocotron mode dynamics, further measurements have been made of the evolution that indicate additional influences on the mode. The $m = 1$ diocotron mode evolution in EDG is observed in this thesis research to be unexpectedly sensitive to the conditions in the electron source. In this section, the mode growth rate as a function of the filament heating voltage V_h and filament bias voltage V_b for small-filament plasmas is presented, and the choices of these seemingly unimportant trap parameters are seen to strongly influence the mode dynamics.

5.2.1 Influence of Filament Heating Voltage

For plasma conditions where the “anomalous” damping measured previously should be small, the mode is observed to grow at increased filament heating voltages. Figure 5.6 shows the increase in the diocotron mode growth rate with increasing heating voltage V_h . The range of the growth rates observed here is just as large as the range of growth rates measured previously for the “anomalous” damping, except with a constant magnetic field and a slowly varying total plasma charge. In fact, none of the plasma parameters calculated using the density diagnostics [N , $\max(dn/dr)$, $\langle r^2 \rangle(t = 0)$] vary greatly with the heating voltage in this range. In the plot, the data represented by the diamonds, circles, and triangles was taken after the filament assembly and trap had become heated by the filament and the pressure had risen to readings of 1.5×10^{-10} Torr $< P < 1 \times 10^{-9}$ Torr, while the squares represent the data taken first, at around $P \sim 1.5 \times 10^{-10}$ Torr.

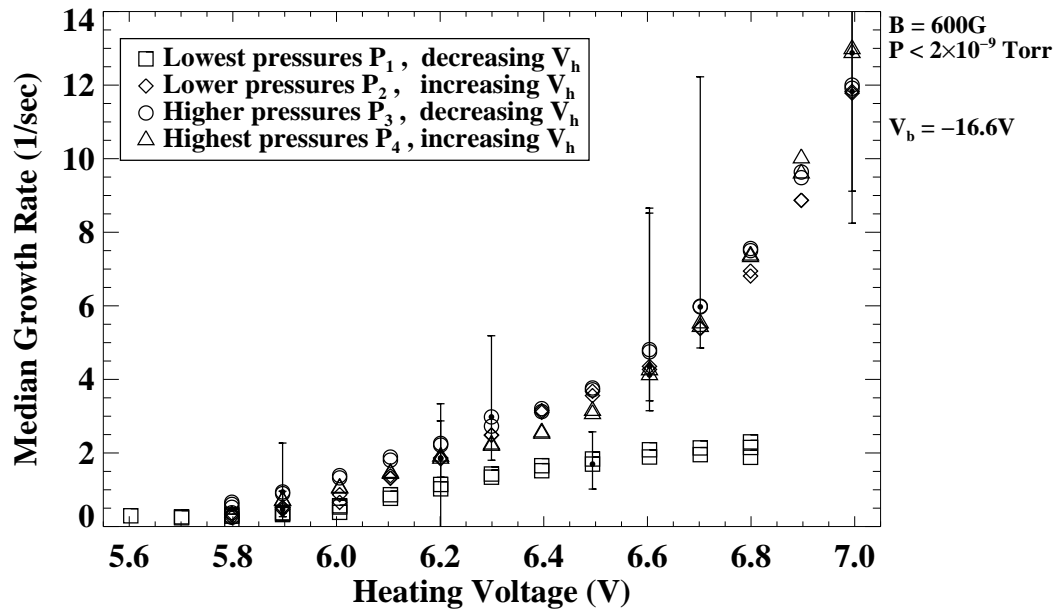


Figure 5.6: Diocotron mode growth rate vs. filament heating voltage at $V_b = -16.7$ V, $\omega_D/(2\pi) \approx 48$ kHz (corresponding to $N_L \approx 4 \times 10^7$ electrons/cm), and $B = 600$ G. The median growth rate is calculated by taking the median value of the diocotron mode growth rate between the point where the voltage signal from the diocotron mode amplifier rises above $A = 0.02$ V and the point where its slope dA/dt is a maximum. The high and low values of the growth rate in this subset of the evolution are indicated with “error bars” for a few points, but the uncertainty in the median growth rate is clearly much smaller because of the small spread of the data represented by diamonds, triangles, and circles. The fact that the high value is generally much further away from the median than the low value indicates that most of the difference is due to the changing growth rate rather than to noise. Black dots are additionally plotted inside the symbols to which the high and low value bars apply.

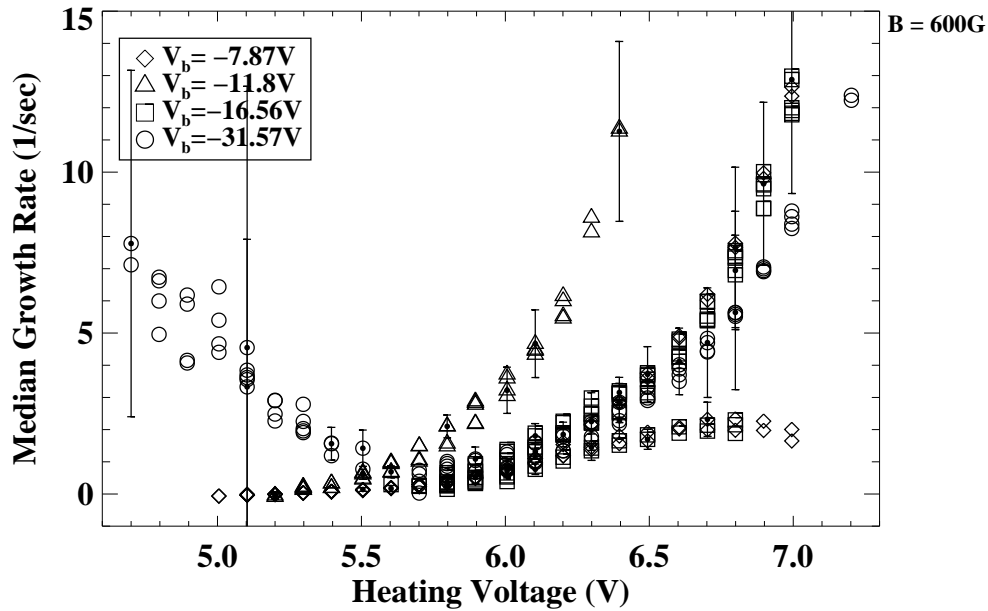


Figure 5.7: Plot of the median diocotron mode growth rate γ vs. heating voltage V_h for several values of bias voltage V_b . The median growth rate is computed in the same manner as for the data in Fig. 5.6, but the “error bars” plotted here represent the standard deviation of the points between $A = 0.02$ V and the point where dA/dt is a maximum. The standard deviation is shown instead because the high and low values for some of the data are excessively affected by noise. For this data, $B = 600$ G. (A different analysis of this data was presented previously in [PAUL *et al.*, 2003].)

Similar behavior is observed at several different values of filament bias voltage, as demonstrated in Fig. 5.7. Again, the $V_b = -7.87$ V and $V_b = -16.6$ V data that are below the $V_b = -31.57$ V data were taken at slightly lower pressures than the rest of the data at these two bias voltages. The difference between the growth rates at lower and higher pressures was thought to be an undetermined mechanical (surface chemistry) requirement that the filament warm up fully, but is now thought to have been an early sign of the pressure dependence of this mode growth (see section 5.3.2). The $V_b = -31.57$ V data in this plot show that the mode can also grow

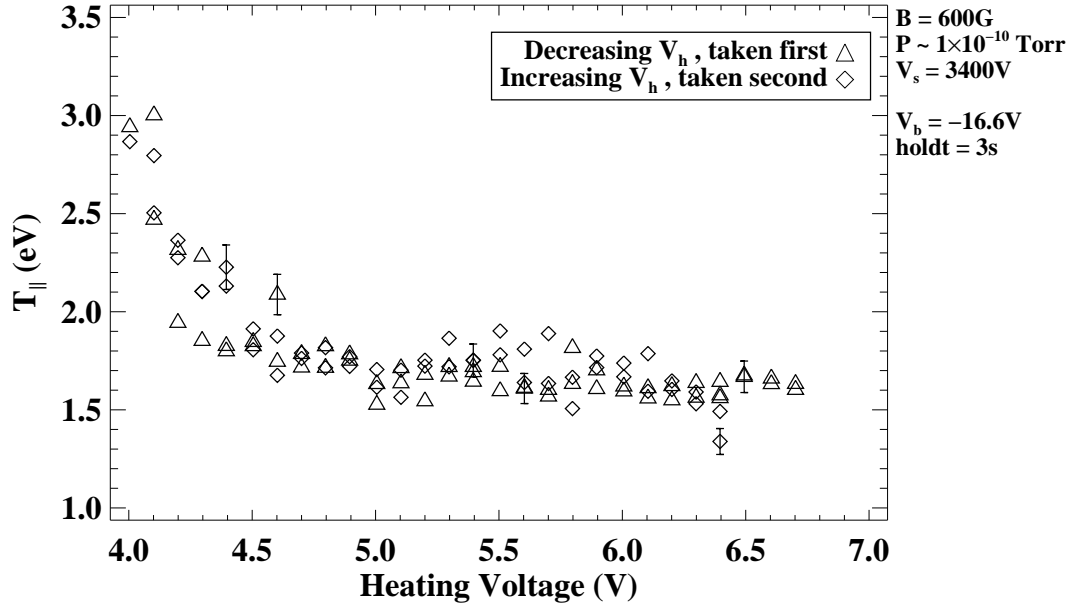


Figure 5.8: Plot of the measured parallel temperature $T_{||}$ vs. filament heating voltage V_h . For this data, the plasmas were held in the trap for $t = 3$ seconds, $V_b = -16.6$ V, and $B = 600$ G.

strongly at heating voltages below $V_h = 5.5$ V. For this part of the data, the mode frequency decreases as the heating voltage is decreased, implying that the plasma line density is also decreasing. An explicit line-density dependence of the growth rate has not been measured for this thesis work, but the “anomalous” damping data (Fig. 5.5) suggests that the mode would be less damped at lower line density.

Since the mode growth rate generally increases with heating voltage, it is conceivable that the electrons emitted at the higher heating voltages are imparted additional kinetic energy that somehow affects the mode growth rate. To test this, the parallel temperature as a function of V_h was measured after the plasma had time to equilibrate ($t = 3$ seconds). As shown in Fig. 5.8, it does not vary in the interesting range $5\text{ V} < V_h < 7\text{ V}$ to within the sensitivity of the diagnostic. Each of the

data points in Fig. 5.8 is from an individual plasma, with the data represented by the triangles taken first. In the absence of additional information, it was originally conjectured that the dependence of the growth rate on the heating voltage could therefore only be due to some subtle details of the density and temperature profiles that are not obviously correlated to the mode growth but somehow critical to the evolution. Instead, it is now hypothesized that all the measured mode growth at high heating voltages ($V_h > 5.5$ V) is due to transiting ions passing through the plasma axially and destabilizing the mode. This phenomenon is described in section 3.4.2, and measurements of ions produced by the EDG filament assembly are presented in section 5.4.

This dependence of the $m = 1$ mode growth on heating voltage is thought to explain the discrepancy between the measured and predicted plasma expansion rates around $P \approx 1 \times 10^{-5}$ Torr in Fig. 4.10. The $m = 1$ mode is observed to grow quite strongly at $V_h = 6.8$ V, which is the heating voltage used for the highest pressure data in Fig. 4.10. Also taking into account the mode growth's pressure dependence (see section 5.3.2), it is possible that the mode grew very quickly, causing the plasmas to interact almost immediately with the trap electrodes. This behavior could have been misinterpreted as slower plasma expansion because of the limitations of the Faraday-cup density diagnostic.

5.2.2 Influence of Filament Bias Voltage

Changes in the filament bias voltage were also shown to affect the growth rate of the $m = 1$ diocotron mode at sufficiently high heating voltages, as illustrated in Fig. 5.9. This data shows that the mode growth rate slowly increases with increas-

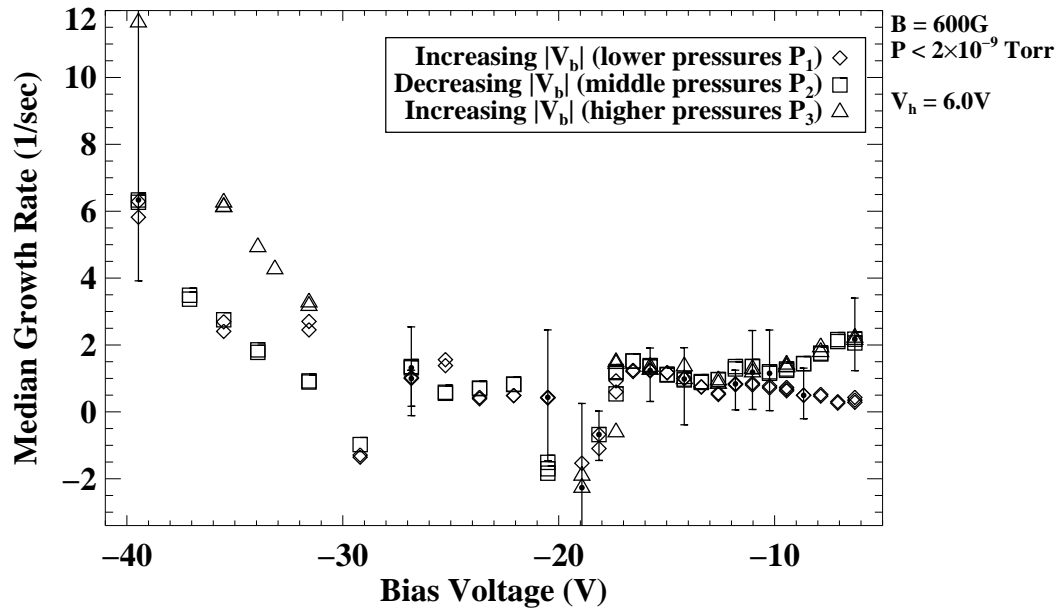


Figure 5.9: Plot of the median diocotron mode growth rate vs. bias voltage. For this data, $V_h = 6$ V, $B = 600$ G, and the mode frequency varies in the range $17.5 \text{ kHz} \lesssim \omega_D/2\pi \lesssim 79 \text{ kHz}$ (corresponding to 1.5×10^7 electrons/cm $\lesssim N_L \lesssim 6.7 \times 10^7$ electrons/cm). The data was calculated in a manner similar to that for the data in Fig. 5.6, but the median damping rates for points where $\gamma \lesssim 0$ were calculated either using the mode evolution from the point where the signal amplitude A was a maximum to the point where the signal amplitude dropped to $A = 0.02$ V, or all the data above $A = 0.02$ V if the presence of growth or damping couldn't clearly be identified. The “error bars” plotted correspond to the high and low growth rate values in the chosen subset of the evolution.

ing bias voltage at low bias voltages ($V_b \gtrsim -2V_h = -12$ V) and sufficient background gas pressures (specifically, the data denoted by the triangles and squares), and that the growth rate increases with *decreasing* bias voltage at high bias voltages ($V_b \lesssim -5V_h = -30$ V). Similar behavior is observed for data taken at different heating voltages. For Figure 5.9, the filament heating voltage was set to a point where the heating voltage dependence showed clear diocotron mode growth ($V_h = 6$ V). Not surprisingly, the data represented by the diamonds was taken at the lowest pressures in the data set, while the data represented by the triangles and squares was taken after the pressure had risen to readings above $P \approx 3.1 \times 10^{-10}$ Torr. The data represented by the triangles was taken at a higher pressures than the data represented by the squares, so the data for $V_b \lesssim -30$ V suggests that increased pressure causes greater mode growth in this bias voltage range as well.

The dependence of the growth rate on filament bias voltage is not as surprising as the heating voltage dependence in section 5.2.1, because the plasma total charge N increases dramatically as V_b becomes more negative (from $N \approx 1 \times 10^8$ electrons to $N > 4.5 \times 10^9$ electrons in this data set) and the measured initial plasma radius increases from $R_p \approx 0.31$ cm to $R_p \approx 0.78$ cm. Even the changes in “anomalous” damping with N_L could be responsible for the decrease in growth rate with increasing total charge at low bias voltages ($V_b \gtrsim -12$ V). Additional data at extremely low bias voltages ($V_b > -4.5$ V) in Fig. 5.13 show that the growth rate eventually stops increasing with increasing bias voltage, presumably because the trapped electrons are too tenuous to support the mode and may only dubiously be called a plasma.

The high growth rates at the highest bias voltages ($V_b \lesssim -30$ V) occur for plasmas formed with $|V_b/V_h| > 4$, which is also true of the $V_b = -31.57$ V heating

voltage scan data in Fig. 5.7 (especially below $V_h = 5.5$ V). At the highest bias voltages in the bias voltage scan, the mode frequency is also observed to decrease as the ratio $|V_b/V_h|$ increases, but accompanying data taken with the total collector of the Faraday-cup density diagnostic indicates that the total charge increases linearly with decreasing bias voltage. Decreased line density is, therefore, neither suspected to be present nor to be responsible for the mode growth in either situation. The decreasing mode frequency is not explained at present.

The damping seen at some bias voltages in Fig. 5.9 always occurs immediately after the plasma is trapped, and it is possible that the initial expansion of the plasma as it relaxes to thermal quasi-equilibrium is somehow related. If so, a mode excited using the resistive-wall technique (see section 5.1.2) after the plasma is in thermal quasi-equilibrium might damp away at a different rate. For the majority of the growth rate data presented in this thesis, the modes either grow so strongly in the first second of plasma evolution or grow so continuously for several seconds that the initial relaxation of the plasma density profile is not expected to change the nature of the results markedly.

5.3 Mode Sensitivity to Pressure

Having identified a new regime of $m = 1$ diocotron mode behavior in EDG (see section 5.2), it is interesting to see if the dependence of the mode evolution on background gas pressure is different in that regime than that observed previously [CHAO *et al.*, 2000]. Specifically, a comparing the two could help reveal the mechanisms important for producing both behaviors. This section describes the former measurement of diocotron mode damping with increased background

gas pressure and new measurements of the pressure dependence of the filament-voltage-dependent growth.

5.3.1 Previous Measurements of the Mode Evolution Pressure Dependence

With the resistive-electrode and anomalous $(N_L/B)^2$ damping effects adjusted to produce slight damping at the base pressure, the mode was previously seen [CHAO *et al.*, 2000; CHAO, 1999] to damp more strongly as the background gas pressure was increased, as shown in Fig. 5.10. Pressure differences as small as $\Delta P \approx 5 \times 10^{-10}$ Torr produced measurable differences in the mode amplitude evolution that took roughly 8 seconds to discriminate. The sensitivity to background gas pressure is much better than for the expansion rate measurements in part because a measurement of the mode evolution can be made with just one plasma, while an expansion rate measurement with the Faraday-cup density diagnostic required the trapping of hundreds of plasmas. The non-exponential damping with pressure was slow enough that the plasma could have expanded to a point where it had some contact with the trap electrodes, though the seemingly constant plasma frequencies (to within 1% throughout the evolution) suggest that only a small amount of charge could have been lost.

5.3.2 Measurements of the Mode Growth Rate Dependence on Pressure

Duplicating the particular trap conditions that created the pressure sensitivity observed previously (Fig. 5.10, [CHAO *et al.*, 2000]) with the new small-filament

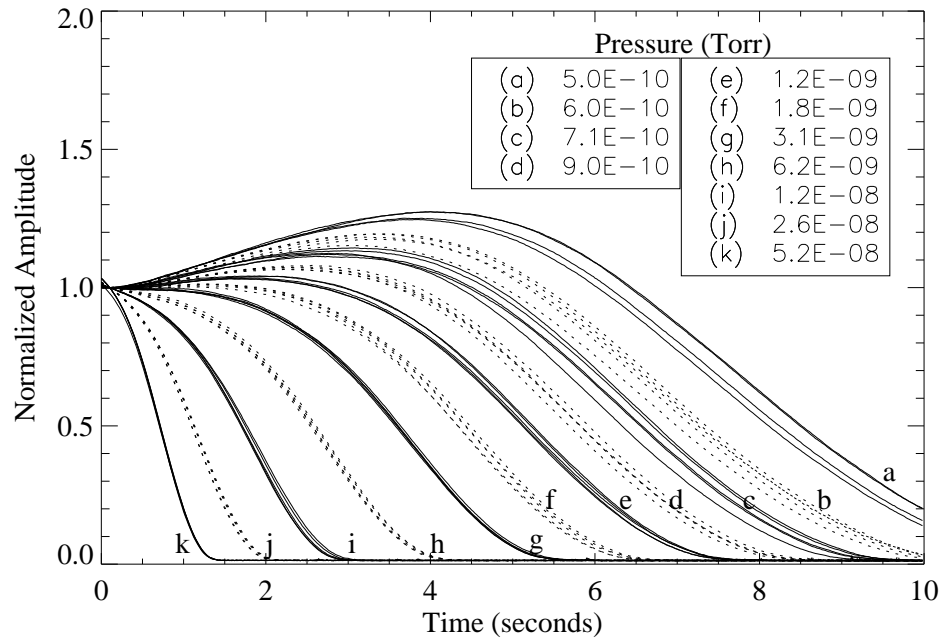


Figure 5.10: Amplitude evolution of the $m = 1$ diocotron mode. Each individual evolution is normalized by its value at $t = 0$ seconds. For this data, $B = 612$ G and $\omega_D/2\pi = 55$ kHz (corresponding to $N_L \approx 4.6 \times 10^7$ electrons/cm). Note that the pressure readings reported in this figure are the N_2 -equivalent pressures reported by the Bayard-Alpert ionization gauges, and the smallest pressure difference measured is in fact $\Delta P \approx 5 \times 10^{-10}$ Torr because the gauges are roughly five times less sensitive to helium gas than they are to nitrogen gas. (Reproduced from [CHAO, 1999], with permission.)

plasmas and a better-aligned magnetic field proved to be difficult, so an investigation was made into whether more controllable effects on the mode evolution were sensitive to gas pressure. The damping of modes in the presence of a slightly resistive trap electrode or modes initially excited to a large amplitude seemed to be rather insensitive to pressure [PAUL *et al.*, 2002] below $P \sim 10 \times 10^{-8}$ Torr. However, small discrepancies in that mode damping data suggested that the choice of filament voltages had an effect on the mode evolution, provoking the measurements described in section 5.2. With the observation that the mode was particularly sensitive to the filament conditions, a new opportunity for identifying a pressure-sensitive phenomenon presented itself.

The growth rate of the diocotron mode was first measured as a function of pressure at $V_h = 6$ V by simply allowing the filament to heat the device and drive off gases adsorbed to the trap surfaces. The results of this measurement are presented in Fig. 5.11. The constitution of this mixture of gases is unfortunately not known, but its effects are interesting, nonetheless, because the unknown, desorbed gases are almost certainly present even when helium gas is used to change the pressure for other data sets (increases in the helium partial pressure shouldn't appreciably affect the ability of the filament to heat the trap). In contrast to the increased damping at increased pressures observed previously, the mode growth rate measured here *increases* with increasing background gas pressure. This dependence is consistent with the differences in the filament-heating-voltage and bias-voltage growth rate data (in Figures 5.6 and 5.8) between the points taken before and after the pressure increased. Even the magnitude of the growth rate changes with pressure in Fig. 5.11 are consistent with those previous discrepancies. For the data in Fig. 5.11, differences in mode growth are evident for changes

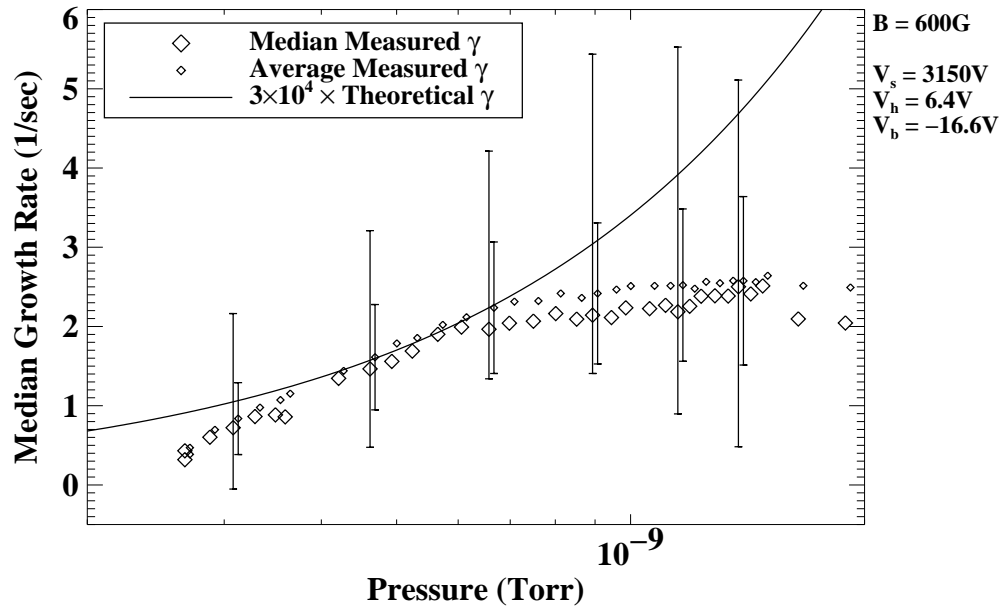


Figure 5.11: Growth rate vs. pressure at $V_b = -16.7\text{ V}$, $V_h = 6\text{ V}$, $B = 600\text{ G}$, and $\omega_D/2\pi \approx 47\text{ kHz}$ (corresponding to $N_L \approx 4 \times 10^7$ electrons/cm). The median growth rate (large diamonds) is again calculated by taking the median value of the mode growth rate between the point where the voltage signal from the diocotron mode amplifier rises above $A = 0.02\text{ V}$ and the point where its slope dA/dt is a maximum. The average growth rate (small diamonds) is the average value of the mode growth rate in this subset of the evolution. The high and low values of the growth rate are indicated by the “error bars” on the selected median growth rate data, and the standard deviation of the growth rate is indicated on the corresponding average growth rate points. The average growth rate points are shifted to a slightly higher pressure from the computed pressure for clarity, as can be clearly perceived from the points with “error bars”. The solid line is 3×10^4 times the theoretical growth rate γ_n for mode growth due to electron-neutral collisions.

in pressure as small as $\Delta P \approx 1 \times 10^{-10}$ Torr, which is an improvement over the previous mode damping measurements. Not much change is seen in the growth rate past $P \sim 1 \times 10^{-9}$ Torr, though, and it is possible that the mechanism producing the mode growth is saturated beyond this point. The theoretical growth rate $\gamma_n = \omega_\infty(\nu_{en}/\omega_{ce}) [\propto P]$ [Eq. (3.69)] for mode growth due to electron-neutral collisions is completely negligible compared to this pressure-dependent mode growth and the filament-voltage-dependent mode growth in section 5.2; the solid line plotted in Fig. 5.11 is 3×10^4 times the theoretical growth rate γ_n . Again, the plasma expansion is too fast for the prediction of collisionally induced mode growth to be applicable (see section 3.4.2).

Figure 5.12 shows a similar data set [PAUL *et al.*, 2003] where $V_b = -4.7$ V. In this data set, however, helium gas was used to adjust the pressure above $P = 2 \times 10^{-10}$ Torr, and the growth rates did not increase once helium was added; only the initial pressure changes due to the heating of the trap had a noticeable effect on the growth rate. This behavior might also ultimately be explained by the reason for the “saturation” of the growth rate data in Fig. 5.11, but another possible explanation for this behavior is discussed in section 5.4. The solid line again indicates how small the collisionally induced mode growth is for these plasmas.

For a clearer picture of how the growth rate sensitivity to pressure depends on filament bias voltage, growth rate data as a function of bias voltage was taken quickly at several background gas pressures below $P = 1 \times 10^{-8}$ Torr, and this data is displayed in Fig. 5.13 [PAUL *et al.*, 2003]. This data shows that the median growth rate increases with increasing background gas pressure for bias voltages in the range $-10 \text{ V} < V_b < -3.5 \text{ V}$. Mode growth is also seen for bias voltages in the range $-18 \text{ V} < V_b < -11 \text{ V}$ (which includes the $V_b = -16.6 \text{ V}$ value used for Fig. 5.11), but

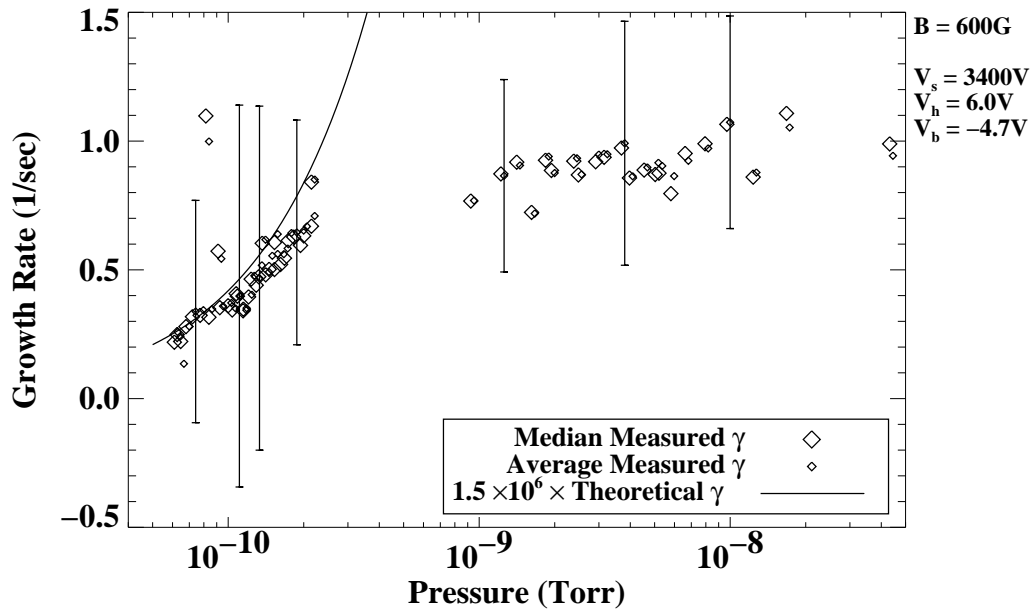


Figure 5.12: Median and average diocotron mode growth rate vs. pressure, where helium gas was used above $P = 2 \times 10^{-10}$ Torr. For this data, $V_b = -4.7$ V, $V_h = 6$ V, and $\omega_D/2\pi \approx 13.7$ kHz (corresponding to $N_L \approx 1.2 \times 10^7$ electrons/cm). The median and average diocotron mode growth rates are computed in the same manner as for the data in Fig. 5.11, but only the standard deviations of the growth rate evolution are displayed because the data was too noisy to have meaningful high and low growth rate values. The solid line shows that these growth rates are roughly a factor of 1.5×10^6 greater than the growth rates predicted for electron-neutral-collision-induced mode growth γ_n [Eq. (3.69)]. (A different analysis of this data was presented previously in [PAUL *et al.*, 2003].)

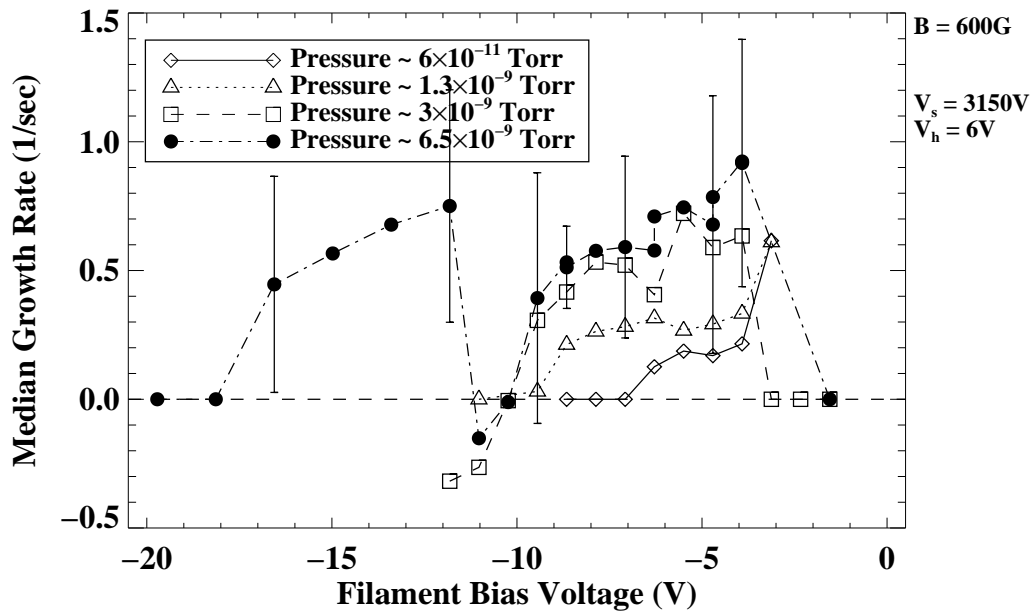


Figure 5.13: Diocotron mode growth rate vs. V_b at several background gas pressures. For this data, $V_h = 6\text{ V}$, $B = 600\text{ G}$, and $12\text{ kHz} \lesssim \omega_D/2\pi \lesssim 47.3\text{ kHz}$ (corresponding to $1 \times 10^7\text{ electrons/cm} \lesssim N_L \lesssim 4.0 \times 10^7\text{ electrons/cm}$). The median diocotron mode growth rate is computed in the same manner as for the data in Fig. 5.9, and the “error bars” show the standard deviation of the growth rate evolution for the $P \sim 1.5 \times 10^{-9}\text{ Torr}$ data. The points where $\gamma = 0$ indicate that no growth rate could be computed for the evolutions under those conditions, usually meaning that the maximum signal amplitude was below the chosen noise level $A = 0.02\text{ V}$.

not enough data is available to illustrate the pressure dependence there. For this plot, helium gas was used to help adjust the pressure. One interesting discrepancy between the data in Fig. 5.13 and the earlier bias-voltage data in Fig. 5.9 is that the newer data show no diocotron mode growth in the range $-10 \text{ V} \lesssim V_b \lesssim -11 \text{ V}$, even at pressures similar to those for Fig. 5.9. Recent mode growth data suggest that asymmetries in the confining fields affect the mode growth, and the improved field alignment used for the data in Fig. 5.9 may ultimately explain the appearance of this feature.

The data in this section (section 5.3.2) show a higher sensitivity to the background gas pressure in EDG than seen in the previous diocotron mode evolution data, with changes in pressure as small as $\Delta P \approx 3 \times 10^{-11}$ Torr (N_2 -equivalent) observed in Fig. 5.12. The pressure dependence for desorbed gas shown in Fig. 5.11 also suggests that the slight growth seen at low N_L/B in the “anomalous” damping is caused by the same mechanism (and is not part of the remaining $(N_L/B)^2$ dependence in Fig. 5.5), since the base pressure for that data was a reading of $P \approx 3 \times 10^{-9}$ Torr.

5.4 Transiting Ion Measurements

To determine whether previously undetected ions passing axially through the electron plasma are causing the mode growth at increased heating voltages (shown in sections 5.2 and 5.3.2), as described in section 3.4.2, the ion current emitted by the filament assembly as a function of background gas pressure is measured. This was accomplished by charging consecutive trap electrodes (e.g., electrodes 1–6) to a confining voltage (-150V) to repel any electrons produced, charging trap electrode

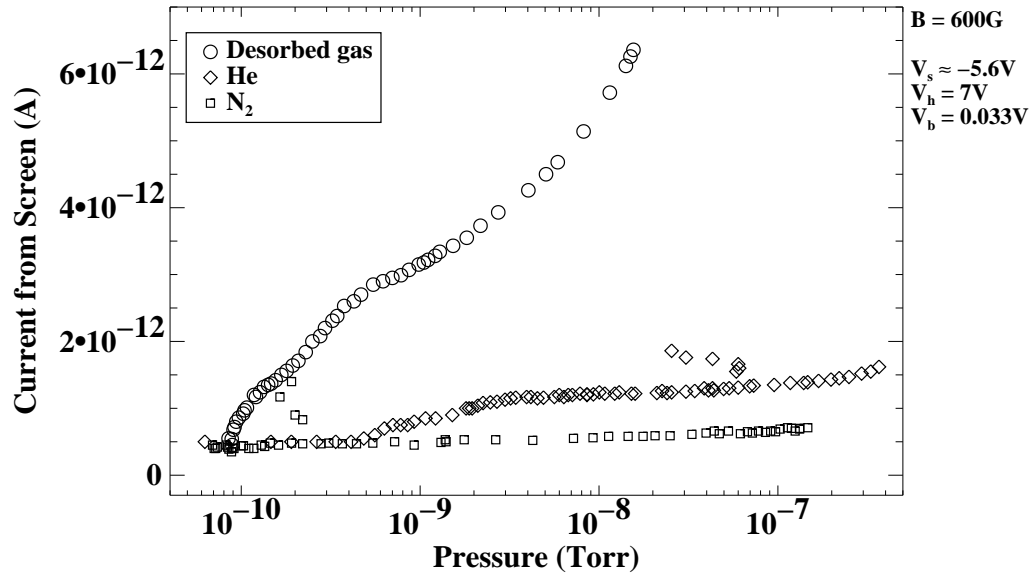


Figure 5.14: Ion current vs. background gas pressure for a variety of background gases. For this data, $B = 600 \text{ G}$, $V_h = 7 \text{ V}$, and $V_b = 0.033 \text{ V}$. The uncertainty in the current is smaller than the plot symbol for all data points. The filament bias voltage was set to $V_b \gtrsim 0$ because preliminary data suggested the ion emission was substantial at this setting.

7 (to which the copper acceleration grid for the phosphor screen is attached) to -5.6 V , and charging the phosphor screen to -5.3 V using a separate power supply. The current to the phosphor screen is measured using a Keithley 602A Electrometer in series with the phosphor screen's power supply.

The ion currents measured as a function of background gas pressure with this setup are shown in Fig. 5.14. In this plot, the pressure reported for the desorbed gas data is simply the pressure reading from the gauge (which is set to report the pressure for pure nitrogen gas), because we do not know the relative sensitivity of the gauge to the desorbed gas. The pressure for the helium data is corrected for the factor of five lower gauge sensitivity to helium than to nitrogen. The first

data set taken (the circles) is the current as a function of the desorbed gas pressure (created by letting the filament heat the trap, just as for Fig. 5.11). It took several hours for the pressure to rise to an extractor gauge reading of $P = 1.4 \times 10^{-8}$ Torr. The next data set, represented by the diamonds, was obtained by leaking helium gas into the trap. However, the six diamonds in this set that are distinct from the rest in the range of pressure readings 2×10^{-8} Torr $< P < 7 \times 10^{-8}$ Torr were taken immediately *after* the flow of helium gas to the trap was stopped at the reading $P \approx 4 \times 10^{-7}$, and should have been less than the ion current at that pressure.

This unusual behavior suggests that the ion current measured at the phosphor screen for $V_b > 0$ is not a function of the helium gas pressure but rather of some independent quantity, such as the partial pressure of the gas desorbed from the trap surfaces. This hypothesis was tested by instead leaking nitrogen gas into the trap, since nitrogen should be much more easily ionized than helium gas (the ionization gauges are 5 times more sensitive to nitrogen than helium, and are only 1.5 times more sensitive to argon than nitrogen). The nitrogen-gas data is represented by the squares in Fig. 5.14, and exhibits a similar behavior to the data obtained using helium; the ion current rises slowly for the entire time that nitrogen is leaked into the trap, and then continues to rise after the nitrogen leak is turned off (as demonstrated by the four squares above the helium data at a reading of $P \approx 2 \times 10^{-10}$ Torr). If the diocotron mode growth measured for the high-heating-voltage data is indeed due to the presence of transiting ions produced from the desorbed gas, it could explain why the mode growth rates stopped increasing in Fig. 5.12 after helium gas was introduced for pressure control—the quick changes in the partial pressure of helium would have little effect on the slow increases in the diocotron

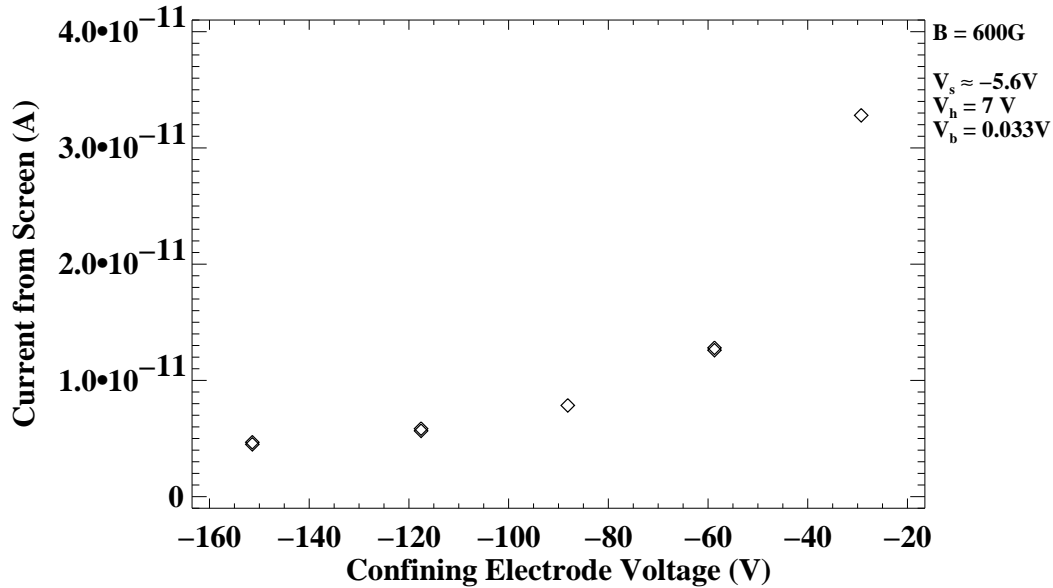


Figure 5.15: Ion current vs. confining voltage at a pressure reading of $P \approx 5.5 \times 10^{-9}$ Torr (of desorbed gas), $V_b = 0.033$, $V_h = 7$ V, and $B = 600$ G. The uncertainty in the current is smaller than the plot symbol for all data points.

mode growth rate, and the mode growth would appear to have saturated as the background gas pressure was increased with helium instead.

During the measurement of the ion current represented by the circles in Fig. 5.14, a quick set of measurements of the ion current as a function of the confining voltage on trap electrodes 1–6 revealed the dependence shown in Fig. 5.15. The current from the filament assembly is observed to increase with increasing confining voltage, suggesting that the confining electrode voltages are not important for extracting ions from the filament assembly at $V_b \approx 0$ V. This data also supports the hypothesis that transiting ions become trapped in the confining potential well formed by the charged electrodes 1–6, and that more ions are trapped and allowed to escape the trap radially to the confining electrodes [Kabantsev, 2003] as the confining

voltage is made more negative. This axial trapping and radial diffusion of ions provides another avenue of escape for the ions (in addition to the two grounded grids in EDG) when the phosphor screen is biased positively for plasma measurements.

At a reduced confining voltage, the greater ion current allows measurements of the ion current dependences on the filament bias and heating voltages, shown in Fig. 5.16. In addition, the confining voltage V_c may be applied to fewer trap electrodes to further reduce the number of ions trapped and lost radially, and only electrodes 1 and 7 were biased to their respective voltages for this data. In Figure 5.16(a), the current emitted by the filament assembly is displayed as a function of the filament heating voltage for $V_c = -14.7$ V, and a similar increase with heating voltage is observed as for the mode growth rate data in Figures 5.6 and 5.7. In Fig. 5.16(b), the ion current as a function of bias voltage measured at the lower confining voltage ($V_c = -43$ V, represented by the diamonds) has a similar dependence on bias voltage to the mode growth rate data for $V_b \gtrsim -12$ V in Figures 5.9 and 5.13, and the current measured at the higher confining voltage ($V_c = -150$ V, represented by the triangles) also mimics the behavior of the mode growth data at high bias voltages ($V_b \lesssim -30$ V).

The substantial ion current at the high bias voltages agrees with the most recent transiting ion mechanism description [KABANTSEV and DRISCOLL, 2003b], which postulates that ions are produced when electrons from the filament are accelerated towards the zero-voltage accelerating grid between the filament and the trap and ionize background gas molecules near the grid. This mechanism should not be responsible for the majority of ion current measurements presented in this section, those where $V_b > 0$ V, and an explanation for the source of ions at low bias voltages ($V_b > -25$ V) is still outstanding. The observations in Fig. 5.14 that suggest only

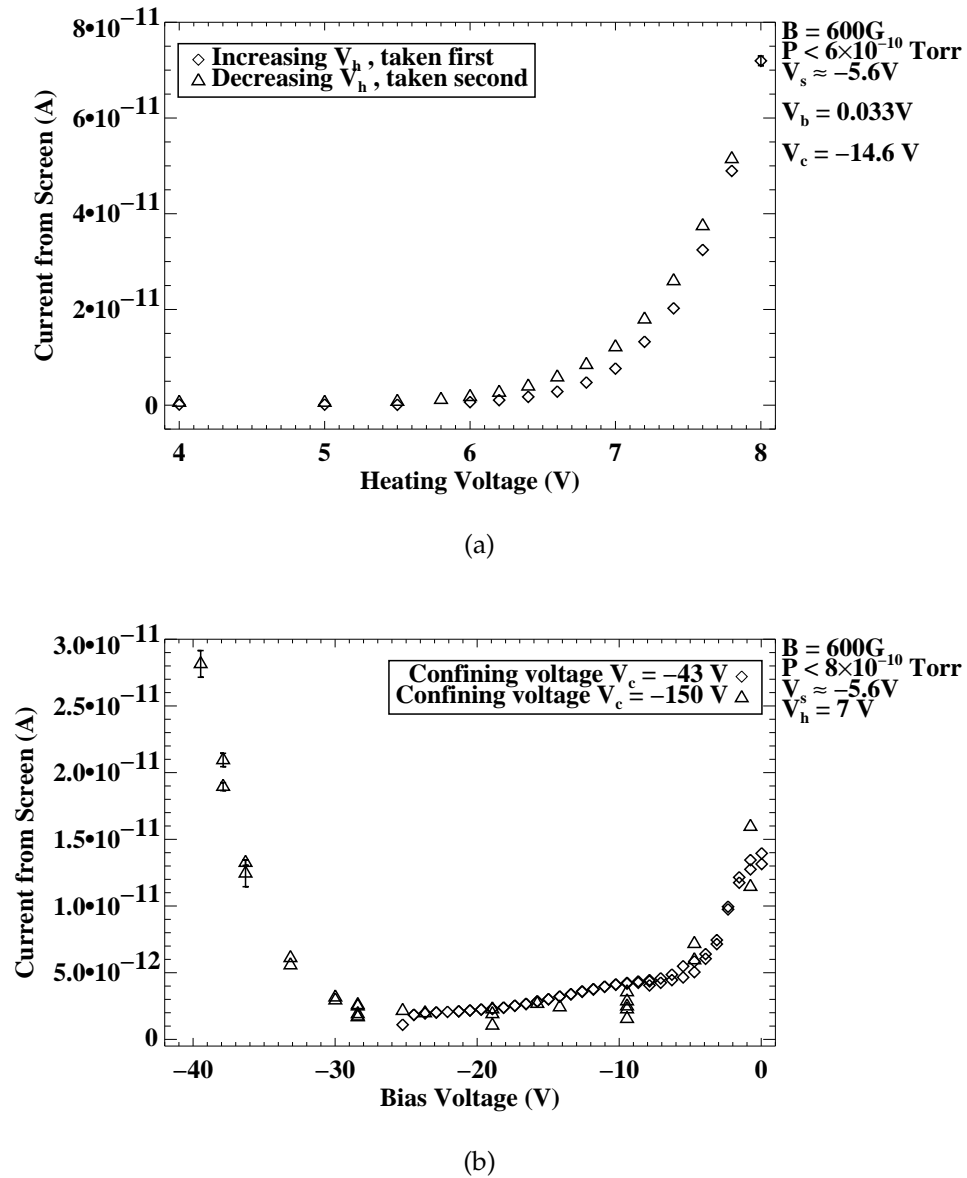


Figure 5.16: Ion current filament voltages. The uncertainty in the current is smaller than the plot symbol for all data points without error bars. For the data in Fig. 5.16(a), $B = 600$ G, $V_b = 0.033$ V, $P \approx 4 \times 10^{-10}$ Torr, and the confining voltage $V_c = -14.6$ V. For the data in Fig. 5.16(b), $B = 600$ G, $V_h = 7$ V, and $P \approx 6 \times 10^{-10}$ Torr.

desorbed gas is ionized were also taken at $V_b = 0.033$ V, and this may be an important clue for the identification of the mechanism. However, this desorbed-gas pressure dependence does not necessarily apply to mode growth and ion production at high bias voltages ($V_b < -30$ V), which might depend more sensitively on inserted helium or nitrogen gas because of the different ion production mechanism. The similitude between the ion current dependences and the mode growth rate dependences on filament voltages strongly suggests that undesired ions are responsible for the new mode growth at high filament heating voltages observed in EDG.

One additional difference between the description of transiting-ion-induced mode growth and the experiments presented here is that the transiting ions observed in the UCSD experiment were apparently trapped between the positively charged density diagnostic and the filament assembly. This was demonstrated by the observation of an immediate decrease of the mode growth rate when the density diagnostic was switched to a negative bias voltage [KABANTSEV and DRISCOLL, 2003b]. In test experiments on EDG, switching the phosphor screen voltage from $V_s = +30$ V to $V_s = -30$ V (between plasmas) had no effect on the growth rate of the diocotron mode, even though the number of ions collected by the screen is substantially less at $V_s = +30$ V (data not shown). If transiting ions are indeed the cause of the mode growth in EDG, they must only travel through the plasma a few times before they are lost to one of the zero-voltage grids (between the trap and the filament assembly or between the trap and the phosphor screen) or become deeply trapped in one of the confining potential wells for this test measurement to be consistent. In addition, there could be some complicated interaction between

the ions trapped in the confining potential wells and the plasma that accounts for the mode growth, but this possibility has not been explored.

5.5 Summary of $m = 1$ Diocotron Mode Measurements

The $m = 1$ diocotron mode in EDG was previously shown to have finite-length and large-amplitude frequency shifts similar to those seen in other Malmberg-Penning traps, and confirmed to grow in the presence of resistive trap electrodes. The plasma's displacement from the trap axis by the $m = 1$ mode has been verified using the new phosphor-screen diagnostic, and the presence of quick mode growth does not cause the plasma to expand measurably faster than it does when the mode is absent. The $m = 1$ mode was additionally observed in the previous study to experience an "anomalous" damping that could not be explained by the accepted "rotational pumping" mechanism, and the mode evolution was observed to be sensitive to $\Delta P \approx 5 \times 10^{-10}$ Torr changes in background gas pressure.

Subsequent measurements with small-filament plasmas presented in this chapter reveal that the $m = 1$ mode in the UHV pressure range where the plasma expansion is slowly varying is also quite sensitive to the electron-source filament's heating voltage, the filament's bias voltage, and the desorbed background gas partial pressure. The mode is observed to grow more strongly with increasing filament heating voltage, and to grow more strongly at low, negative filament bias voltages and high, negative filament bias voltages than at moderate filament bias voltages. Measurements of this mode growth as a function of background gas pressure show a remarkable sensitivity to pressure changes as small as $\Delta P \approx 3 \times 10^{-11}$ Torr (see

Fig. 5.12), at pressures below $P = 1 \times 10^{-9}$ Torr, but little sensitivity above that point.

Measurements of ions transiting the trap axially suggest that the ions are responsible for the clear diocotron mode growth in all of the new mode evolution measurements. In other devices [KABANTSEV and DRISCOLL, 2003b; PEURRUNG *et al.*, 1993], transiting ions generated in the filament assembly or the plasma (and confined between the filament assembly and the density diagnostic) were observed to destabilize the plasma to the $m = 1$ mode. The ion current generated by the EDG filament assembly depends very similarly on the filament heating voltage and bias voltage as the mode growth rate does, but measurements of the ion current as a function of background gas show that the ion current increases primarily with time rather than with helium gas pressure. The conclusion from the data is that the ion production for $V_b > 0$ V is not as sensitive to the helium or nitrogen gas pressures as it is to the partial pressure of the gas desorbed from the trap surfaces, suggesting that the desorbed gas is ionized much more effectively near the filament than either helium or nitrogen. At high bias voltages ($V_b < 30$ V), where the ions are thought to be created by electron impact near the grounded filament grid as in the other devices, the ion production and therefore the mode growth are expected to be sensitive to helium and nitrogen partial pressures.

The ion current measurements at high, negative filament bias voltages agree with the proposed ion-production mechanism of energetic electrons ionizing the background gas near the acceleration grid, but the source of the ions at low, negative bias voltages is not explained. Determining the mechanism for ion generation at low filament bias voltages or a clear way of isolating the plasma from the ions

may be necessary to predict the $m = 1$ diocotron mode behavior as a function of background gas pressure in EDG.

Chapter 6

Conclusions

The new measurements of the EDG plasma expansion and $m = 1$ diocotron mode evolution presented in this thesis have greatly illuminated the understanding of the dynamics observed previously in EDG. Better agreement with theoretical predictions and the experimental findings of other groups have lent credibility to the experimental results on EDG, and helped reveal the remaining challenges to our understanding of the effects that neutral gas molecules have on trapped electron plasmas. New temperature and density diagnostics constructed for this purpose were critical to the advances made in this research.

6.1 Dependence of the Plasma Expansion Rate on Background Gas Pressure

The previous measurements of the plasma expansion rates as a function of helium gas pressure made with the Faraday-cup density diagnostic have been extended to pressures above $P = 1 \times 10^{-8}$ Torr. The expansion rate predicted with

a fluid description of the plasma [DAVIDSON and MOORE, 1996] was shown to match the new expansion rate data in the pressure range where the minimum level of plasma expansion was negligible. That minimum level of expansion, in turn, was shown to be artificially high with the newly implemented phosphor-screen density diagnostic by measuring the density profile evolution at much later times. The extended density profile evolutions strongly suggest that the initial evolution of the plasma at low pressures is a nonlinear relaxation of the plasma to thermal quasi-equilibrium, a conclusion supported by new measurements of the plasma temperature evolution at $r = 0$. The expansion after the plasma has relaxed to thermal quasi-equilibrium reveals a much lower level of asymmetry-induced transport in EDG than was previously thought to exist. The agreement between the theoretically predicted expansion rate derived for plasmas with a spatially-uniform temperature and the measured rates for plasmas at higher pressures that are expected to have temperature gradients is rather remarkable. It suggests that whatever mechanism is responsible for the apparent loss of plasma kinetic energy may also be suppressing the creation of temperature gradients, that the gradients that exist may be too small to have a measurable effect on the plasma expansion, or that including temperature gradients in the fluid theory would not change the prediction appreciably.

The finding that the plasmas measured with the Faraday-cup density diagnostic were not in thermal quasi-equilibrium indicates that the temperatures inferred from those density profiles by fitting them with theoretical, thermal quasi-equilibrium density profiles are not necessarily representative of the plasma temperature once it reaches quasi-equilibrium. The previous energy analysis, which

predicted a loss of energy through inelastic collisions with background gas impurities based on these inferred temperatures, is therefore not trustworthy. However, the newly measured plasma temperatures, observed after the plasma has relaxed to thermal quasi-equilibrium in the asymmetry-induced expansion regime, also do not increase as the plasma expands, suggesting that the electrostatic potential energy liberated as the plasma expands is indeed being lost in part through inelastic collisions, as suggested previously, and possibly through work done in interactions with the asymmetric fields in the trap. To determine the fate of the liberated electrostatic potential energy, it would therefore be necessary to determine the constitution of the background gas in the trap using a Residual Gas Analyzer.

It was also found that the plasma temperature measurements disagree with the temperatures inferred from the density profiles, even for the plasmas thought to be in thermal quasi-equilibrium. It is not clear whether this is due to errors in the analysis codes, is a systematic failure of the new diagnostics to accurately measure the density profiles or temperatures, or is simply a further indication that the plasma is still not in thermal quasi-equilibrium even late in the evolution. To clearly resolve whether the plasma is in thermal quasi-equilibrium, a temperature diagnostic that can measure off-axis temperatures should be implemented to see whether the plasma relaxes to a constant temperature throughout.

To improve the characterization of the plasma expansion as a function of background gas pressure in future measurements, there are at least two clear options available: At the higher background gas pressures, where the plasma currently expands too quickly to relax to thermal quasi-equilibrium, an additional, rotating-wall-type electric field might be employed to confine the plasma long enough that it fully equilibrates before measurements are made. Even with an initially thermal,

quasi-equilibrium state, a temperature diagnostic that can measure off-axis temperatures would be necessary to fully describe the dynamics at high pressures. At the lower pressures, the asymmetries in the trap fields could be reduced to allow expansion rate measurements where the plasmas have time to equilibrate before they come into contact with the trap electrodes. At these pressures, a Residual Gas Analyzer would still be needed to ensure that minority gas molecules do not interfere excessively with the plasma dynamics.

6.2 Dependence of the $m=1$ Diocotron Mode Growth Rate on Background Gas Pressure

The $m = 1$ diocotron mode frequency shifts and instability to resistive trap electrodes that were seen in other traps were confirmed previously for EDG plasmas, and an “anomalous” damping and slight pressure dependence of the mode damping were also observed. In this thesis work, the evolution of the $m = 1$ diocotron mode was measured for plasmas with smaller initial radii, and the observed mode *growth* was found to be quite sensitive to the filament voltages and the background gas pressure. For example, changes in the mode growth rate for pressure differences as low as $\Delta P \approx 3 \times 10^{-11}$ Torr (N_2 -equivalent) were observed using gas desorbed from the trap surfaces to change the pressure. Measurements of the flow of ions from the filament assembly suggest that ions are present in the trap at high filament heating voltages, and that they are primarily formed from the unknown gas molecules desorbed from the inner surfaces of the EDG device as it is heated by the filament [for low filament bias voltages ($V_b > -25\text{V}$)]. Furthermore, the ion production as a function of filament heating voltage and filament

6.2. Dependence of the $m=1$ Diocotron Mode Growth Rate on Background Gas Pressure¹⁷³

bias voltage has a dependence that is very similar to the mode growth dependence on those parameters, strongly suggesting that transiting ions are responsible for the mode growth. Similar mode growth due to transient and transiting ions has been observed and characterized by other groups [KABANTSEV and DRISCOLL, 2003b; PEURRUNG *et al.*, 1993], as well.

To more definitively link the mode growth at high filament heating voltages to the production of ions, an additional, positively charged trap electrode or grid between the first confining cylinder and the filament assembly could be introduced. Alternatively, the bias voltages on the filament or the phosphor screen could be more quickly varied to see the effects on the mode growth. If ions are clearly shown to be responsible, an RGA could be used to identify the desorbed gas that is preferentially ionized and steps should be taken to either ensure that all gases are ionized fairly well by the trap (creating, in effect, a highly sensitive ionization gauge) or to eliminate the ionization (e.g., using a field-emitting array as the electron source, which would require hardly any heating) to provide ion-free mode dynamics.

The measurements made previously of the mode damping as a function of background pressure in large-filament plasmas have not been reproduced with the smaller filament plasmas. It is interesting to consider whether the plasma expansion is somehow responsible for the mode damping (which could be tested by intentionally misaligning the magnetic field) or whether some unobserved interaction between the plasma and the trap electrodes caused the damping (which might require replacement of the large filament to properly diagnose). Using the new phosphor-screen diagnostic to observe small-filament plasmas, mode damping at later times has always corresponded to the close proximity between the trap electrodes and the edge of the plasma, usually with a small, accompanying loss

6.2. Dependence of the $m=1$ Diocotron Mode Growth Rate on Background Gas Pressure¹⁷⁴

in plasma charge. Although measurements of the effects that plasma expansion has on the mode evolution directly have not been yet been performed, preliminary measurements suggest that modes driven with a resistive trap electrode do not cause the plasma to expand more quickly than it does in the absence of the mode.

Appendix A

Electron-neutral collision and ionization cross-sections¹

In this appendix is reproduced several calculations [CHAO, 1999] of the “volumetric collision rate” and “volumetric ionization rate” for some of the gases present in the EDG vacuum chamber. The “volumetric collision rate”

$$\langle \sigma v \rangle = \int_0^\infty dv \sigma_m v P(v), \quad (\text{A.1})$$

which is important for plasma expansion rate predictions, was calculated for an electron plasma with an isotropic, Maxwellian particle speed distribution [KITTEL and KROEMER, 1980]

$$P(v) = 4\pi \left(\frac{m_e}{2\pi T} \right)^{3/2} v^2 \exp \left(-\frac{m_e v^2}{2T} \right). \quad (\text{A.2})$$

In Eq. (A.1), the momentum-transfer collision cross section between electrons and molecules is defined by

$$\sigma_m(E) = \int d\phi \int d\theta (1 - \cos \theta) \frac{d\sigma}{d\Omega}(E, \theta, \phi) \quad (\text{A.3})$$

¹This Appendix draws its material entirely from Appendix B of reference [CHAO, 1999].

where

$$\frac{d\sigma}{d\Omega}(E, \theta, \phi) \tag{A.4}$$

is the differential scattering cross section, E is the energy of the electron, and θ and ϕ denote the spherical-coordinate angles into which the electron scatters, and is given in the literature [HAYASHI, 1981]. The “volumetric ionization rate” was similarly calculated, using the ionization cross sections given in the literature [RAPP and ENGLANDER-GOLDEN, 1965].

A.1 Helium

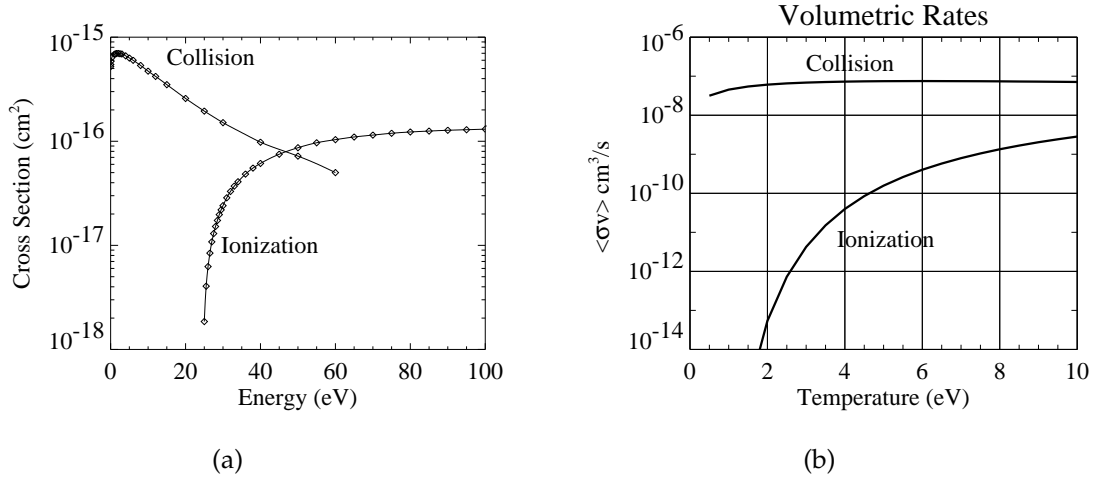


Figure A.1: Electron - He momentum transfer collision and ionization (a) cross-sections and (b) volumetric rates.

Temp. (eV)	Collision Rate (cm ³ /s)	Ionization Rate (cm ³ /s)
0.5	3.17×10^{-8}	
1.0	4.54×10^{-8}	1.56×10^{-19}
1.5	5.44×10^{-8}	7.42×10^{-16}
2.0	6.08×10^{-8}	5.40×10^{-14}
3.0	6.87×10^{-8}	4.24×10^{-12}
4.0	7.27×10^{-8}	3.97×10^{-11}
5.0	7.45×10^{-8}	1.57×10^{-10}
6.0	7.50×10^{-8}	4.01×10^{-10}
7.0	7.47×10^{-8}	7.96×10^{-10}
8.0	7.38×10^{-8}	1.34×10^{-9}
9.0	7.26×10^{-8}	2.03×10^{-9}
10.	7.12×10^{-8}	2.84×10^{-9}

Table A.1: Volumetric collision and ionization rates for electrons impacting helium (He).

A.2 Molecular Hydrogen

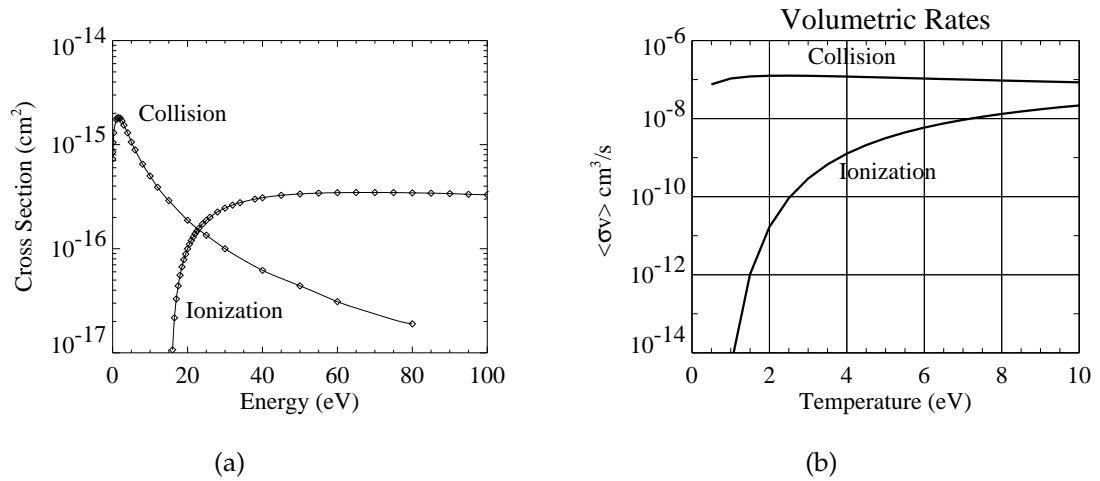
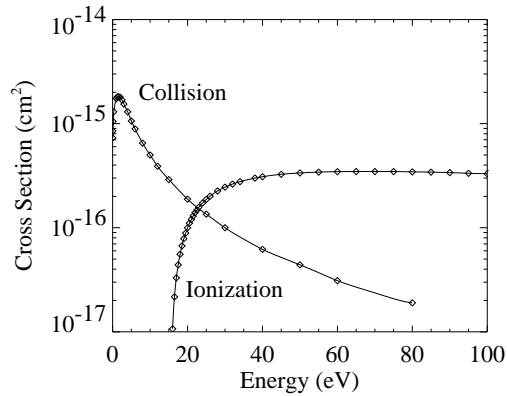


Figure A.2: Electron - H₂ momentum transfer collision and ionization (a) cross-sections and (b) volumetric rates.

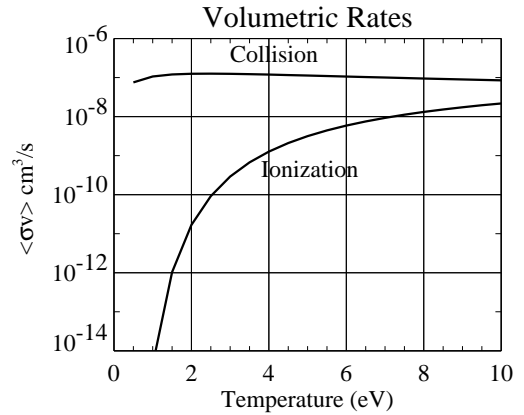
Temp. (eV)	Collision Rate (cm ³ /s)	Ionization Rate (cm ³ /s)
0.5	7.53×10^{-8}	4.36×10^{-22}
1.0	1.07×10^{-7}	4.38×10^{-15}
1.5	1.20×10^{-7}	1.04×10^{-12}
2.0	1.25×10^{-7}	1.68×10^{-11}
3.0	1.25×10^{-7}	2.91×10^{-10}
4.0	1.19×10^{-7}	1.27×10^{-9}
5.0	1.13×10^{-7}	3.16×10^{-9}
6.0	1.06×10^{-7}	5.89×10^{-9}
7.0	1.00×10^{-7}	9.30×10^{-9}
8.0	9.48×10^{-8}	1.32×10^{-8}
9.0	8.97×10^{-8}	1.74×10^{-8}
10.	8.50×10^{-8}	2.18×10^{-8}

Table A.2: Volumetric collision and ionization rates for electrons impacting molecular hydrogen (H₂).

A.3 Molecular Nitrogen



(a)



(b)

Figure A.3: Electron - N_2 momentum transfer collision and ionization (a) cross-sections and (b) volumetric rates.

Temp. (eV)	Collision Rate (cm^3/s)	Ionization Rate (cm^3/s)
0.5	5.15×10^{-8}	3.37×10^{-22}
1.0	8.58×10^{-8}	3.62×10^{-15}
1.5	1.06×10^{-7}	9.20×10^{-13}
2.0	1.18×10^{-7}	1.59×10^{-11}
3.0	1.34×10^{-7}	3.08×10^{-10}
4.0	1.45×10^{-7}	1.47×10^{-9}
5.0	1.53×10^{-7}	3.94×10^{-9}
6.0	1.60×10^{-7}	7.82×10^{-9}
7.0	1.64×10^{-7}	1.30×10^{-8}
8.0	1.68×10^{-7}	1.93×10^{-8}
9.0	1.71×10^{-7}	2.65×10^{-8}
10.	1.72×10^{-7}	3.44×10^{-8}

Table A.3: Volumetric collision and ionization rates for electrons impacting molecular nitrogen (N_2).

Bibliography

AMORETTI, M., AMSLER, C., BONOMI, G., BOUCHTA, A., BOWE, P., CARRARO, C., CESAR, C. L., CHARLTON, M., COLLIER, M. J. T., DOSER, M., FILIPPINI, V., FINE, K. S., FONTANA, A., FUJIWARA, M. C., FUNAKOSHI, R., GENOVA, P., HANGST, J. S., HAYANO, R. S., HOLZSCHEITER, M. H., JØRGENSEN, L. V., LAGOMARSINO, V., LANDUA, R., LINDELÖF, D., RIZZINI, E. L., MACRÍ, M., MADSEN, N., MANUZIO, G., MARCHESOTTI, M., MONTAGNA, P., PRUYS, H., REGENFUS, C., RIEDLER, P., ROCHET, J., ROTONDI, A., ROULEAU, G., TESTERA, G., VARIOLA, A., WATSON, T. L., and VAN DER WERF, D. P. (2002). Production and detection of cold antihydrogen atoms. *Nature* **419**, 456–459.

AMORETTI, M., BONOMI, G., BOUCHTA, A., BOWE, P. D., CARRARO, C., CESAR, C. L., CHARLTON, M., DOSER, M., FONTANA, A., FUJIWARA, M. C., FUNAKOSHI, R., GENOVA, P., HANGST, J. S., HAYANO, R. S., JØRGENSEN, L. V., LAGOMARSINO, V., LANDUA, R., RIZZINI, E. L., MACRÍ, M., MADSEN, N., MANUZIO, G., TESTERA, G., VARIOLA, A., and VAN DER WERF, D. P. (2003a). Complete nondestructive diagnostic of nonneutral plasmas based on the detection of electrostatic modes. *Phys. Plasmas* **10**, 3056–3064.

AMORETTI, M., BONOMI, G., BOUCHTA, A., BOWE, P. D., CARRARO, C., CESAR, C. L., CHARLTON, M., DOSER, M., FONTANA, A., FUJIWARA, M. C.,

- FUNAKOSHI, R., GENOVA, P., HANGST, J. S., HAYANO, R. S., JØRGENSEN, L. V., LAGOMARSINO, V., LANDUA, R., RIZZINI, E. L., MACRÍ, M., MADSEN, N., MANUZIO, G., TESTERA, G., VARIOLA, A., and VAN DER WERF (ATHENA COLLABORATION), D. P. (2003b). Complete nondestructive diagnostic of nonneutral plasmas based on the detection of electrostatic modes. *Phys. Plasmas* **10**, 3056–3064.
- ANDEREGG, F., DRISCOLL, C. F., and DUBIN, D. H. E. (2002a). Shear-Limited Test Particle Diffusion in 2-Dimensional Plasmas. In ANDEREGG, F., SCHWEIKHARD, L., and DRISCOLL, C. F., editors, *Non-Neutral Plasma Physics IV: Workshop on Non-Neutral Plasmas: AIP Conference Proceedings, Volume 606*, page 401, Melville, NY. American Institute of Physics.
- ANDEREGG, F., HOLLMANN, E. M., and DRISCOLL, C. F. (1998). Rotating field confinement of pure electron plasmas using Trivelpiece-Gould modes. *Phys. Rev. Lett.* **81**, 4875–4878.
- ANDEREGG, F., HUANG, X.-P., DRISCOLL, C. F., HOLLMANN, E. M., O'NEIL, T. M., and DUBIN, D. H. E. (1997a). Test Particle Transport due to Long Range Interactions. *Phys. Rev. Lett.* **78**, 2128–2131.
- ANDEREGG, F., HUANG, X.-P., HOLLMANN, E. M., DRISCOLL, C. F., O'NEIL, T. M., and DUBIN, D. H. E. (1997b). Test particle transport from long-range collisions. *Phys. Plasmas* **4**, 1552–1558.
- ANDEREGG, F., SCHWEIKHARD, L., and DRISCOLL, C. F., editors (2002b). *Non-Neutral Plasma Physics IV*, volume 606 of *AIP Conference Proceedings*. American Institute of Physics, Melville, NY.

- ANDEREGG, F., SHIGA, N., DUBIN, D. H. E., DRISCOLL, C. F., and GOULD, R. W. (2003). Thermally excited Trivelpiece-Gould modes as a pure electron plasma temperature diagnostic. *Phys. Plasmas* **10**, 1556–1562.
- BECK, B. R., FAJANS, J., and MALMBERG, J. H. (1996). Temperature and anisotropic-temperature relaxation measurements in cold, pure-electron plasmas. *Phys. Plasmas* **3**, 1250–1258.
- BEVINGTON, P. R. and ROBINSON, D. K. (1992). *Data reduction and error analysis for the physical sciences*. McGraw-Hill, Inc., New York, 2nd edition.
- BOLLINGER, J. J., KRIESEL, J. M., MITCHELL, T. B., KING, L. B., JENSEN, M. J., ITANO, W. M., and DUBIN, D. H. E. (2003). Laser-cooled ion plasmas in Penning traps. *J. Phys. B* **36**, 499–510.
- BOLLINGER, J. J., PRESTAGE, J. D., ITANO, W. M., and WINELAND, D. J. (1985). Laser-Cooled Atomic Frequency Standard. *Phys. Rev. Lett.* **54**, 1000–1003.
- BOLLINGER, J. J., SPENCER, R. L., and DAVIDSON, R. C., editors (1999). *Non-Neutral Plasma Physics III*, volume 498 of *AIP Conference Proceedings*. American Institute of Physics, Melville, NY.
- BOLLINGER, J. J., WINELAND, D. J., and DUBIN, D. H. E. (1994). Nonneutral Ion Plasmas and Crystals, Laser Cooling, and Atomic Clocks. *Phys. Plasmas* **1**, 1403–1414.
- BONANOS, P. (1964). Coil Data Compilation. Atomic Energy Commission Research and Development Report TM-207, Plasma Physics Laboratory, Princeton University.

- CHAO, E. H. (1999). *Pure Electron Plasma Dynamics and the Effects of Collision with Background Neutral Gas Atoms*. PhD thesis, Princeton University.
- CHAO, E. H., DAVIDSON, R. C., PAUL, S. F., and FINE, K. S. (1999a). Self-Consistent Numerical Solution to Poisson's Equation in an Axisymmetric Malmberg-Penning Trap. In BOLLINGER, J., DAVIDSON, R. C., and SPENCER, R., editors, *Proceedings of the 1999 Workshop on Nonneutral Plasmas: AIP Conference Proceedings 498*, pages 461–468, Melville, NY. American Institute of Physics.
- CHAO, E. H., DAVIDSON, R. C., PAUL, S. F., and MORRISON, K. A. (1999b). Effects of Background Gas Pressure on Pure Electron Plasma Dynamics in the Electron Diffusion Gauge Experiment. In BOLLINGER, J., DAVIDSON, R. C., and SPENCER, R., editors, *Proceedings of the 1999 Workshop on Nonneutral Plasmas: AIP Conference Proceedings 498*, pages 278–289, Melville, NY. American Institute of Physics.
- CHAO, E. H., DAVIDSON, R. C., PAUL, S. F., and MORRISON, K. A. (2000). Effects of background gas pressure on the dynamics of a nonneutral electron plasma confined in a Malmberg-Penning trap. *Phys. Plasmas* **7**, 831–838.
- CHAO, E. H., PAUL, S. F., and DAVIDSON, R. C. (1999c). Dynamics of the $m=1$ Diocotron Mode in the Electron Diffusion Gauge (EDG) Experiment. *J. Vac. Sci. Technol. A* **17**, 2034–2040.
- CLUGGISH, B. P. (1995). *Experiments on Asymmetry-Induced Particle Transport in Magnetized, Pure Electron Plasma Columns*. PhD thesis, University of California, San Diego.

- CLUGGISH, B. P. and DRISCOLL, C. F. (1995). Transport and Damping from Rotation Pumping in Magnetized Electron Plasmas. *Phys. Rev. Lett.* **74**, 4213–4216.
- CLUGGISH, B. P. and DRISCOLL, C. F. (1996). Transport and sawtooth oscillations from rotational pumping of a magnetized electron plasma. *Phys. Plasmas* **3**, 1813–1819.
- CORNGOLD, N. R. (1996). The nonlinear diocotron mode in a pure electron plasma. *Phys. Plasmas* **3**, 3324–3330.
- CROOKS, S. M. and O'NEIL, T. M. (1995). Rotational pumping and damping of the $m=1$ diocotron mode. *Phys. Plasmas* **2**, 355–364.
- DAVIDSON, R. C. (1990). *The Physics of Nonneutral Plasmas*. Addison-Wesley, California.
- DAVIDSON, R. C. and CHAO, E. H. (1996a). Electrostatic instability for azimuthal mode number $l = 1$ induced by electron-neutral collisions in a strongly-magnetized nonneutral electron plasma. *Phys. Lett. A* **219**, 95–101.
- DAVIDSON, R. C. and CHAO, E. H. (1996b). $l = 1$ electrostatic instability induced by electron-neutral collisions in a nonneutral electron plasma interacting with background neutral gas. *Phys. Plasmas* **3**, 3279–3287.
- DAVIDSON, R. C. and KRALL, N. A. (1969). Vlasov Description of an Electron Gas in a Magnetic Field. *Phys. Rev. Lett.* **22**, 833–837.
- DAVIDSON, R. C. and KRALL, N. A. (1970). Vlasov equilibria and stability of an electron gas. *Phys. Fluids* **13**, 1543–1555.

- DAVIDSON, R. C. and LUND, S. M. (1994). Thermal Equilibrium Properties of Nonneutral Plasma in the Weak Coupling Approximation. In FISCH, N. J., editor, *Advances in Plasma Physics: Thomas H. Stix Symposium; AIP Conference Proceedings 314*, pages 1–15, Melville, NY. American Institute of Physics.
- DAVIDSON, R. C. and MOORE, D. A. (1996). Expansion and nonlinear relaxation of a strongly magnetized non-neutral electron plasma due to elastic collisions with background neutral gas. *Phys. Plasmas* **3**, 218–225.
- DAVIDSON, R. C. and UHM, H. (1977). Influence of Strong Self-Electric Fields on the Ion Resonance Instability in a Nonneutral Plasma Column. *Phys. Fluids* **20**, 1938–1946.
- DAVIDSON, R. C. and UHM, H. (1978). Influence of Finite Ion Larmor Radius Effects on the Ion Resonance Instability in a Nonneutral Plasma Column. *Phys. Fluids* **21**, 60–71.
- DEGRASSIE, J. S. and MALMBERG, J. H. (1977). Wave-Induced Transport in the Pure Electron Plasma. *Phys. Rev. Lett.* **39**, 1077–1080.
- DEGRASSIE, J. S. and MALMBERG, J. H. (1980). Waves and transport in the pure electron plasma. *Phys. Fluids* **23**, 63–81.
- DOUGLAS, M. H. and O'NEIL, T. M. (1978). Transport of a nonneutral electron plasma due to electron collisions with neutral atoms. *Phys. Fluids* **21**, 920–925.
- DRISCOLL, C. F. (1990). Observation of an Unstable $l = 1$ Diocotron Mode on a Hollow Electron Column. *Phys. Rev. Lett.* **64**, 645–648.

- DRISCOLL, C. F., ANDEREGG, F., DUBIN, D. H. E., JIN, D. Z., KRIESEL, J. M., HOLLMANN, E. M., and O'NEIL, T. M. (2002). Shear reduction of collisional transport: Experiments and theory. *Phys. Plasmas* **9**, 1905–1914.
- DRISCOLL, C. F. and FINE, K. S. (1990). Experiments on vortex dynamics in pure electron plasmas. *Phys. Fluids B* **2**, 1359–1366.
- DRISCOLL, C. F., FINE, K. S., and MALMBERG, J. H. (1986). Reduction of Radial Losses in a Pure Electron Plasma. *Phys. Fluids* **29**, 2015–2017.
- DRISCOLL, C. F., MALMBERG, J. H., and FINE, K. S. (1988). Observation of Transport to Thermal Equilibrium in Pure Electron Plasmas. *Phys. Rev. Lett.* **60**, 1290–1293.
- DUBIN, D. H. E. (1997). Test Particle Diffusion and Failure of Integration along Unperturbed Orbits. *Phys. Rev. Lett.* **79**, 2678–2681.
- DUBIN, D. H. E. (1998). Collisional transport in non-neutral plasmas. *Phys. Plasmas* **5**, 1688–1694.
- DUBIN, D. H. E. and JIN, D. Z. (2001). Collisional diffusion in a 2-dimensional point vortex gas. *Phys. Lett. A* **284**, 112–117.
- DUBIN, D. H. E. and O'NEIL, T. M. (1997). Cross-Magnetic-Field Heat Conduction in Non-neutral Plasmas. *Phys. Rev. Lett.* **78**, 3868–3871.
- DUBIN, D. H. E. and O'NEIL, T. M. (1998). Two-dimensional bounce-averaged collisional particle transport in a single species non-neutral plasma. *Phys. Plasmas* **5**, 1305–1314.

- EGGLESTON, D. L. (1997). Confinement of test particles in a Malmberg-Penning trap with a biased axial wire. *Phys. Plasmas* **4**, 1196–1200.
- EGGLESTON, D. L. and CARRILLO, B. (2002). Amplitude scaling of asymmetry-induced transport in a non-neutral plasma trap. *Phys. Plasmas* **9**, 786–790.
- EGGLESTON, D. L. and CARRILLO, B. (2003). Frequency dependence of asymmetry-induced transport in a non-neutral plasma trap. *Phys. Plasmas* **10**, 1308–1314.
- EGGLESTON, D. L., DRISCOLL, C. F., BECK, B. R., HYATT, A. W., and MALMBERG, J. H. (1992). Parallel energy analyzer for pure electron plasma devices. *Phys. Fluids B* **4**, 3432–3439.
- EGGLESTON, D. L. and O'NEIL, T. M. (1999). Theory of asymmetry-induced transport in a non-neutral plasma. *Phys. Plasmas* **6**, 2699–2704.
- FAJANS, J. (1993). Transient ion resonance instability. *Phys. Fluids B* **5**, 3127–3135.
- FAJANS, J. and DUBIN, D. H. E., editors (1995). *Non-Neutral Plasma Physics II*, volume 331 of *AIP Conference Proceedings*. American Institute of Physics, New York.
- FAJANS, J., GILSON, E., and BACKHAUS, E. Y. (2000). Bifurcations in elliptical, asymmetric non-neutral plasmas. *Phys. Plasmas* **7**, 3929–3933.
- FINE, K. S. (1988). *Experiments with the $l = 1$ Diocotron Mode*. PhD thesis, University of California, San Diego.
- FINE, K. S. (1992). Simple theory of a nonlinear diocotron mode. *Phys. Fluids B* **4**, 3981–3984.

- FINE, K. S., CASS, A. C., FLYNN, W. G., and DRISCOLL, C. F. (1995). Relaxation of 2D Turbulence to Vortex Crystals. *Phys. Rev. Lett.* **75**, 3277–3280.
- FINE, K. S. and DRISCOLL, C. F. (1998). The finite length diocotron mode. *Phys. Fluids* **5**, 601–607.
- FINE, K. S., DRISCOLL, C. F., and MALMBERG, J. H. (1989). Measurements of a nonlinear diocotron mode in pure electron plasmas. *Phys. Rev. Lett.* **63**, 2232–2235.
- FISK, P. T. H. (1997). Trapped-Ion and Trapped-Atom Microwave Frequency Standards. *Rep. Prog. Phys.* **60**, 761–817.
- FUJIWARA, M. C., AMORETTI, M., AMSLER, C., BENDISCIOLI, G., BONOMI, G., BOUCHTA, A., BOWE, P., CARRARO, C., CHARLTON, M., COLLIER, M., DOSER, M., FILIPPINI, V., FINE, K., FONTANA, A., FUNAKOSHI, R., GENOVA, P., GRÖGLER, D., HANGST, J. S., HAYANO, R. S., HIGAKI, H., HOLZSCHEITER, M. H., JOFFRAIN, W., JØRGENSEN, L., LAGOMARSINO, V., LANDUA, R., CESSAR, C. L., LINDELÖF, D., LODI-RIZZINI, E., MADSEN, M. M. N., MANUZIO, G., MARCHESOTTI, M., MONTAGNA, P., PRUYS, H., REGENFUS, C., RIEDLER, P., ROTONDI, A., ROULEAU, G., SALVINI, P., TESTERA, G., VAN DER WERF, D. P., VARIOLA, A., VENTURELLI, L., WATSON, T., YAMAZAKI, T., and YAMAZAKI, Y. (2001). Producing Slow Antihydrogen for a Test of CPT Symmetry with ATHENA. *Hyperfine Interact.* **138**, 153–158.
- GABRIELSE, G., BOWDEN, N. S., OXLEY, P., SPECK, A., STORRY, C. H., TAN, J. N., WESSELS, M., GRZONKA, D., OELERT, W., SCHEPERS, G., SEFZICK, T., WALZ,

- J., PITTNER, H., HANSCH, T. W., and HESSELS, E. A. (2002). Driven Production of Cold Antihydrogen and the First Measured Distribution of Antihydrogen States. *Phys. Rev. Lett.* **89**, 233401.
- GILSON, E. (2001). *Quadrupole induced resonant particle transport in a pure electron plasma*. PhD thesis, University of California, Berkeley.
- GOULD, R. W. (1995). Dynamics of Nonneutral Plasmas. *Phys. Plasmas* **2**, 2151–2163.
- GREAVES, R. G., GILBERT, S. J., and SURKO, C. M. (2002). Trap-based positron beams. *Appl. Surf. Sci.* **194**, 56–60.
- GREAVES, R. G. and SURKO, C. M. (2002). Positron trapping and the creation of high-quality trap-based positron beams. *Nucl. Instrum. Meth. B* **192**, 90–96.
- HAYASHI, M. (1981). Recommended Values of Transport Cross Sections for Elastic Collisions and Total Collision Cross Section for Electrons in Atomic and Molecular Gases. Technical Report IPPJ-AM-19, Nagoya Inst. of Technology.
- HILSABECK, T. J., KABANTSEV, A. A., DRISCOLL, C. F., and O'NEIL, T. M. (2003). Damping of the Trapped-Particle Diocotron Mode. *Phys. Rev. Lett.* **90**, 245002.
- HOLLMANN, E. M., ANDEREGG, F., and DRISCOLL, C. F. (2000a). Confinement and manipulation of non-neutral plasmas using rotating wall electric fields. *Phys. Plasmas* **7**, 2776–2789.
- HOLLMANN, E. M., ANDEREGG, F., and DRISCOLL, C. F. (2000b). Measurement of cross-magnetic-field heat transport due to long-range collisions. *Phys. Plasmas* **7**, 1767–1773.

- HUANG, X.-P., ANDEREGG, F., HOLLMANN, E. M., DRISCOLL, C. F., and O'NEIL, T. M. (1997). Steady-State Confinement of Non-neutral Plasmas by Rotating Electric Fields. *Phys. Rev. Lett.* **78**, 875–878.
- HUANG, X.-P., FINE, K. S., and DRISCOLL, C. F. (1995). Coherent Vorticity Holes from 2D Turbulence Decaying in a Background Shear Flow. *Phys. Rev. Lett.* **74**, 4424–4427.
- HYATT, A. W. (1988). *Measurement of the Anisotropic Temperature Relaxation Rate in a Magnetized Pure Electron Plasma*. PhD thesis, University of California, San Diego.
- HYATT, A. W., DRISCOLL, C. F., and MALMBERG, J. H. (1987). Measurement of the Anisotropic Temperature Relaxation Rate in Pure Electron Plasma. *Phys. Rev. Lett.* **59**, 2975–2978.
- ICHIMARU, S. and ROSENBLUTH, M. N. (1970). Relaxation processes in plasmas with magnetic field. Temperature relaxations. *Phys. Fluids* **13**, 2778.
- JENKINS, T. G., MORRISON, K. A., DAVIDSON, R. C., and PAUL, S. F. (2002). Large Amplitude $m = 1$ Diocotron Mode Measurements in the Electron Diffusion Gauge Experiment. In ANDEREGG, F., SCHWEIKHARD, L., and DRISCOLL, C. F., editors, *Non-Neutral Plasma Physics IV: Workshop on Non-Neutral Plasmas: AIP Conference Proceedings, Volume 606*, pages 298–304, Melville, NY. American Institute of Physics.
- JONES, H. and LANGMUIR, I. (1927). The Characteristics of Tungsten Filaments as Functions of Temperature. *General Electric Review* **30**, 408.
- Kabantsev (2003). This mechanism was noted by Dr. Andrey A. Kabantsev to Dr. Stephen F. Paul at the APS-DPP03 meeting.

- KABANTSEV, A. A. and DRISCOLL, C. F. (2003a). Diagnosing the velocity-space separatrix of trapped particle modes. *Rev. Sci. Instrum.* **74**, 1925–1928.
- KABANTSEV, A. A. and DRISCOLL, C. F. (2003b). Diocotron Instabilities in an Electron Column Induced by a Small Fraction of Transient Positive Ions. In SCHAUER, M., MITCHELL, T., and NEBEL, R., editors, *Non-Neutral Plasma Physics V: Workshop on Non-Neutral Plasmas: AIP Conference Proceedings, Volume 692*, pages 61–68, Melville, NY. American Institute of Physics.
- KABANTSEV, A. A. and DRISCOLL, C. F. (2003c). Trapped-Particles Modes and Asymmetry-Induced Transport in Single-Species Plasmas. *Phys. Rev. Lett.* **89**, 245001.
- KABANTSEV, A. A., YU, J. H., LYNCH, R. B., and DRISCOLL, C. F. (2003). Trapped particles and asymmetry-induced transport. *Phys. Plasmas* **10**, 1628–1635.
- KAPETANAKOS, C. A. and TRIVELPIECE, A. W. (1971). Diagnostics of non-neutral plasmas using an induced-current electrostatic probe. *J. Appl. Phys.* **42**, 4841.
- KITTEL, C. and KROEMER, H. (1980). *Thermal Physics*. Freeman, second edition.
- KRIESEL, J. M. and DRISCOLL, C. F. (1998). Electron plasma profiles from a cathode with an r^2 potential variation. *Phys. Plasmas*. **5**, 1265–1272. 6M.
- KRIESEL, J. M. and DRISCOLL, C. F. (2001). Measurements of viscosity in pure-electron plasmas. *Phys. Rev. Lett.* **87**, 135003.
- KURZ, C., GILBERT, S. J., GREAVES, R. G., and SURKO, C. M. (1998). New source of ultra-cold positron and electron beams. *Nucl. Instrum. Meth. B* **143**, 188–194.

- LANGMUIR, I. (1923). The Electron Emission from Thoriated Tungsten Filaments. *Phys. Rev.* **22**, 357.
- LEVY, R. H. (1968). Two new results in cylindrical diocotron theory. *Phys. Fluids* **11**, 920.
- LEVY, R. H., DAUGHERTY, J. D., and BUNEMAN, O. (1969). Ion Resonance Instability in Grossly Nonneutral Plasmas. *Phys. Fluids* **12**, 2616.
- LONGMIRE, C. L. and ROSENBLUTH, M. N. (1956). Diffusion of Charged Particles Across a Magnetic Field. *Phys. Rev.* **103**, 507–510.
- MALMBERG, J. H. and DEGRASSIE, J. S. (1975). Properties of Nonneutral Plasma. *Phys. Rev. Lett.* **35**, 577–580.
- MALMBERG, J. H. and DRISCOLL, C. F. (1980). Long-Time Containment of a Pure Electron Plasma. *Phys. Rev. Lett.* **44**, 654–657.
- MALMBERG, J. H., DRISCOLL, C. F., and WHITE, W. D. (1982). Experiments with Pure Electron Plasmas. *Physica Scripta* **T2**, 288–292.
- MARQUARDT, D. W. (1963). An Algorithm for Least-Squares Estimation of Non-linear Parameters. *J. Soc. Ind. Appl. Math.* **11**, 431–441.
- MASON, G. W. (2003). Decay of trapped-particle asymmetry modes in non-neutral plasmas in a Malmberg-Penning trap. *J. Soc. Ind. Appl. Math.* **10**, 1231–1238.
- MONTGOMERY, D., JOYCE, G., and TURNER, L. (1974). Magnetic field dependence of plasma relaxation times. *Phys. Fluids* **17**, 2201–2204.
- MOORE, D. A. (1995). *Pressure Measurement Using a Pure Electron Plasma*. PhD thesis, Princeton University.

- MORRISON, K., PAUL, S. F., and DAVIDSON, R. C. (2003). Measurements of Plasma Expansion due to Background Gas in the Electron Diffusion Gauge Experiment. In SCHAUER, M., MITCHELL, T., and NEBEL, R., editors, *Non-Neutral Plasma Physics V: Workshop on Non-Neutral Plasmas: AIP Conference Proceedings, Volume 692*, pages 75–80, Melville, NY. American Institute of Physics.
- MORRISON, K. A., DAVIDSON, R. C., PAUL, S. F., BELLI, E. A., and CHAO, E. H. (2001). Expansion rate measurements at moderate pressure of non-neutral electron plasmas in the Electron Diffusion Gauge (EDG) experiment. *Phys. Plasmas* **8**, 3506–3509.
- MORRISON, K. A., DAVIDSON, R. C., PAUL, S. F., and JENKINS, T. G. (2002). Investigation of the Expansion Rate Scaling of Plasmas in the Electron Diffusion Gauge Experiment. In ANDEREGG, F., SCHWEIKHARD, L., and DRISCOLL, C. F., editors, *Non-Neutral Plasma Physics IV: Workshop on Non-Neutral Plasmas: AIP Conference Proceedings, Volume 606*, pages 416–421, Melville, NY. American Institute of Physics.
- NOTTE, J., PEURRUNG, A. J., FAJANS, J., CHU, R., and WURTELE, J. S. (1992). Asymmetric Stable Equilibria of Non-Neutral Plasmas. *Phys. Rev. Lett.* **69**, 3056–3059.
- O'NEIL, T. M. (1980a). A confinement theorem for nonneutral plasmas. *Phys. Fluids* **23**, 2216–2218.
- O'NEIL, T. M. (1980b). Nonneutral Plasmas Have Exceptional Confinement Properties. *Comments Plasma Phys. Cont. Fusion* **5**, 213–217.

- O'NEIL, T. M. (1985). New Theory of Transport Due to Like-Particle Collisions. *Phys. Rev. Lett.* **55**, 943–946.
- O'NEIL, T. M. (1995). Plasmas with a Single Sign of Charge (An Overview). *Phys. Scripta* **59**, 341–351.
- O'NEIL, T. M. and DRISCOLL, C. F. (1979). Transport to thermal equilibrium of a pure electron plasma. *Phys. Fluids* **22**, 266–277.
- O'NEIL, T. M. and SMITH, R. A. (1992). Stability theorem for off-axis states of a non-neutral plasmas column. *Phys. Fluids B* **4**, 2720–2728.
- PAUL, S. F., MORRISON, K., and DAVIDSON, R. C. (2003). Experimental Investigation of $m = 1$ Diocotron Mode Growth at Low Electron Densities. In SCHAUER, M., MITCHELL, T., and NEBEL, R., editors, *Non-Neutral Plasma Physics V: Workshop on Non-Neutral Plasmas: AIP Conference Proceedings, Volume 692*, pages 81–86, Melville, NY. American Institute of Physics.
- PAUL, S. F., MORRISON, K. A., DAVIDSON, R. C., and JENKINS, T. G. (2002). $m = 1$ Diocotron Mode Damping in the Electron Diffusion Gauge (EDG) Experiment. In ANDEREGG, F., SCHWEIKHARD, L., and DRISCOLL, C. F., editors, *Non-Neutral Plasma Physics IV: Workshop on Non-Neutral Plasmas: AIP Conference Proceedings, Volume 606*, pages 305–310, Melville, NY. American Institute of Physics.
- PEURRUNG, A. J. and FAJANS, J. (1993). A pulsed microchannel-plate-based non-neutral plasma imaging system. *Rev. Sci. Instrum.* **64**, 52–55.
- PEURRUNG, A. J., NOTTE, J., and FAJANS, J. (1993). Observation of the Ion Resonance Instability. *Phys. Rev. Lett.* **70**, 295–298.

- PRASAD, S. A. and MALMBERG, J. H. (1986). A nonlinear diocotron mode. *Phys. Fluids* **29**, 2196.
- PRASAD, S. A. and O'NEIL, T. M. (1983). Waves in a cold pure electron plasma of finite length. *Phys. Fluids* **26**, 665–672.
- PRASAD, S. A. and O'NEIL, T. M. (1984). Vlasov theory of electrostatic modes in a finite length electron column. *Phys. Fluids* **27**, 206–213.
- PRESS, W. H., TEUKOLSKY, S. A., VETTERLING, W. T., and FLANNERY, B. P. (1992). *Numerical recipes in C : the art of scientific computing*. Cambridge University Press, Cambridge, England.
- RAPP, D. and ENGLANDER-GOLDEN, P. (1965). Total cross-sections for ionization and attachment in gases by electron impact. *J. Chem. Phys.* **43**, 1464.
- ROBERSON, C. W. and DRISCOLL, C. F., editors (1988). *Non-Neutral Plasma Physics*, volume 175 of *AIP Conference Proceedings*. American Institute of Physics, New York.
- ROSENBLUTH, M. N. and KAUFMANN, A. N. (1958). Plasma Diffusion in a Magnetic Field. *Phys. Rev.* **109**, 1–5.
- ROSENBLUTH, M. N. and LIU, C. S. (1976). Cross-field energy transport by plasma waves. *Phys. Fluids* **19**, 815–818.
- SCHAUER, M., MITCHELL, T., and NEBEL, R., editors (2003). *Non-Neutral Plasma Physics V*, volume 692 of *AIP Conference Proceedings*. American Institute of Physics, Melville, NY.

- SILIN, V. P. (1962). High-Frequency Dielectric Constant of a Plasma. *Sov. Phys. JETP-USSR* **14**, 617–622.
- SIMON, A. (1955). Diffusion of Like Particles Across a Magnetic Field. *Phys. Rev.* **100**, 1557–1559.
- Stowell (1997). Analysis by Ronald H. Stowell.
- SURKO, C. M., GREAVES, R. G., IWATA, K., and GILBERT, S. J. (2000). Atomic and molecular physics using positron accumulation techniques - Summary and a look to the future. *Nucl. Instrum. Meth. B* **171**, 2–16.
- TAN, J. N., BOLLINGER, J. J., and WINELAND, D. J. (1995). Minimizing the Time-Dilation Shift in Penning Trap Atomic Clocks. *IEEE T. Instrum. Meas.* **44**, 144–147.
- WARE, A. A. (1993). A Fokker-Planck operator for the emission and absorption of electron plasma waves in a magnetized plasma. *Phys. Rev. Lett.* **5**, 2769–2777.
- WHITE, W. D., MALMBERG, J. H., and DRISCOLL, C. F. (1982). Resistive-wall Destabilization of Diocotron Waves. *Phys. Rev. Lett.* **49**, 1822–1826.